Electronic Supplementary Information

Unveiling the promising anticancer activity of palladium(II)-aryl complexes bearing diphosphine ligands: a structure-activity relationship analysis

Giovanni Tonon,[a] Matteo Mauceri,[a] Enrico Cavarzerani,[a] Rachele Piccolo,[a] Claudio Santo,[a] Nicola Demitri,[b] Laura Orian,[c] P. A. Nogara,[d] J. B. T. Rocha,[d] Vincenzo Canzonieri,[e,f] Flavio Rizzolio,*[a,e] Fabiano Visentin*[a] and Thomas Scattolin*[c]

TABLE OF CONTENTS

NMR SPECTRA

1D NMR and 2D NMR spectrum were recorded on Bruker 300 or 400 Advance spectrometers. Chemical shifts values (ppm) are given relative to TMS (^{1}H and ^{13}C), H_3PO_4 (^{31}P) and CCl_3F (^{19}F).

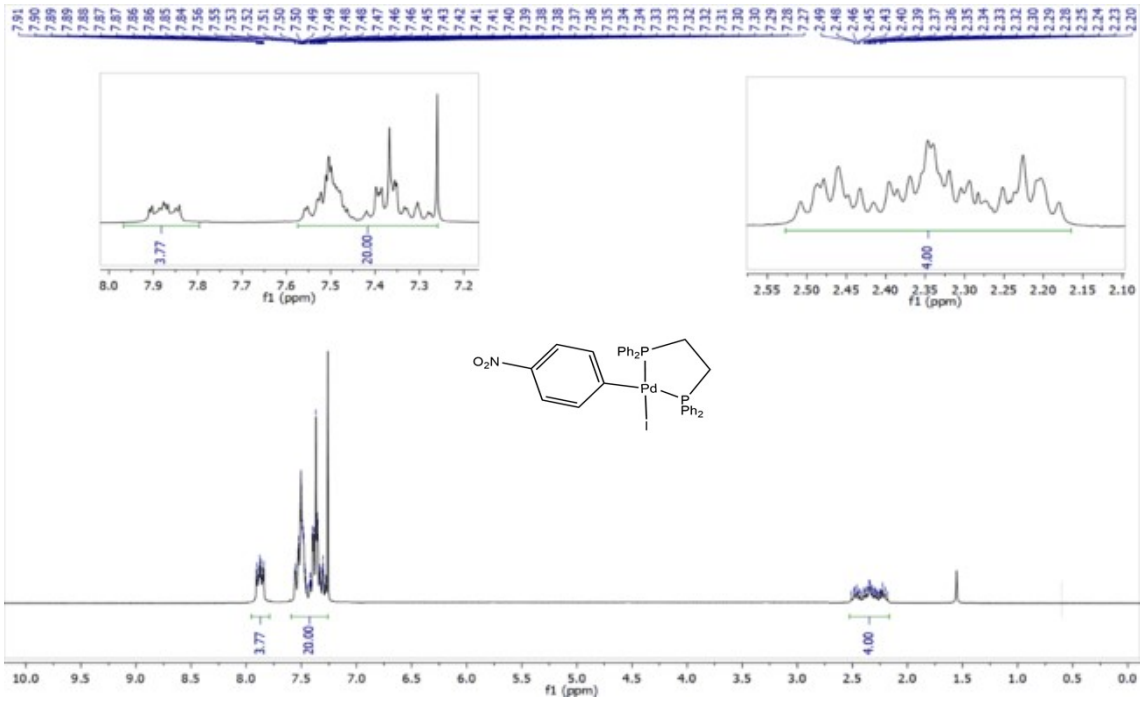

Figure S1. ^{1}H NMR spectrum of **2a** in $CDCl_3$ at 298 K.

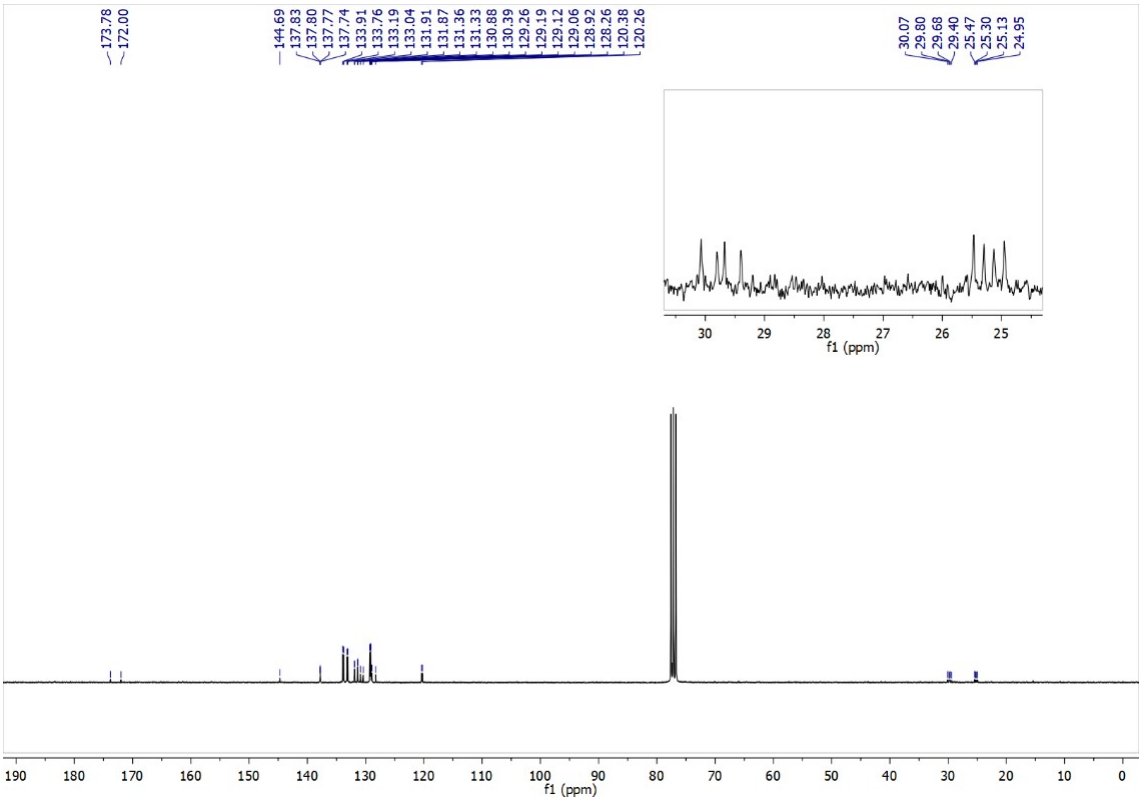

Figure S2. $^{13}C\{^{1}H\}$ NMR spectrum of **2a** in $CDCl_3$ at 298 K.

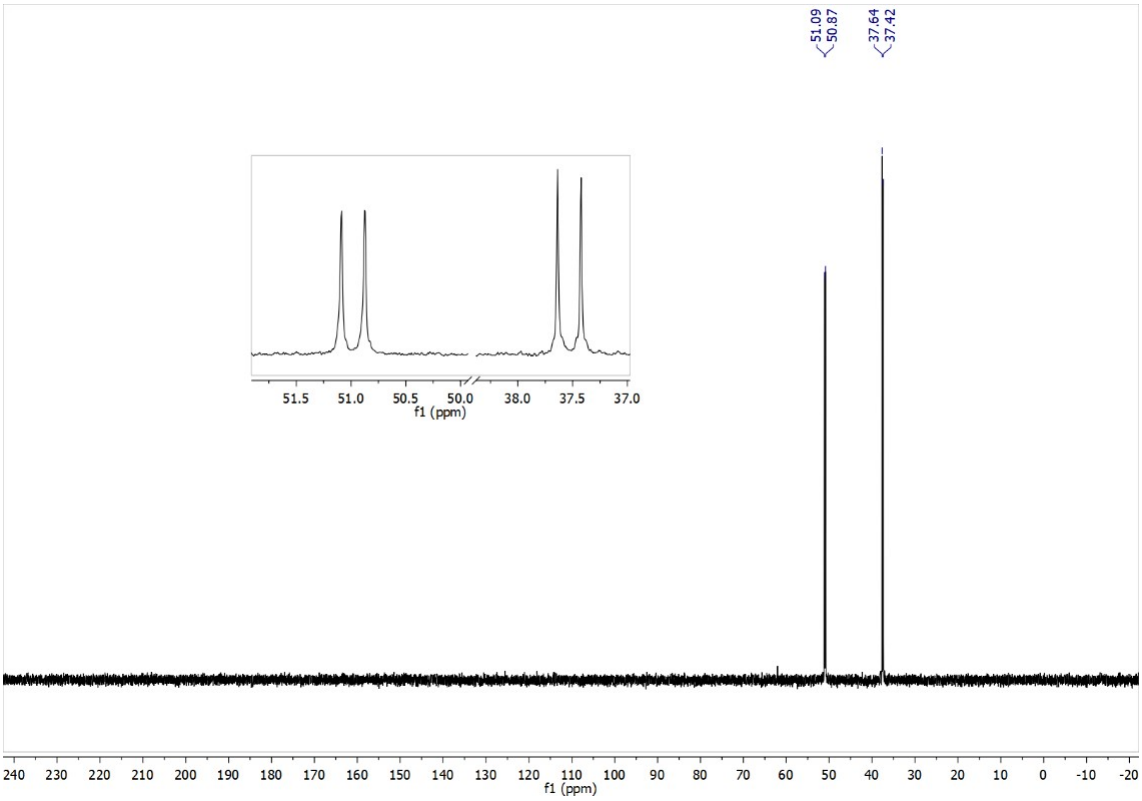

Figure S3. $^{31}P\{^{1}H\}$ NMR spectrum of **2a** in $CDCl_3$ at 298 K

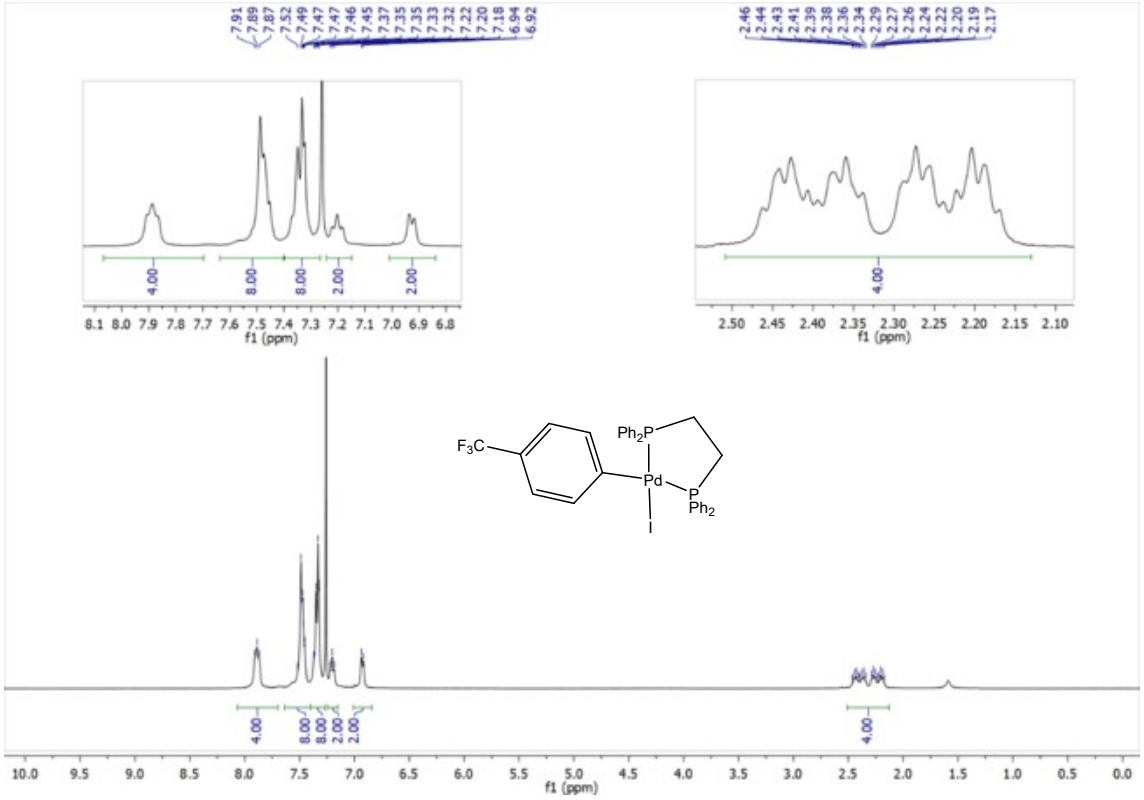

Figure S4. ^{1}H NMR spectrum of **2b** in $CDCl_3$ at 298 K.

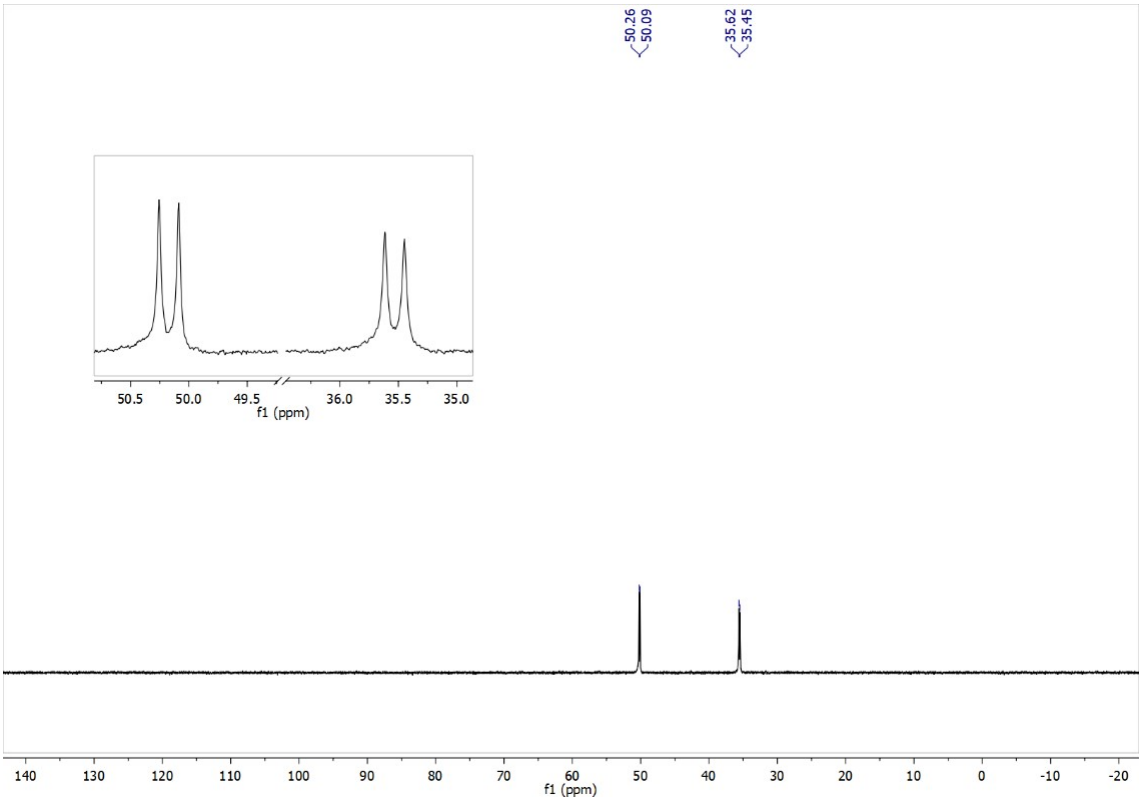

Figure S5. $^{31}P\{^{1}H\}$ NMR spectrum of **2b** in $CDCl_3$ at 298 K.

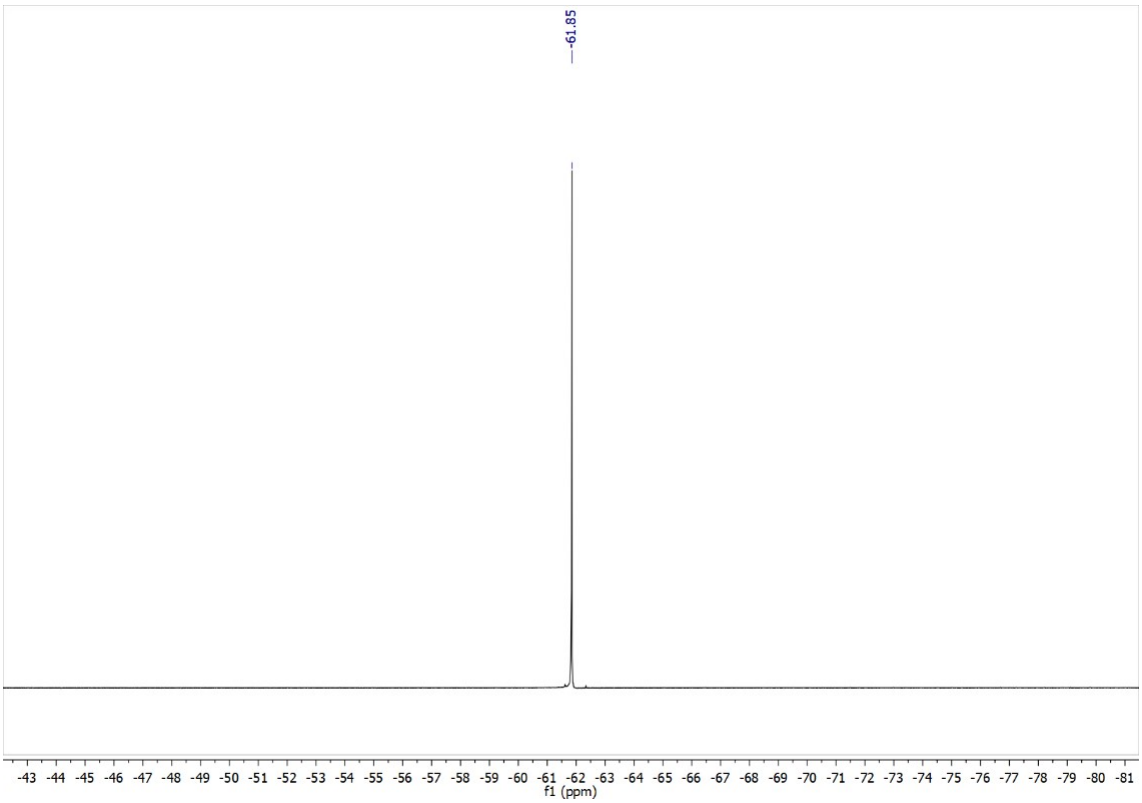

Figure S6. $^{19}F\{^{1}H\}$ NMR spectrum of **2b** in $CDCl_3$ at 298K.

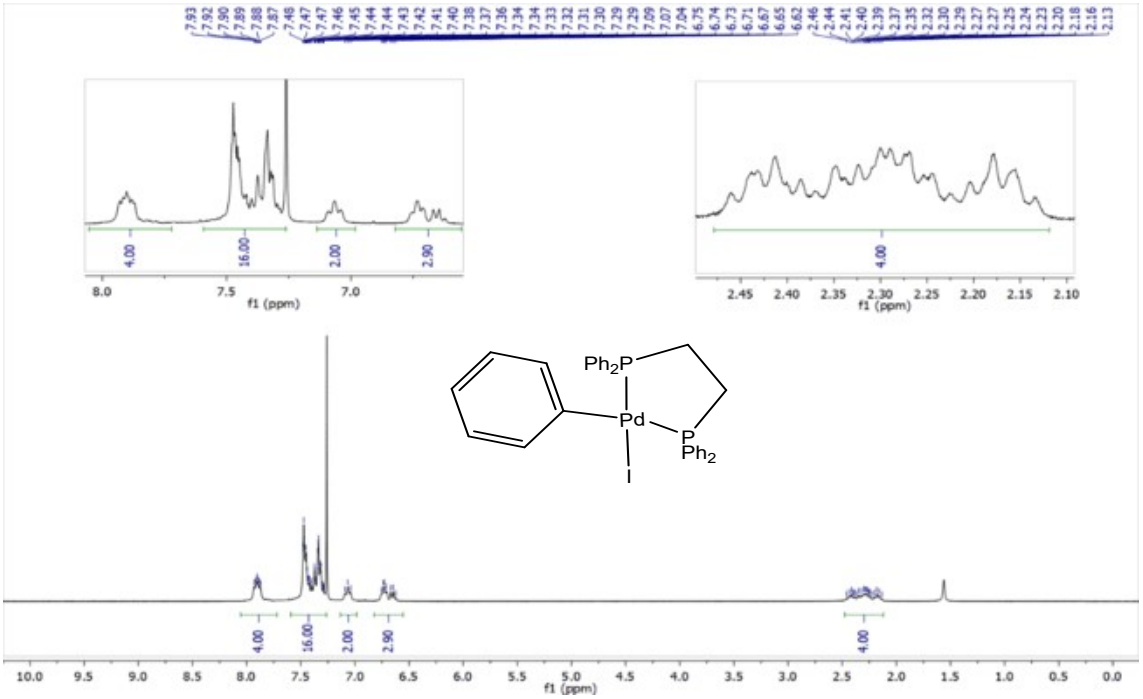

Figure S7. ^{1}H NMR spectrum of **2c** in $CDCl_3$ at 298 K.

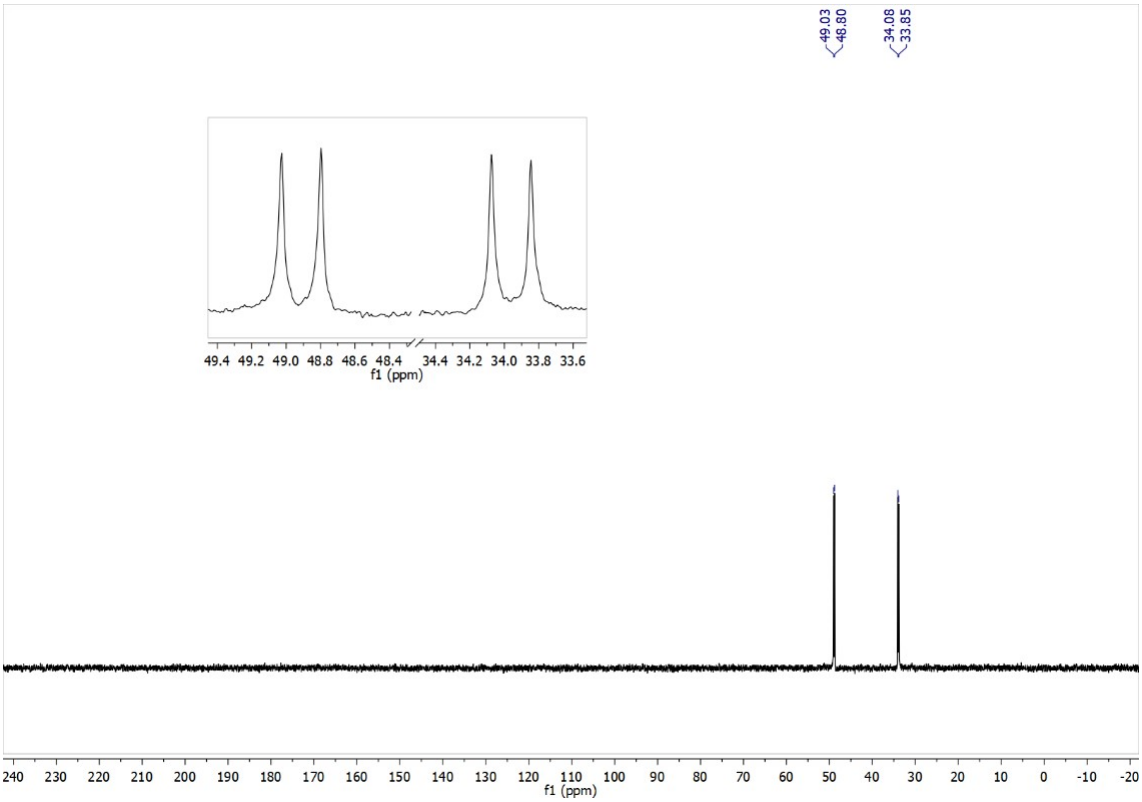

Figure S8. $^{31}P\{^{1}H\}$ NMR spectrum of **2c** in $CDCl_3$ at 298 K.

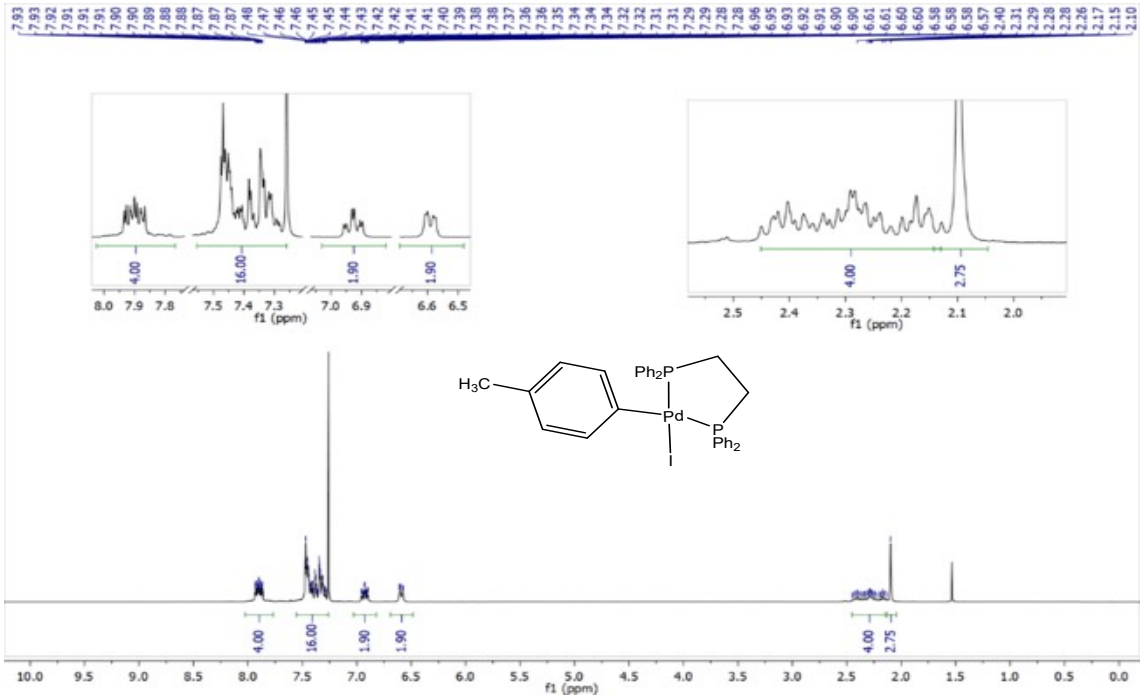

Figure S9. ^{1}H NMR spectrum of **2d** in $CDCl_3$ at 298 K.

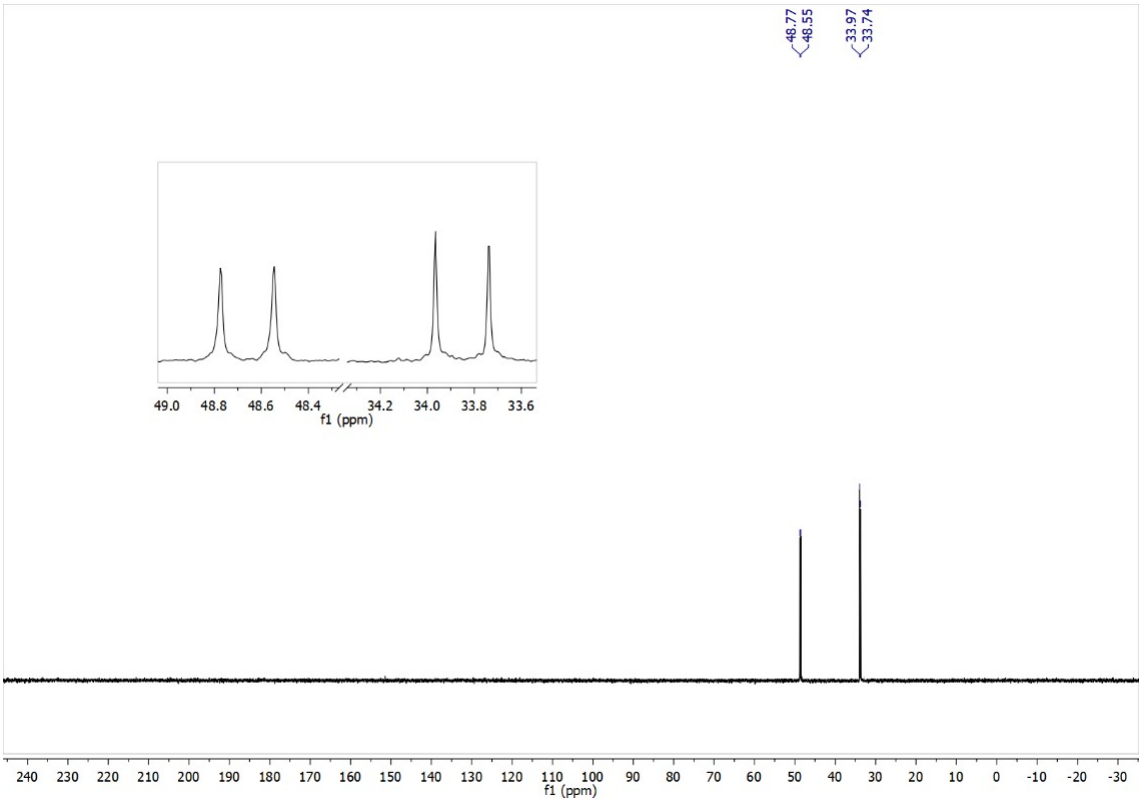

Figure S10. $^{31}P\{^{1}H\}$ NMR spectrum of **2d** in $CDCl_3$ at 298 K.

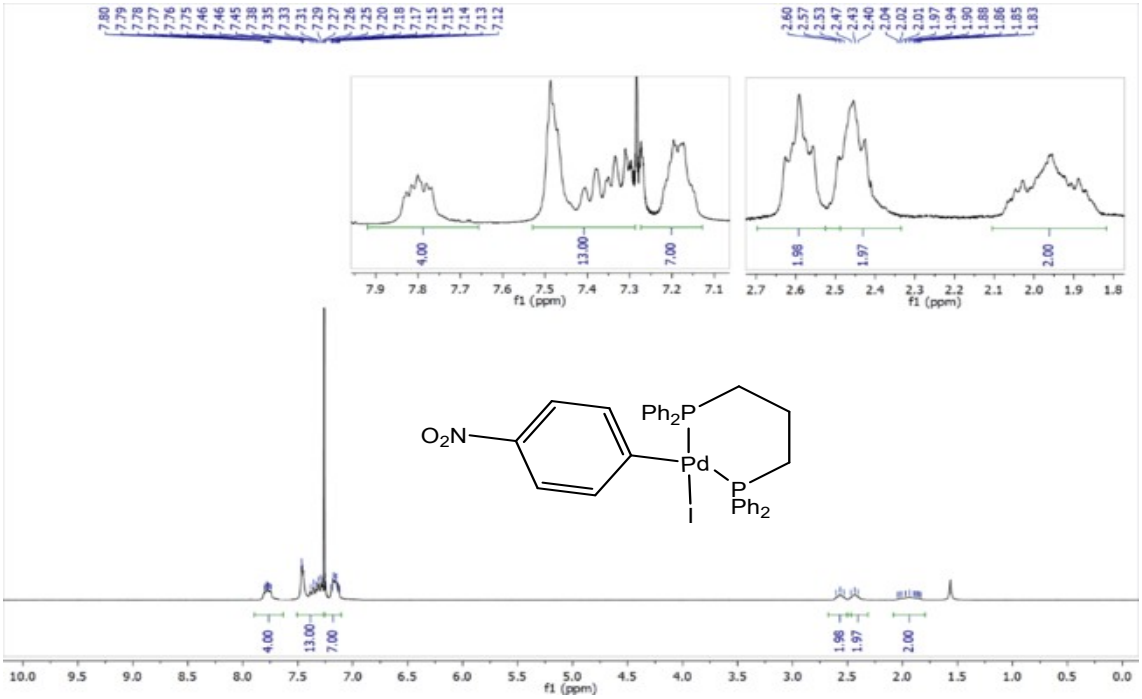

Figure S11. ^{1}H NMR spectrum of **3a** in $CDCl_3$ at 298 K.

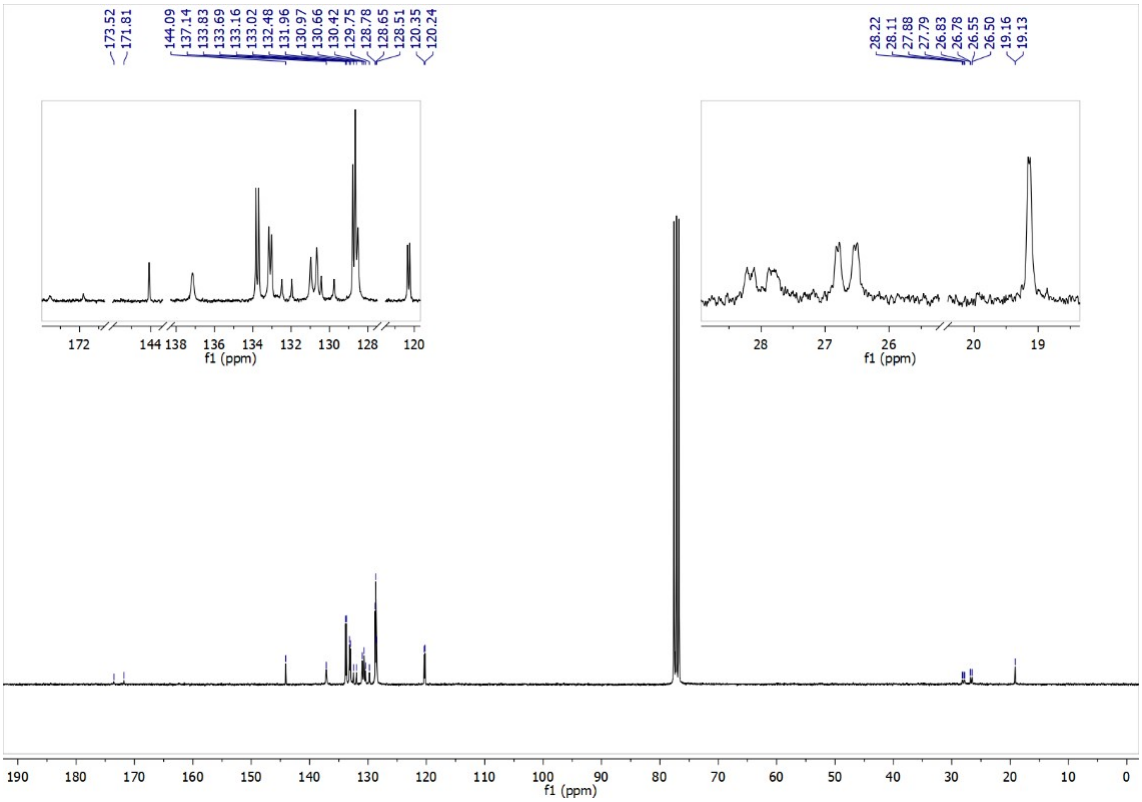

Figure S12. $^{13}C\{^{1}H\}$ NMR spectrum of **3a** in $CDCl_3$ at 298 K.

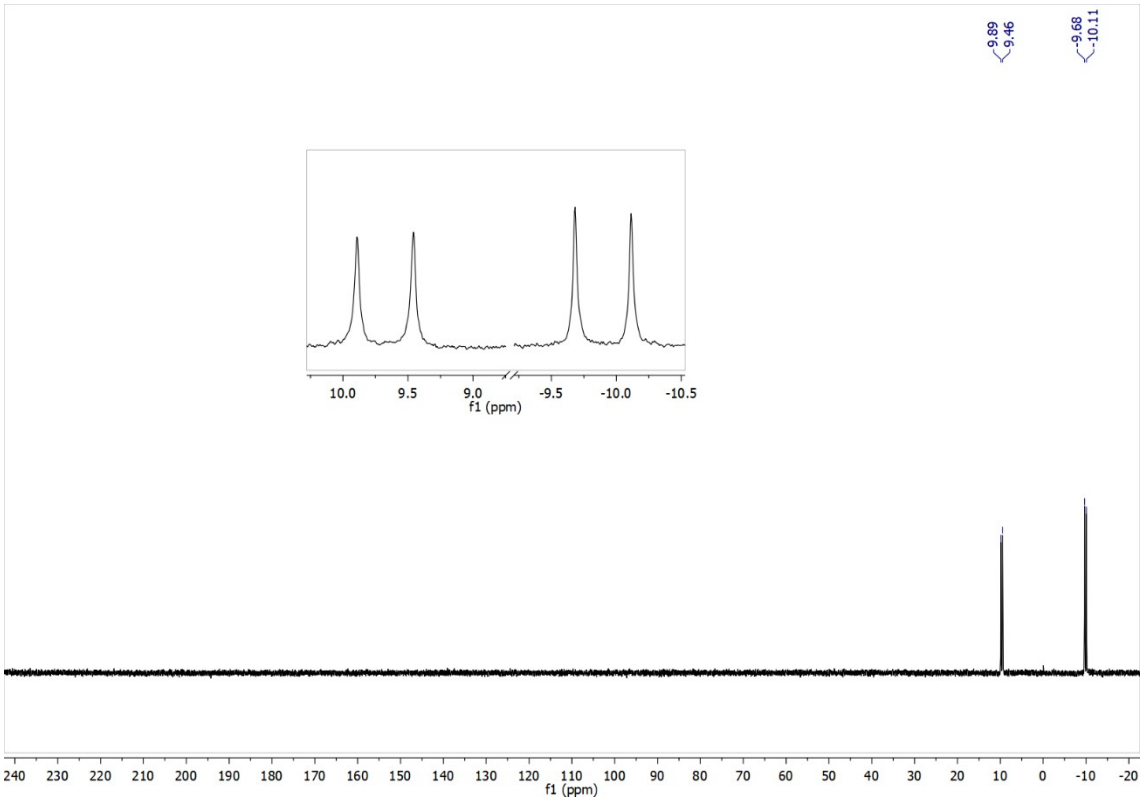

Figure S13. $^{31}P\{^{1}H\}$ NMR spectrum of **3a** in $CDCl_3$ at 298 K.

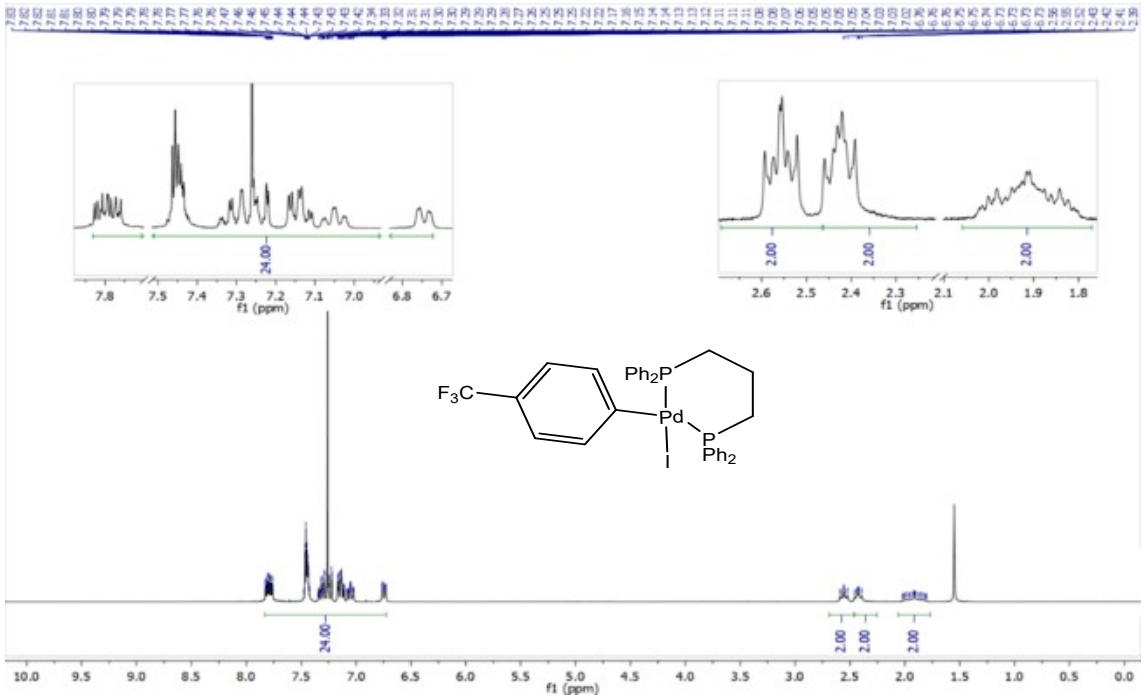

Figure S14. ^{1}H NMR spectrum of **3b** in $CDCl_3$ at 298 K.

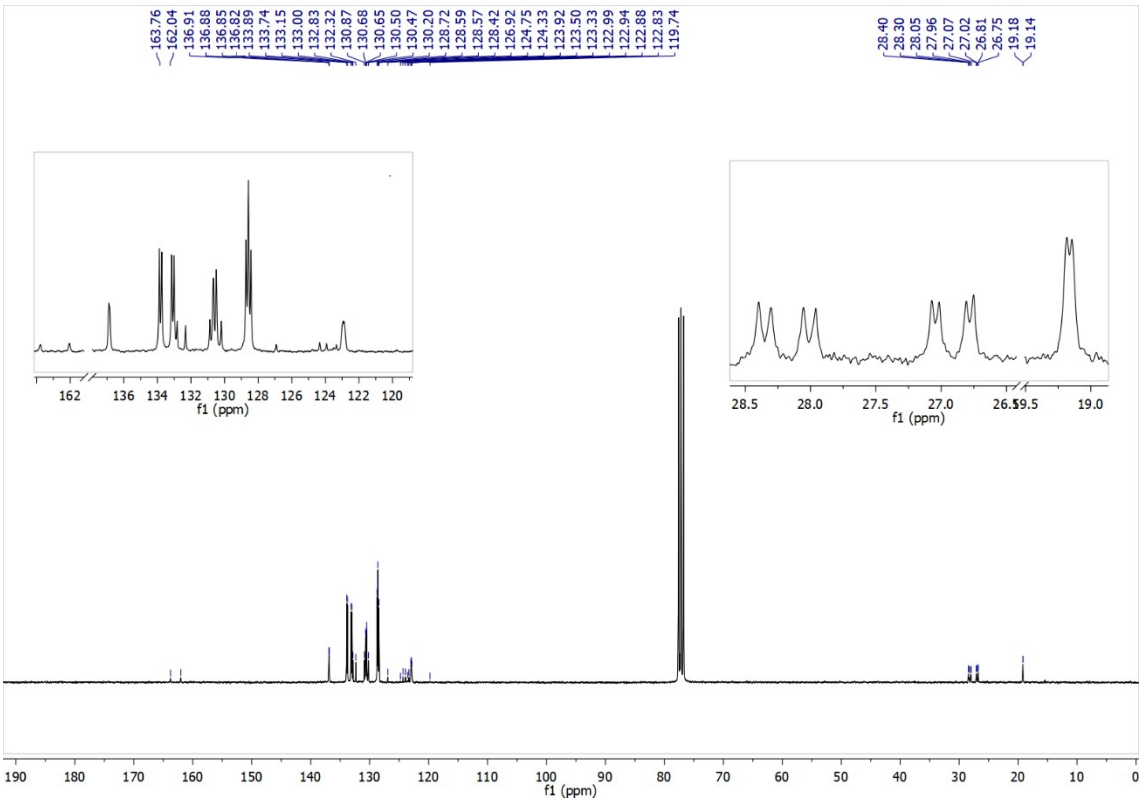

Figure S15. $^{13}C\{^{1}H\}$ NMR spectrum of **3b** in $CDCl_3$ at 298 K.

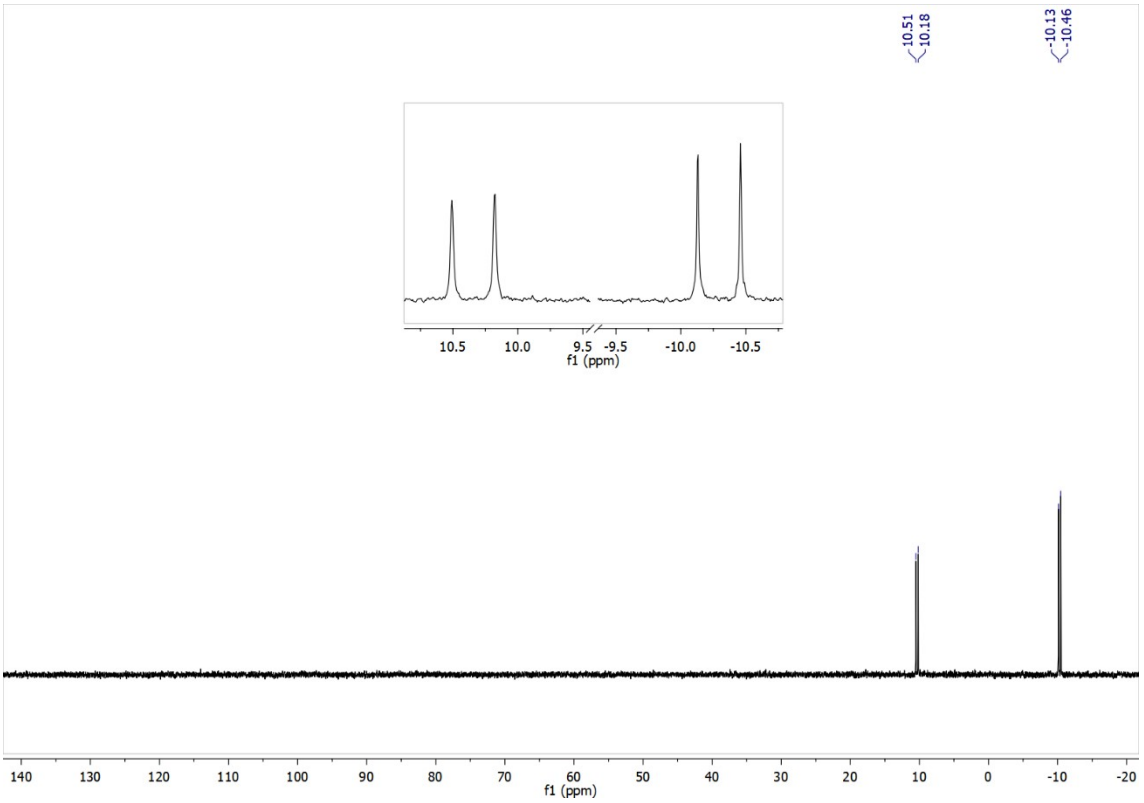

Figure S16. $^{31}P\{^{1}H\}$ NMR spectrum of **3b** in $CDCl_3$ at 298 K.

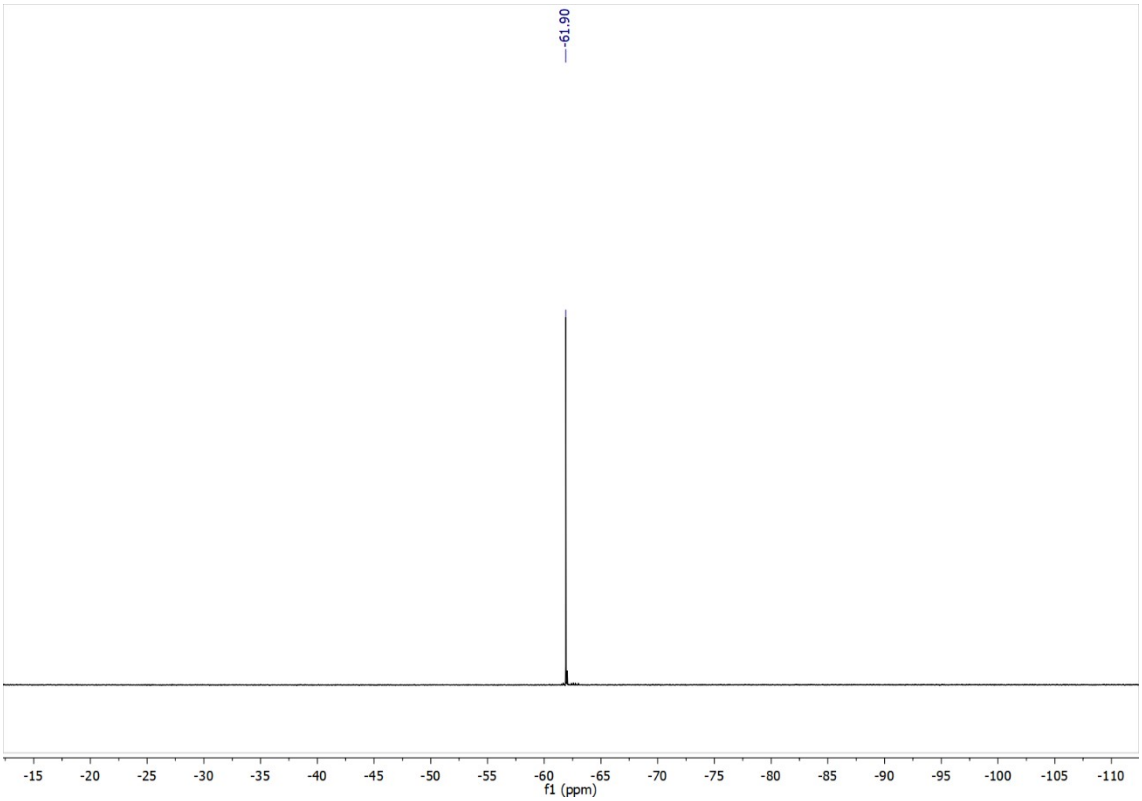

Figure S17. $^{19}F\{^{1}H\}$ NMR spectrum of **3b** in $CDCl_3$ at 298K.

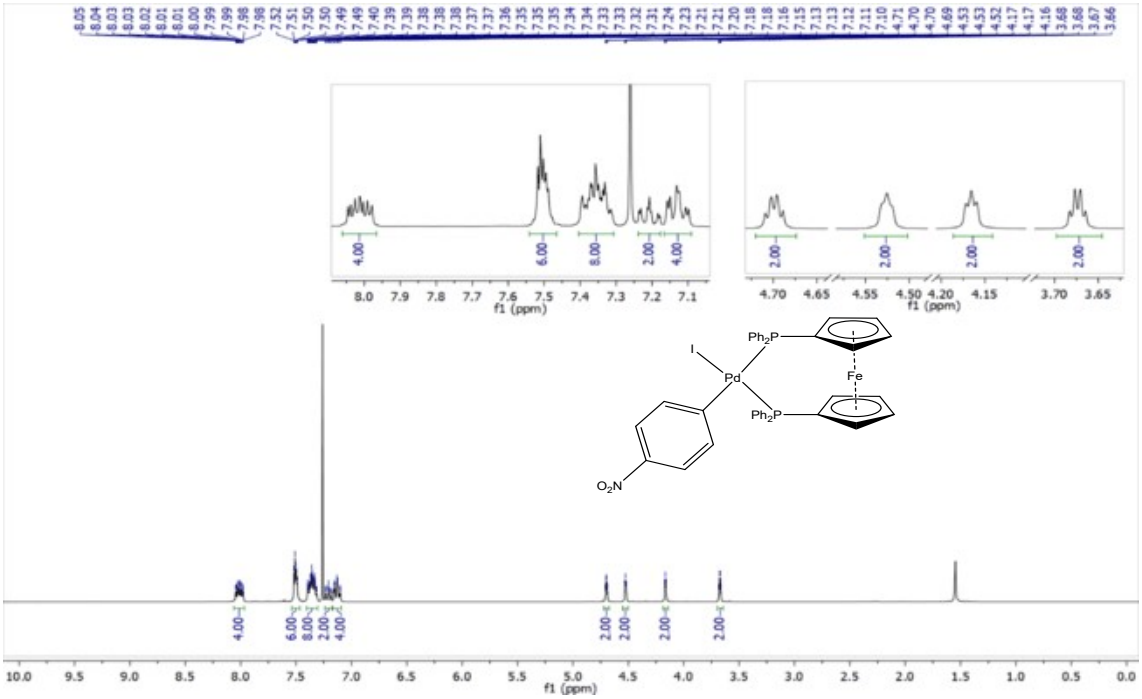

Figure S18. ^{1}H NMR spectrum of **4a** in $CDCl_3$ at 298 K.

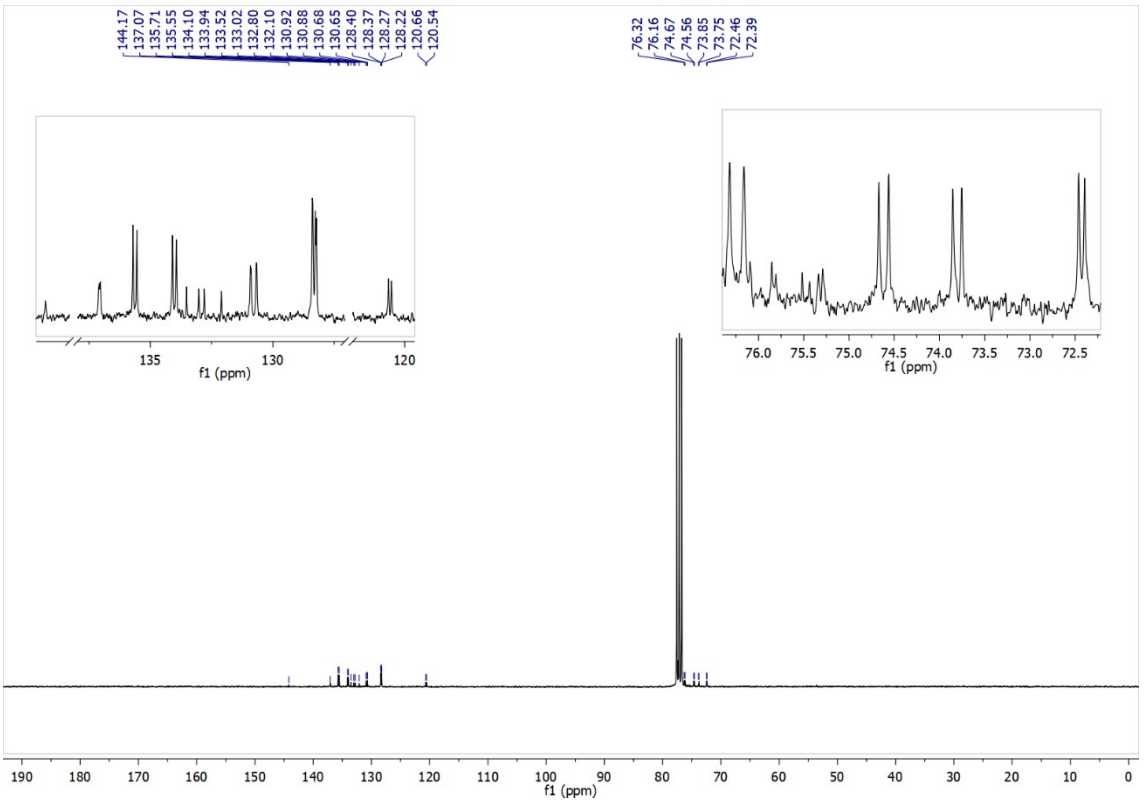

Figure S19. $^{13}C\{^{1}H\}$ NMR spectrum of **4a** in $CDCl_3$ at 298 K.

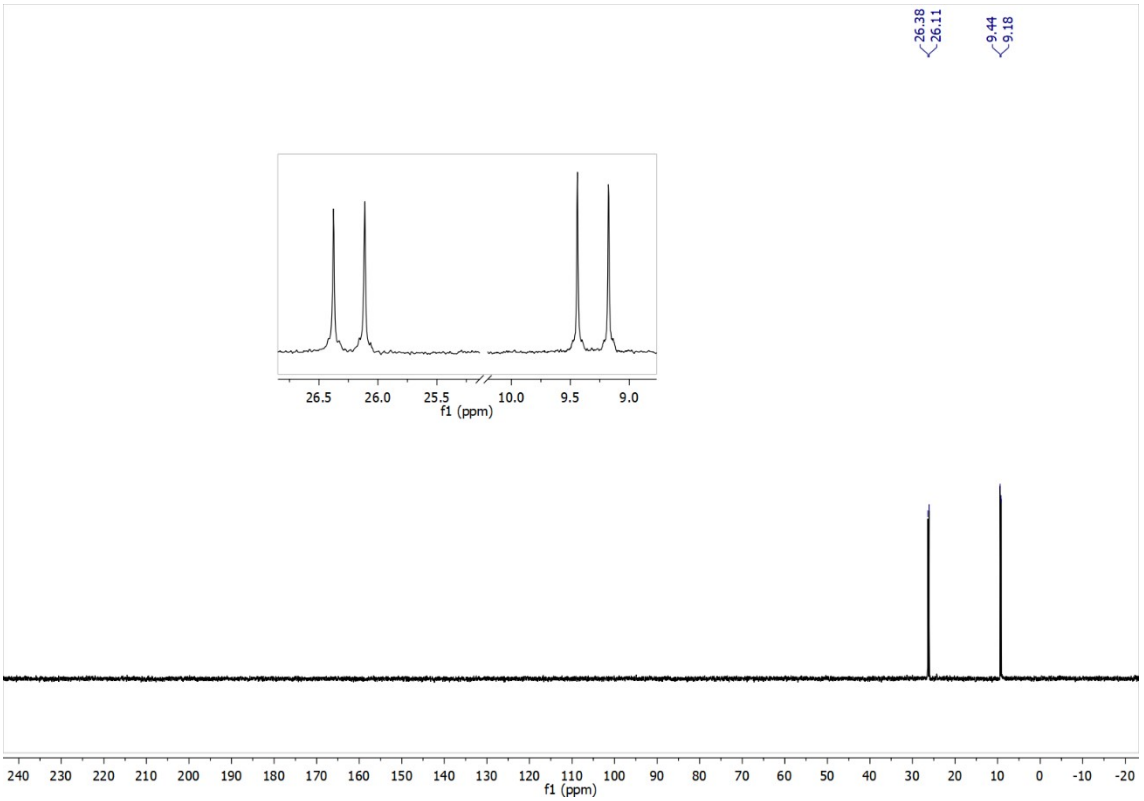

Figure S20. $^{31}P\{^{1}H\}$ NMR spectrum of **4a** in $CDCl_3$ at 298 K.

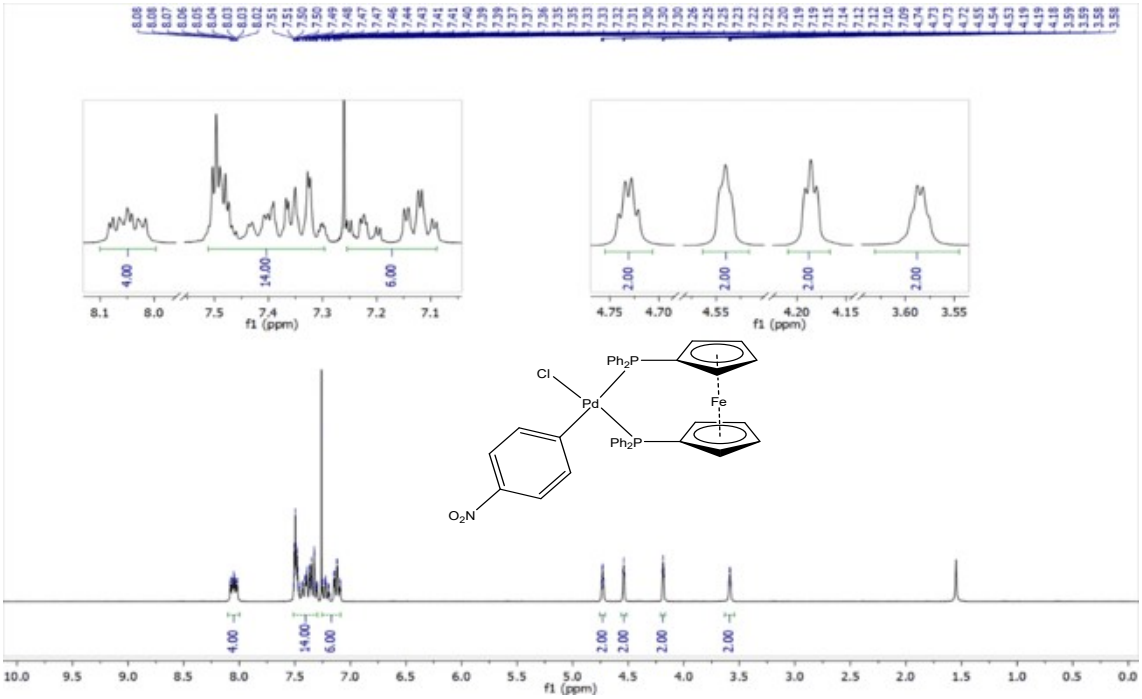

Figure S21. ^{1}H NMR spectrum of **4a-Cl** in $CDCl_3$ at 298 K.

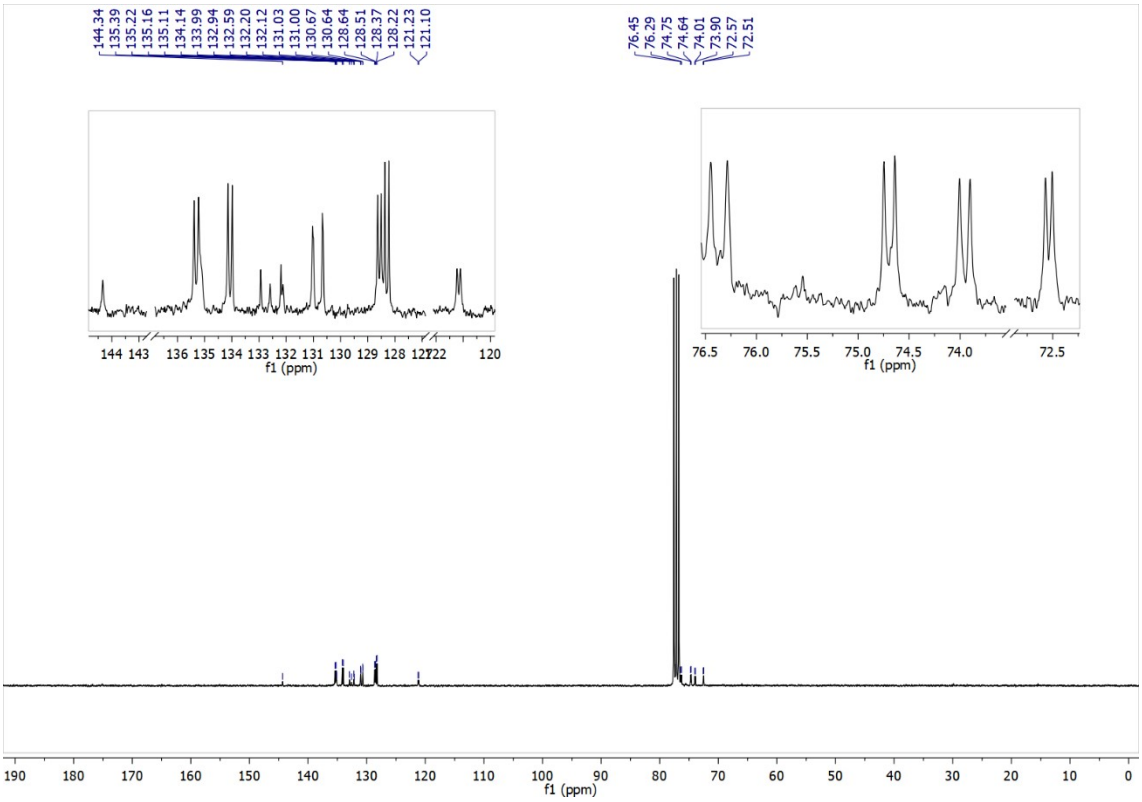

Figure S22. $^{13}C\{^{1}H\}$ NMR spectrum of **4a-Cl** in $CDCl_3$ at 298 K.

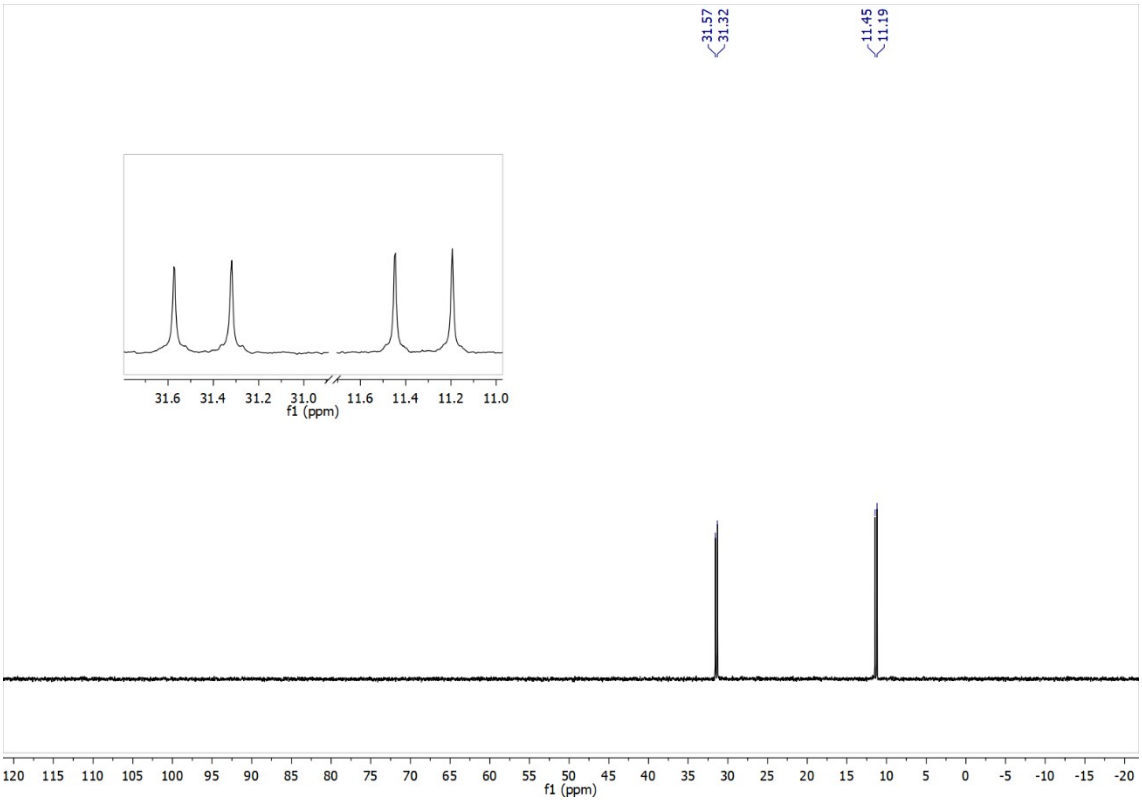

Figure S23. $^{31}P\{^{1}H\}$ NMR spectrum of **4a-Cl** in $CDCl_3$ at 298 K.

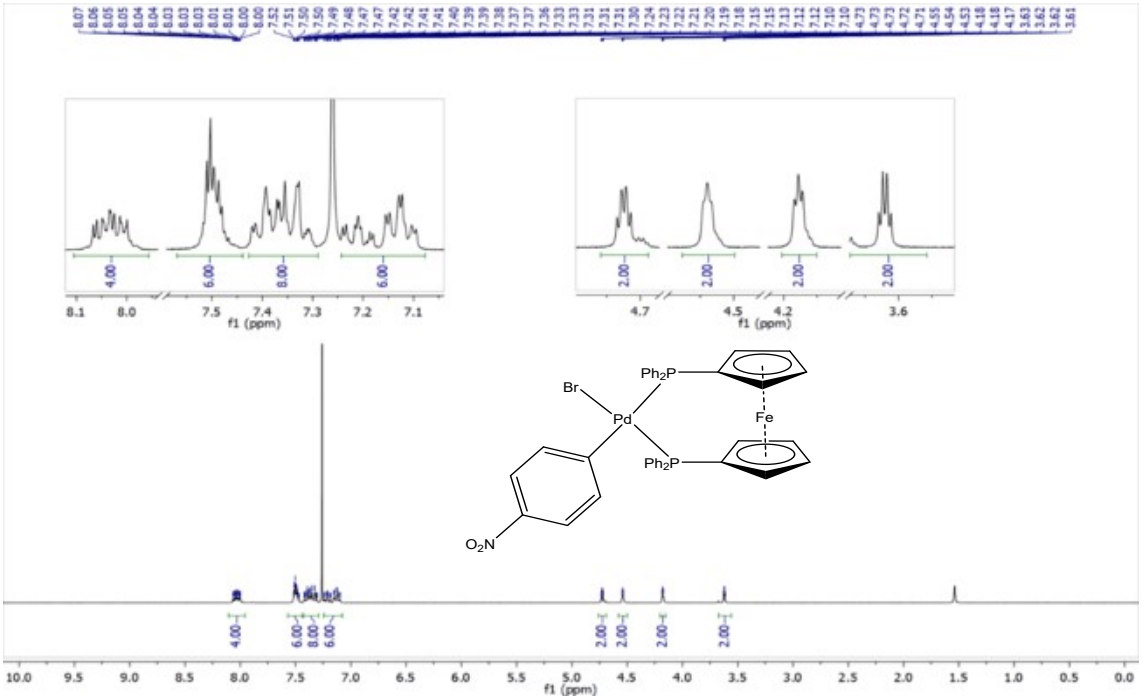

Figure S24. ^{1}H NMR spectrum of **4a-Br** in $CDCl_3$ at 298 K.

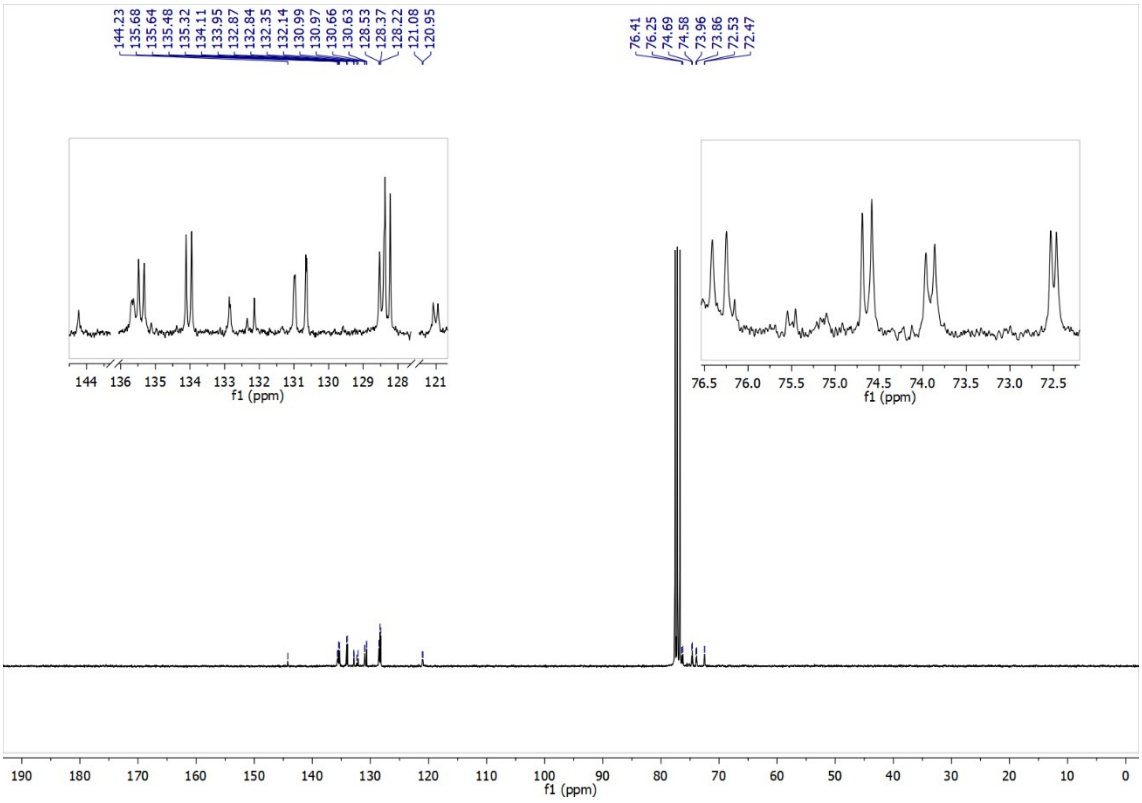

Figure S25. $^{13}C\{^{1}H\}$ NMR spectrum of **4a-Br** in $CDCl_3$ at 298 K.

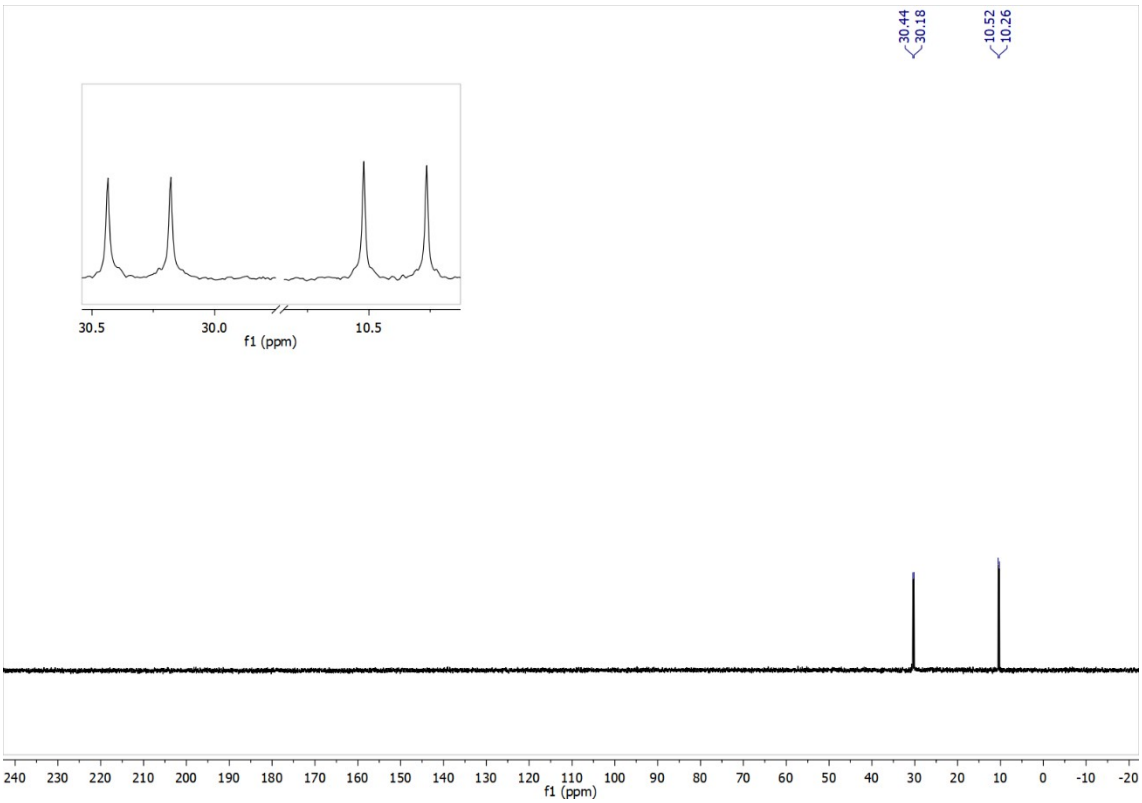

Figure S26. $^{31}P\{^{1}H\}$ NMR spectrum of **4a-Br** in $CDCl_3$ at 298 K.

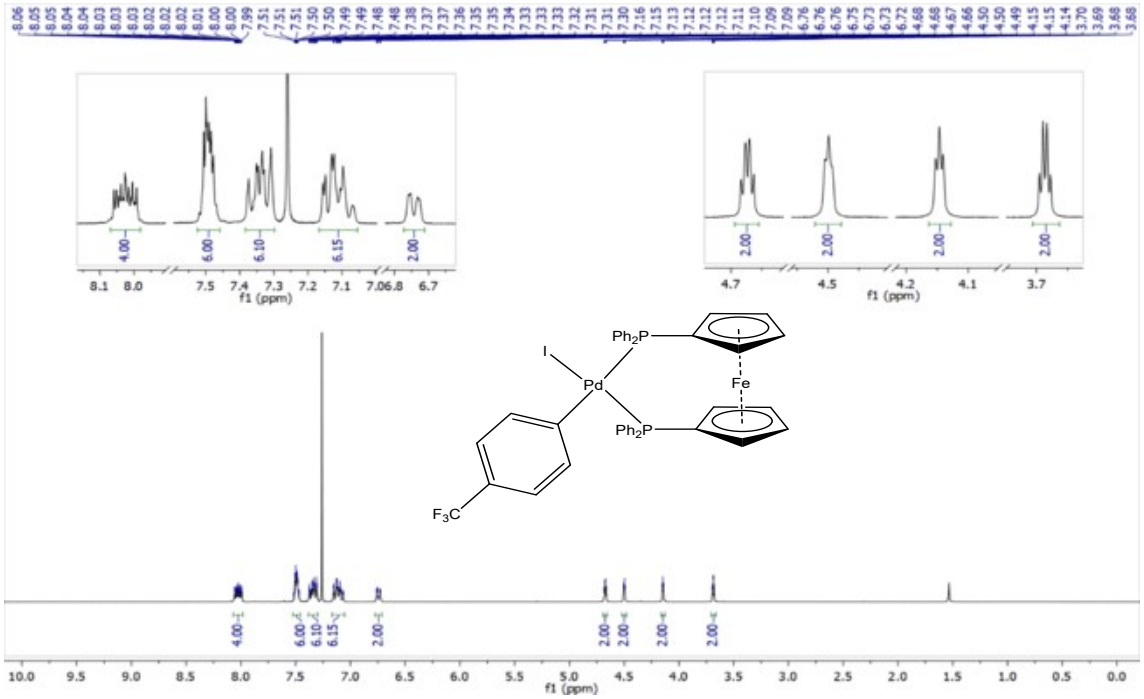

Figure S27. ^{1}H NMR spectrum of **4b** in $CDCl_3$ at 298 K.

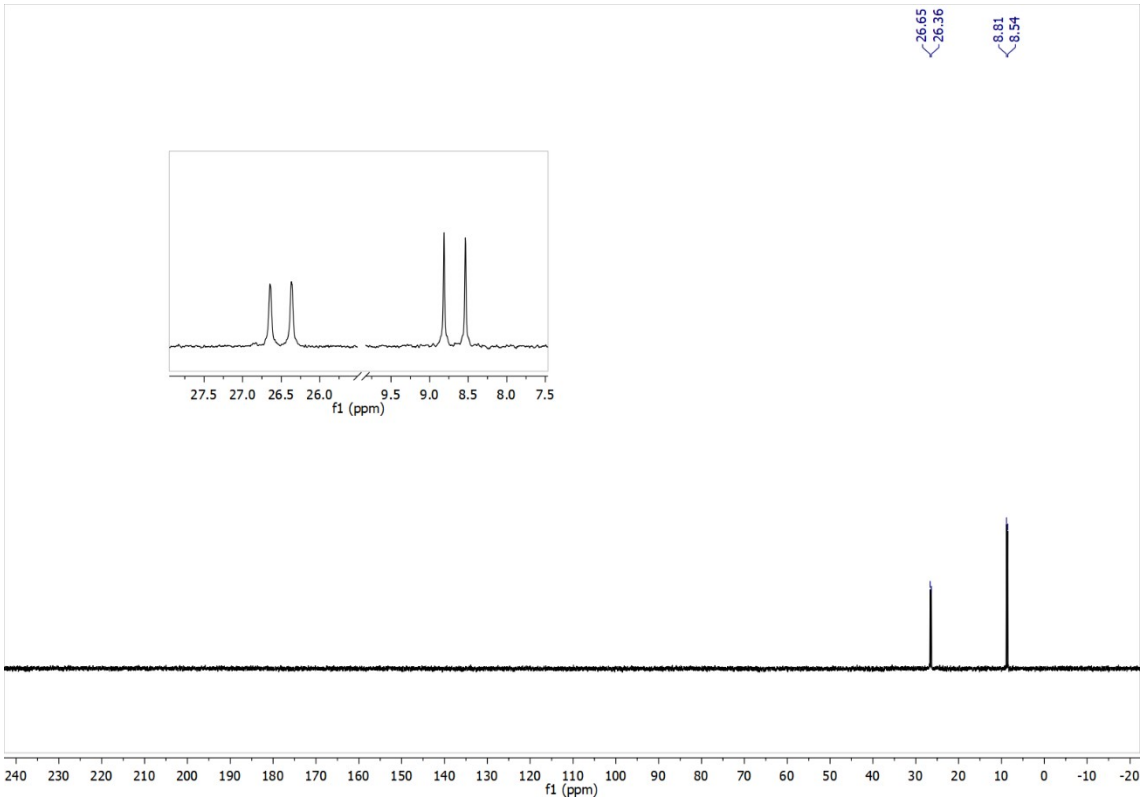

Figure S28. $^{31}P\{^{1}H\}$ NMR spectrum of **4b** in $CDCl_3$ at 298 K.

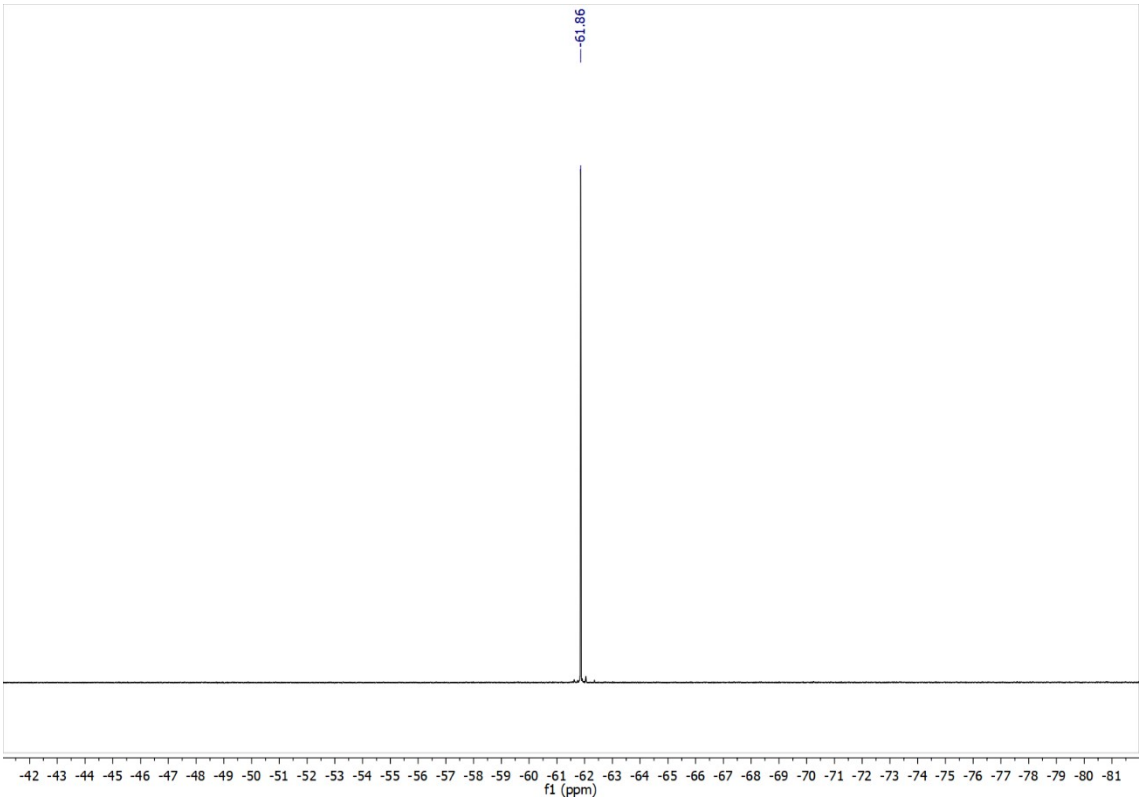

Figure S29. $^{19}F\{^{1}H\}$ NMR spectrum of **4b** in $CDCl_3$ at 298K.

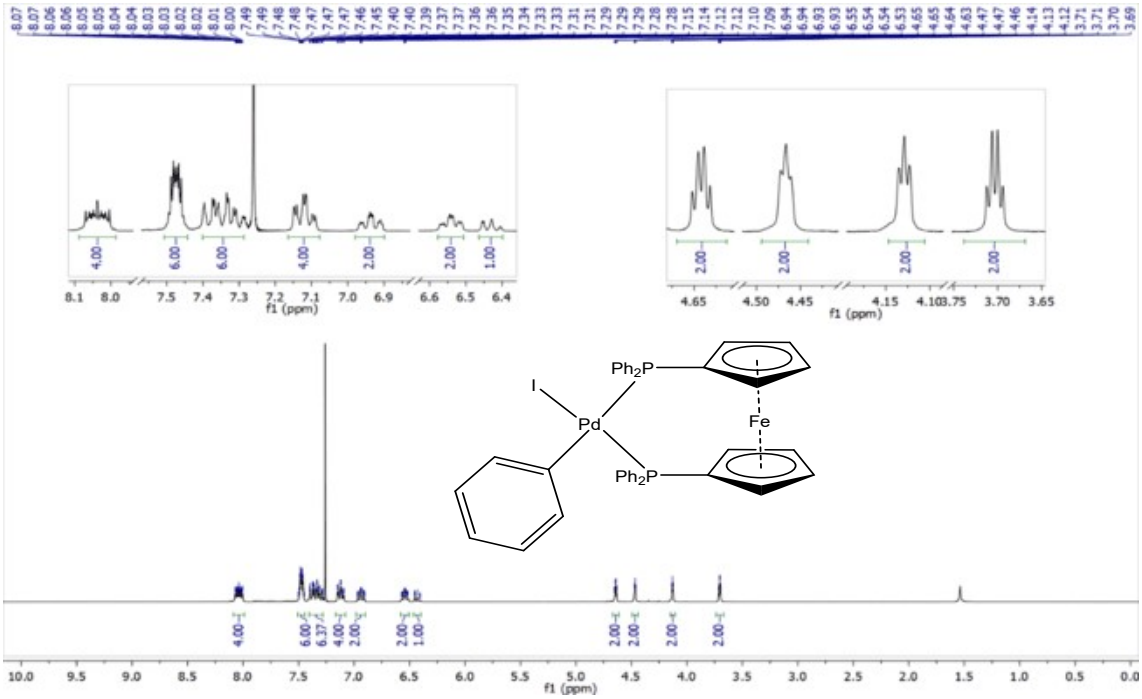

Figure S30. ^{1}H NMR spectrum of **4c** in $CDCl_3$ at 298 K.

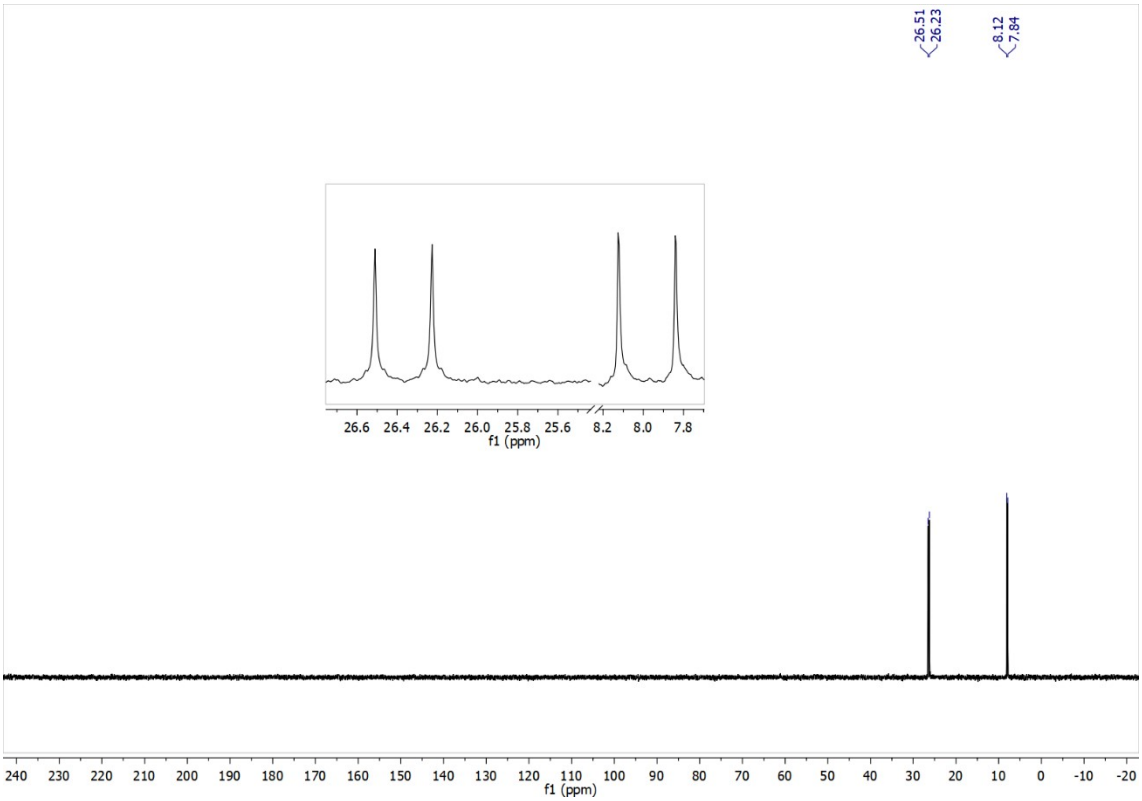

Figure S31. $^{31}P\{^{1}H\}$ NMR spectrum of **4c** in $CDCl_3$ at 298 K.

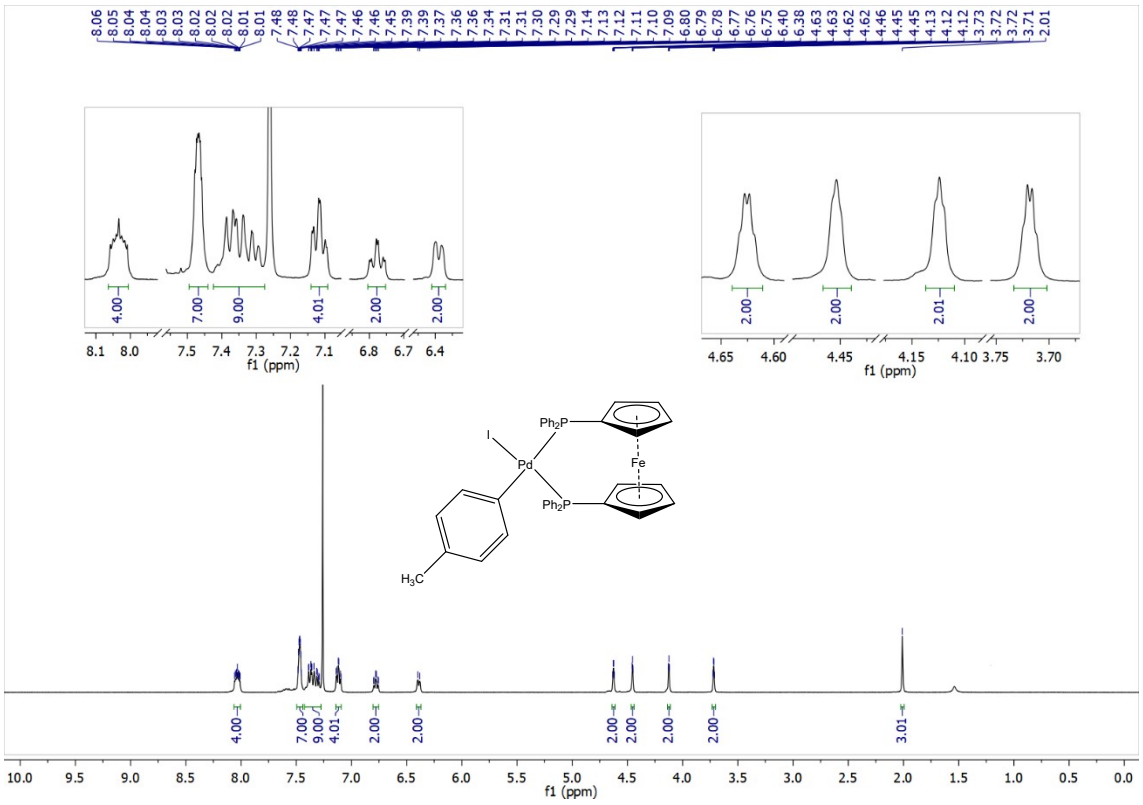

Figure S 32. ^{1}H NMR spectrum of **4d** in $CDCl_3$ at 298 K.

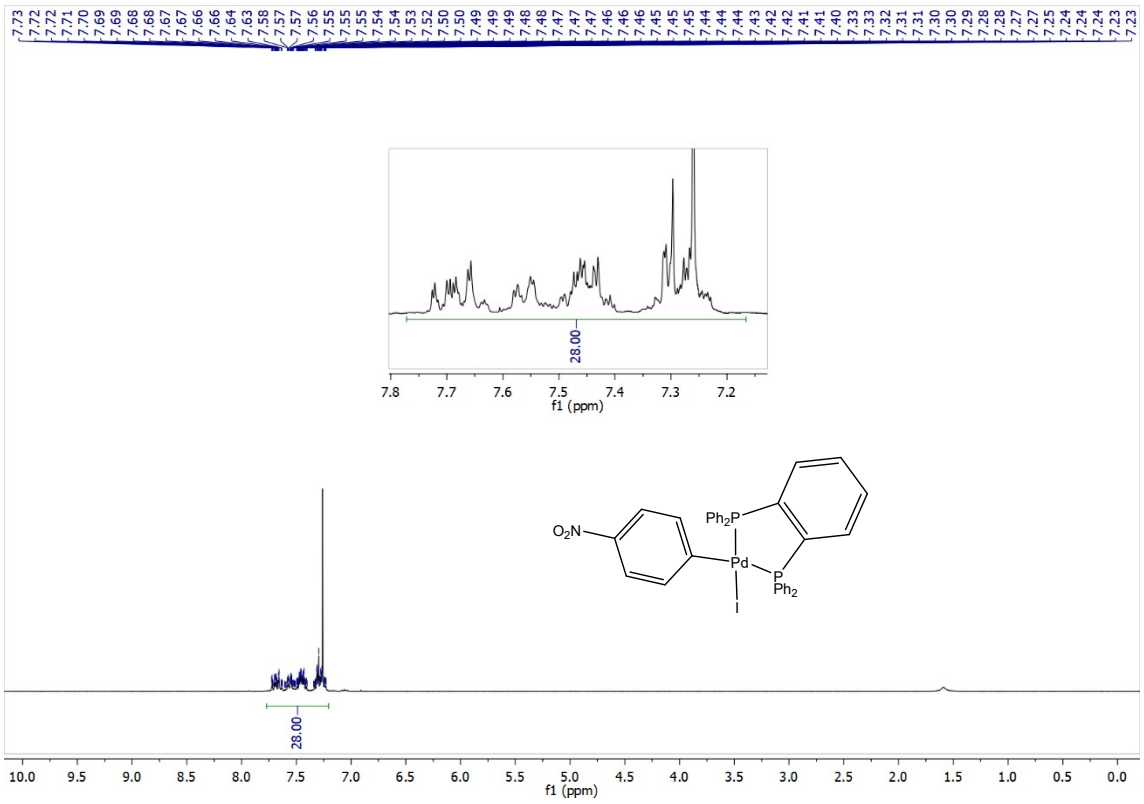

Figure S33. ^{1}H NMR spectrum of **5a** in $CDCl_3$ at 298 K.

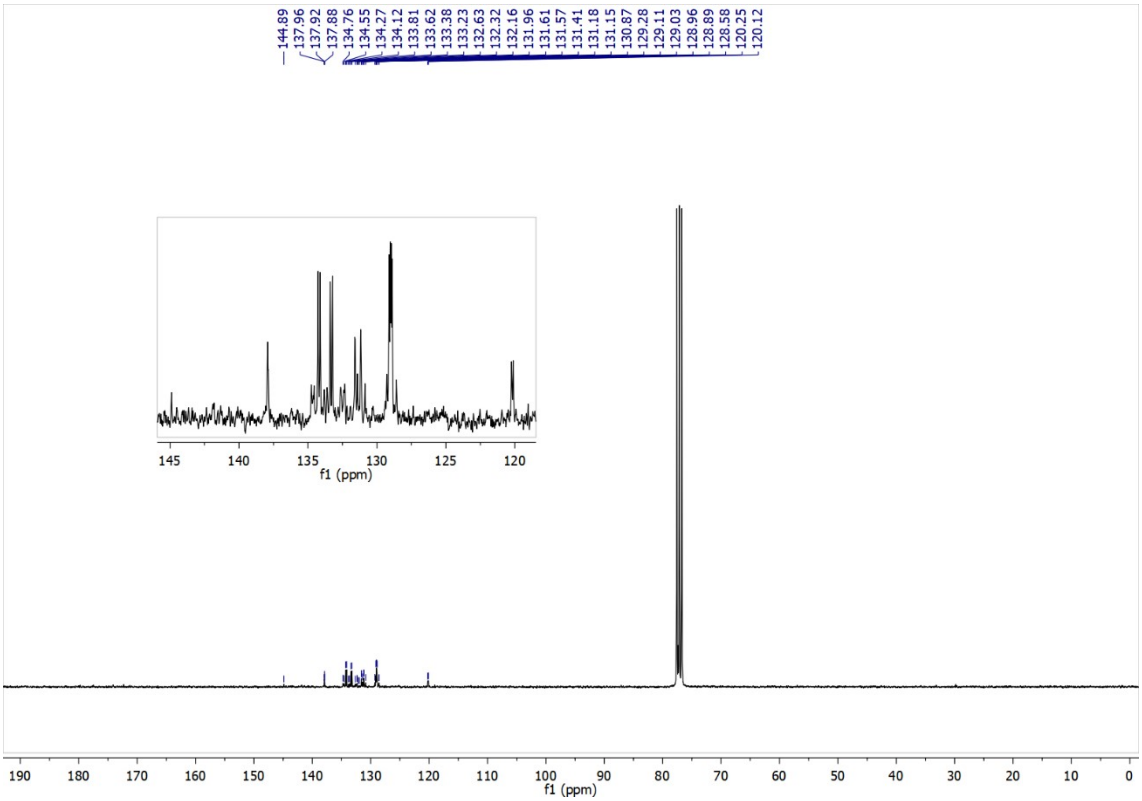

Figure S34. $^{13}C\{^{1}H\}$ NMR spectrum of **5a** in $CDCl_3$ at 298 K.

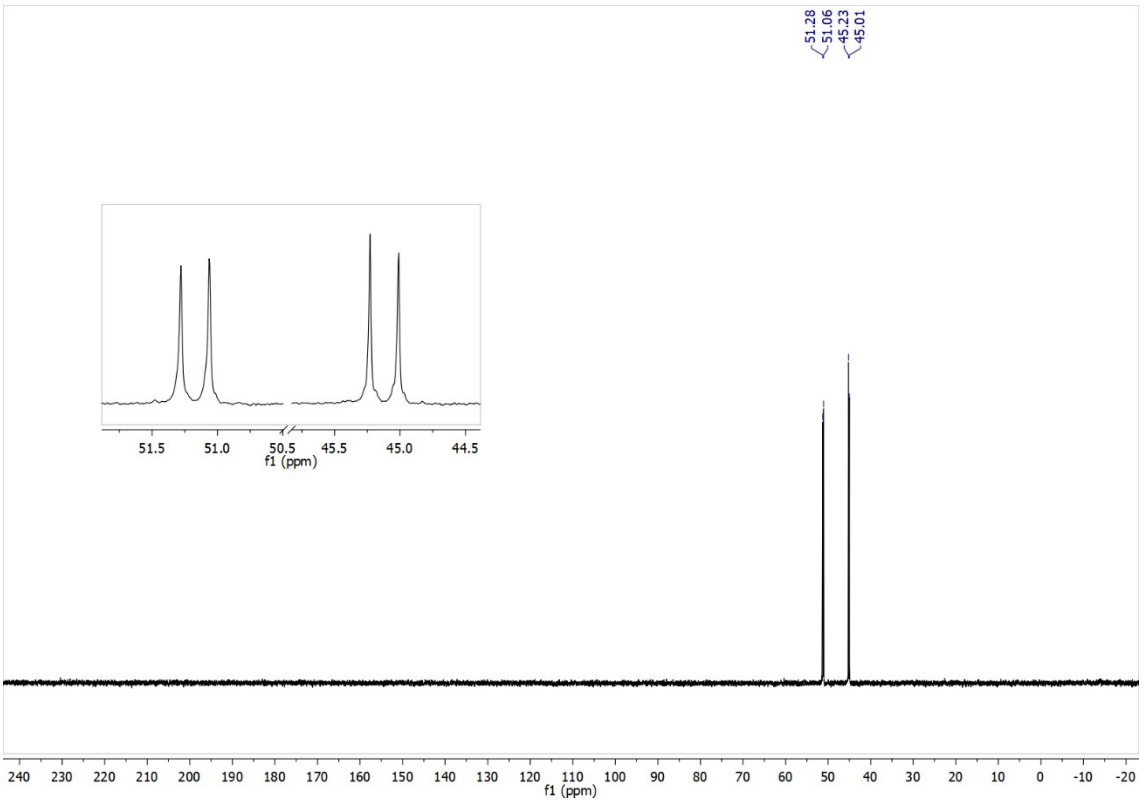

Figure S35. $^{31}P\{^{1}H\}$ NMR spectrum of **5a** in $CDCl_3$ at 298 K.

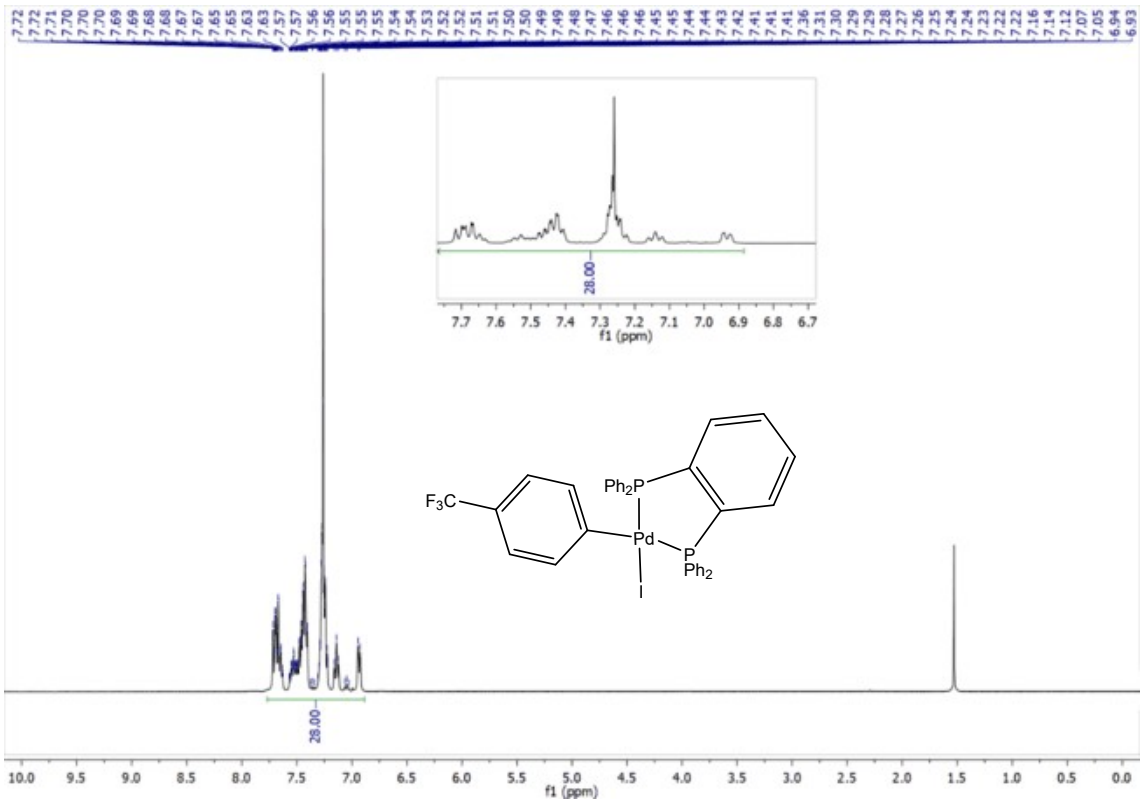

Figure S36. ^{1}H NMR spectrum of **5b** in $CDCl_3$ at 298 K.

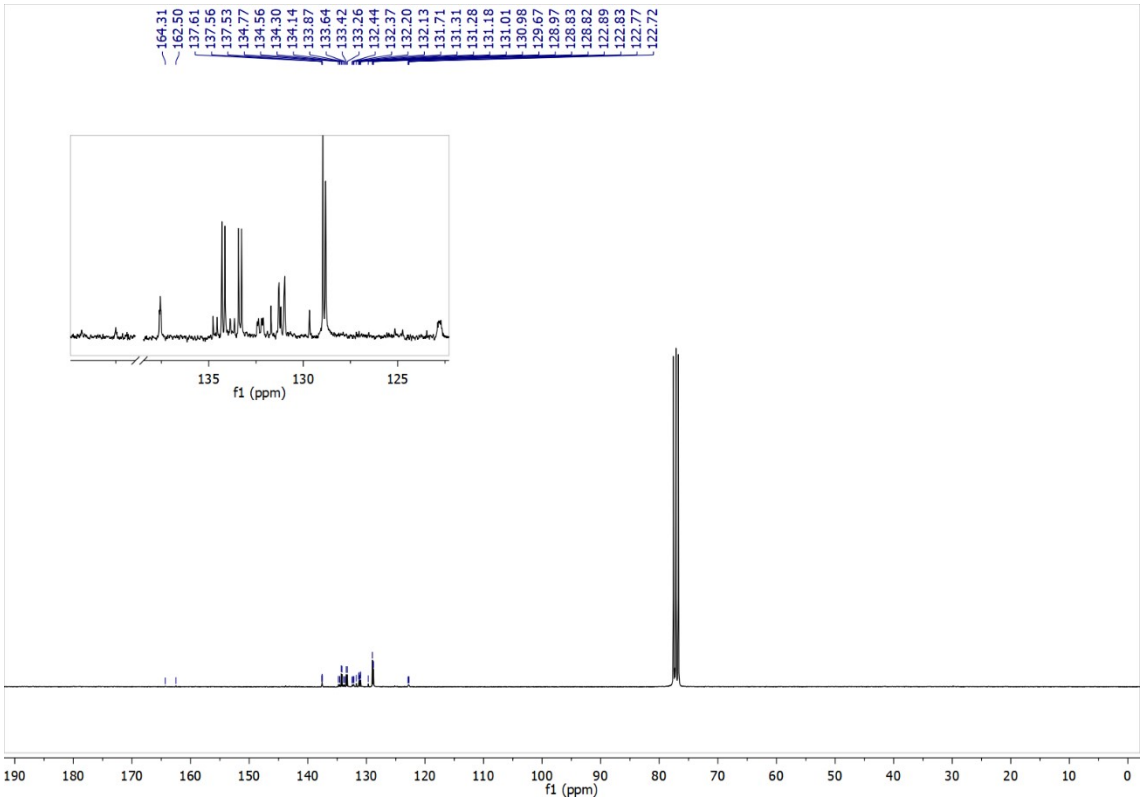

Figure S37. $^{13}C\{^{1}H\}$ NMR spectrum of **5b** in $CDCl_3$ at 298 K.

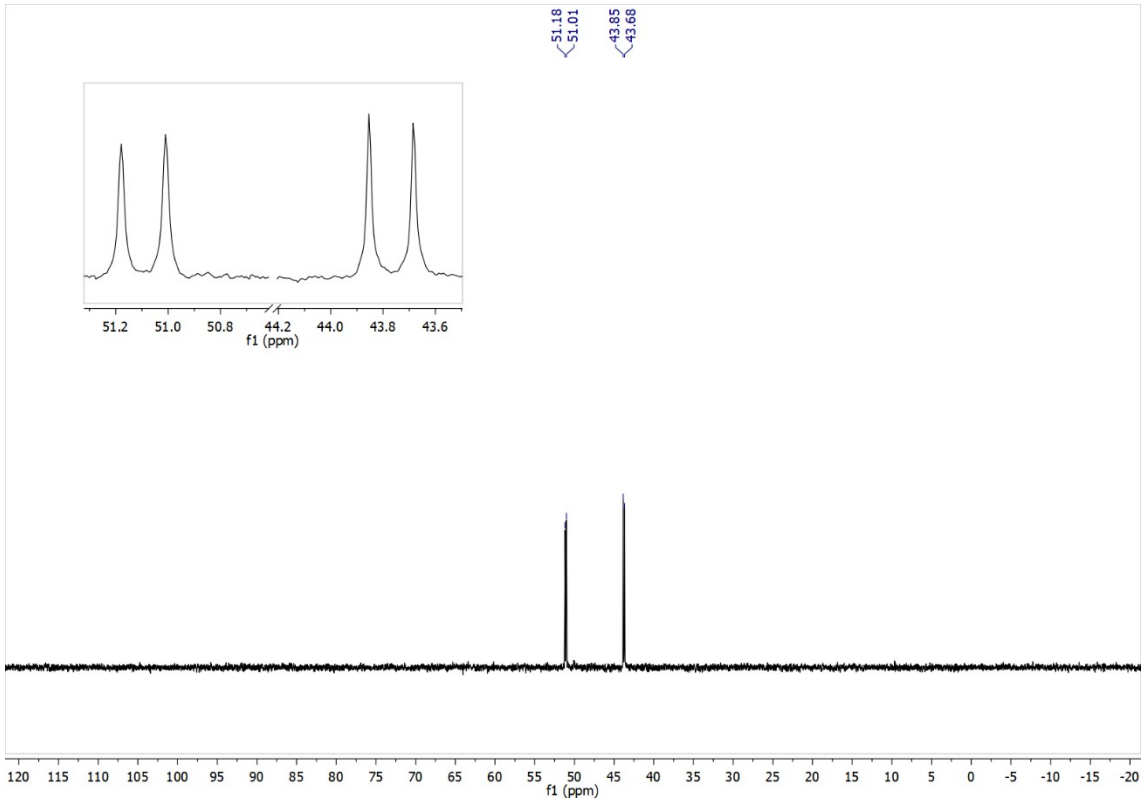

Figure S 38. $^{31}P\{^{1}H\}$ NMR spectrum of **5b** in $CDCl_3$ at 298 K.

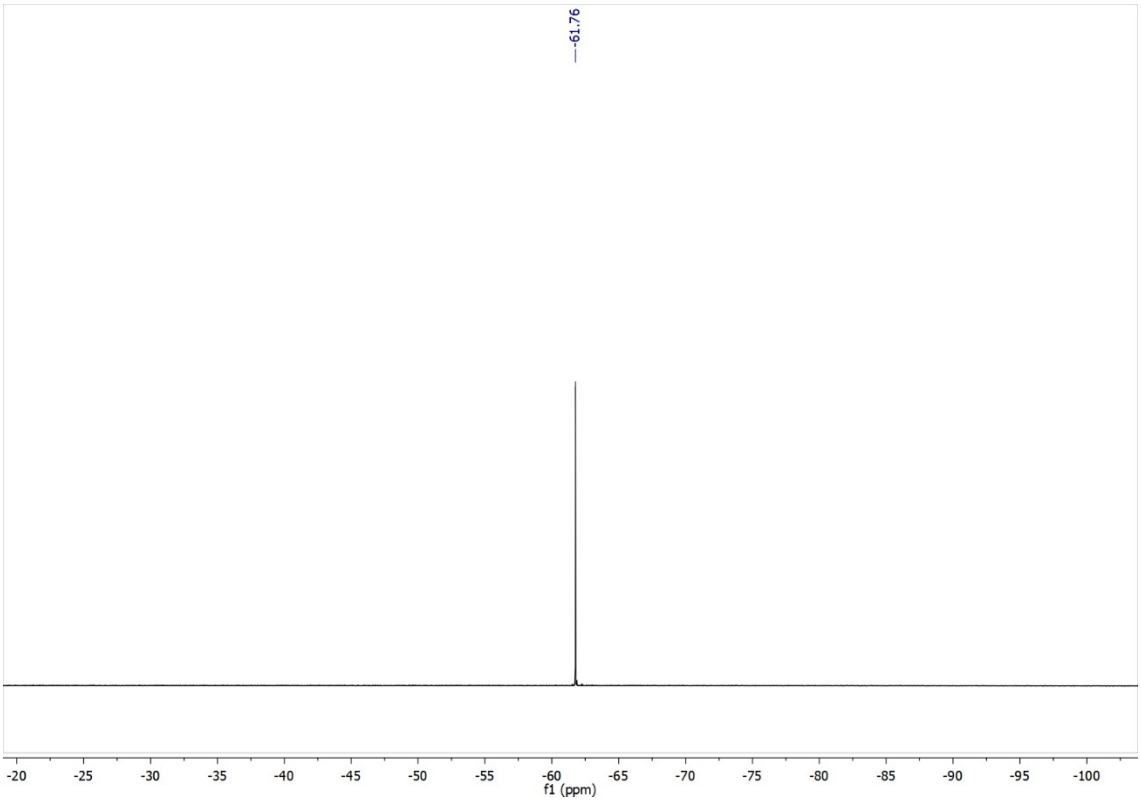

Figure S39. $^{19}F\{^{1}H\}$ NMR spectrum of **5b** in $CDCl_3$ at 298 K.

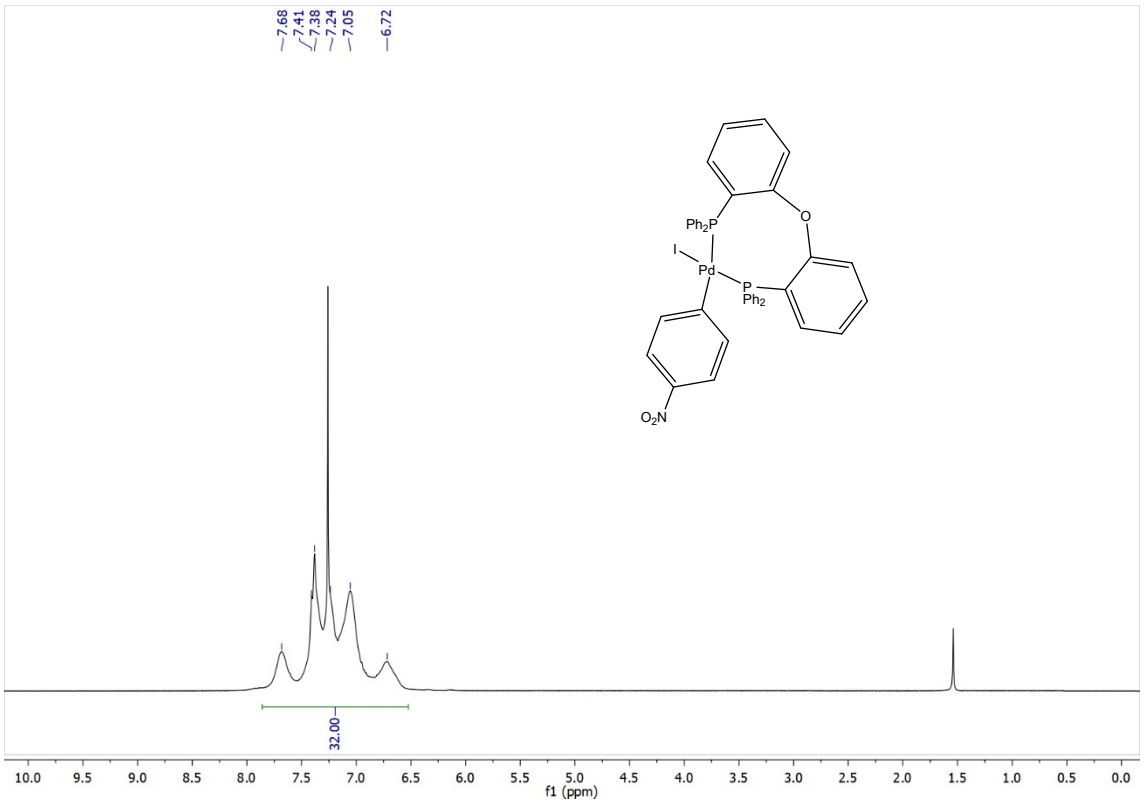

Figure S40. ^{1}H NMR spectrum of **6a** in $CDCl_3$ at 298 K.

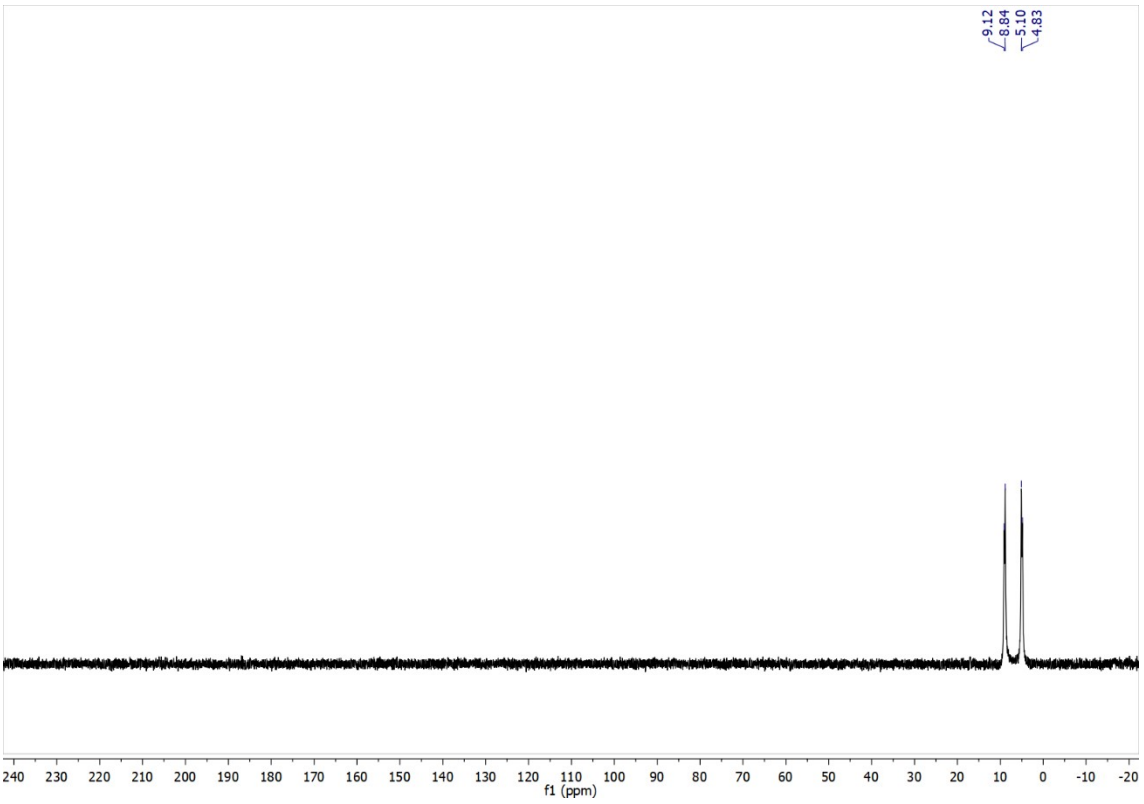

Figure S41. $^{31}P\{^{1}H\}$ NMR spectrum of **6a** in $CDCl_3$ at 298 K.

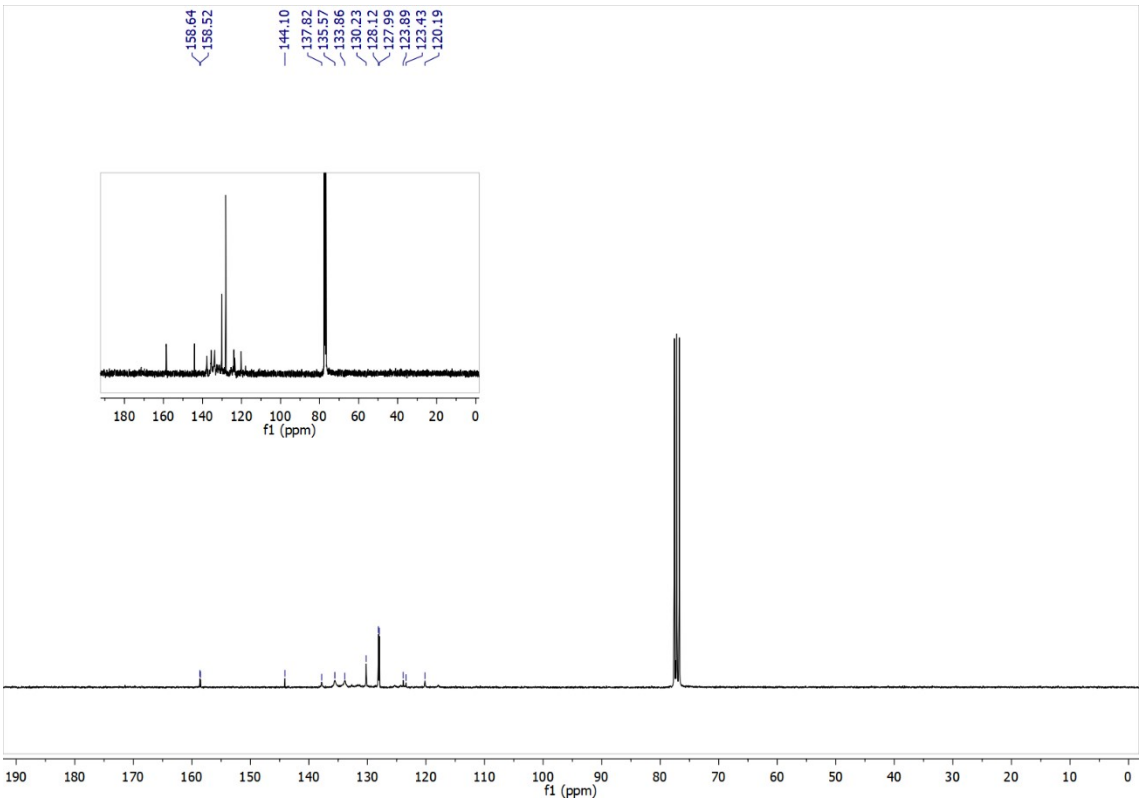

Figure S42. $^{13}C\{^{1}H\}$ NMR spectrum of **6a** in $CDCl_3$ at 298 K.

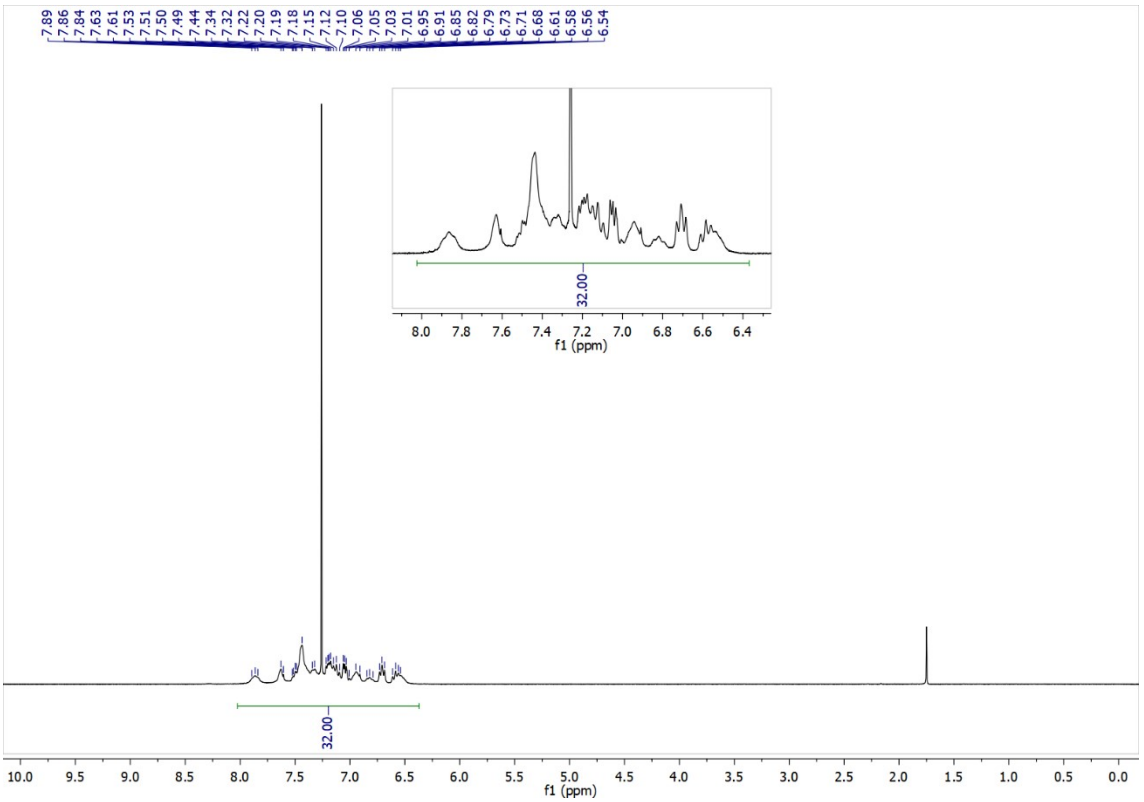

Figure S43. ^{1}H NMR spectrum of **6a** in $CDCl_3$ at 233 K.

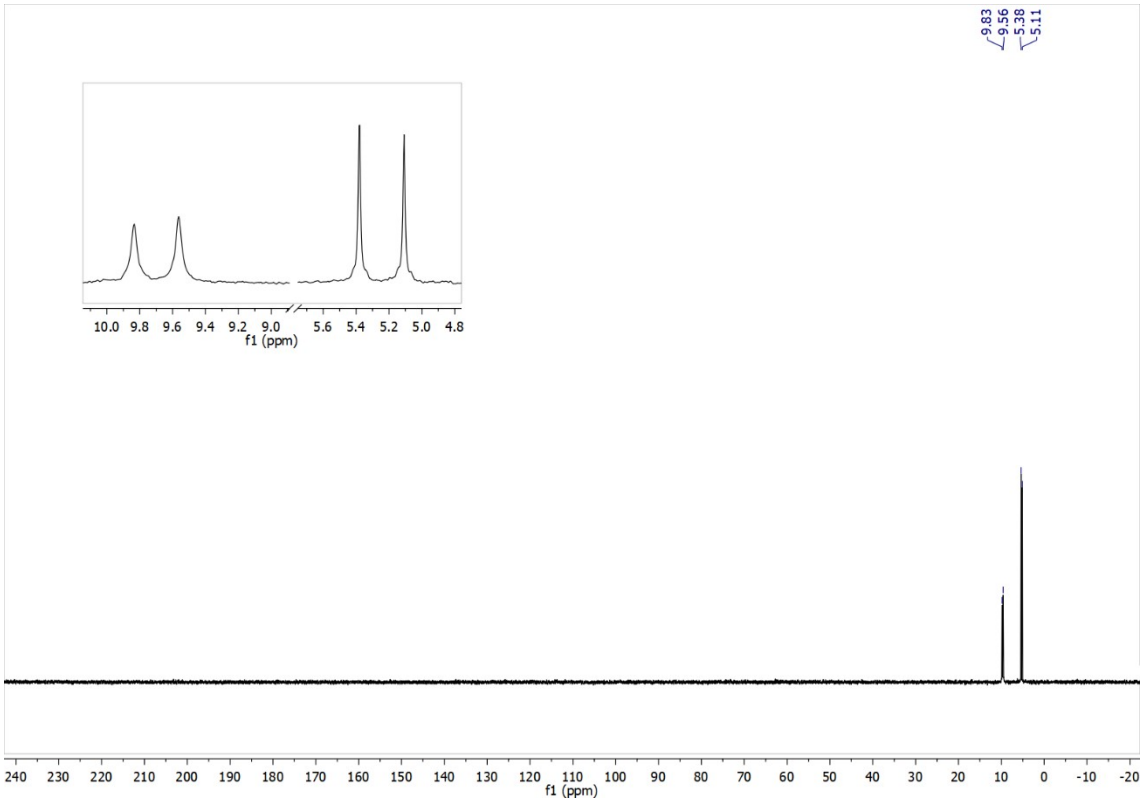

Figure S44. $^{31}P\{^{1}H\}$ NMR spectrum of **6a** in $CDCl_3$ at 233 K.

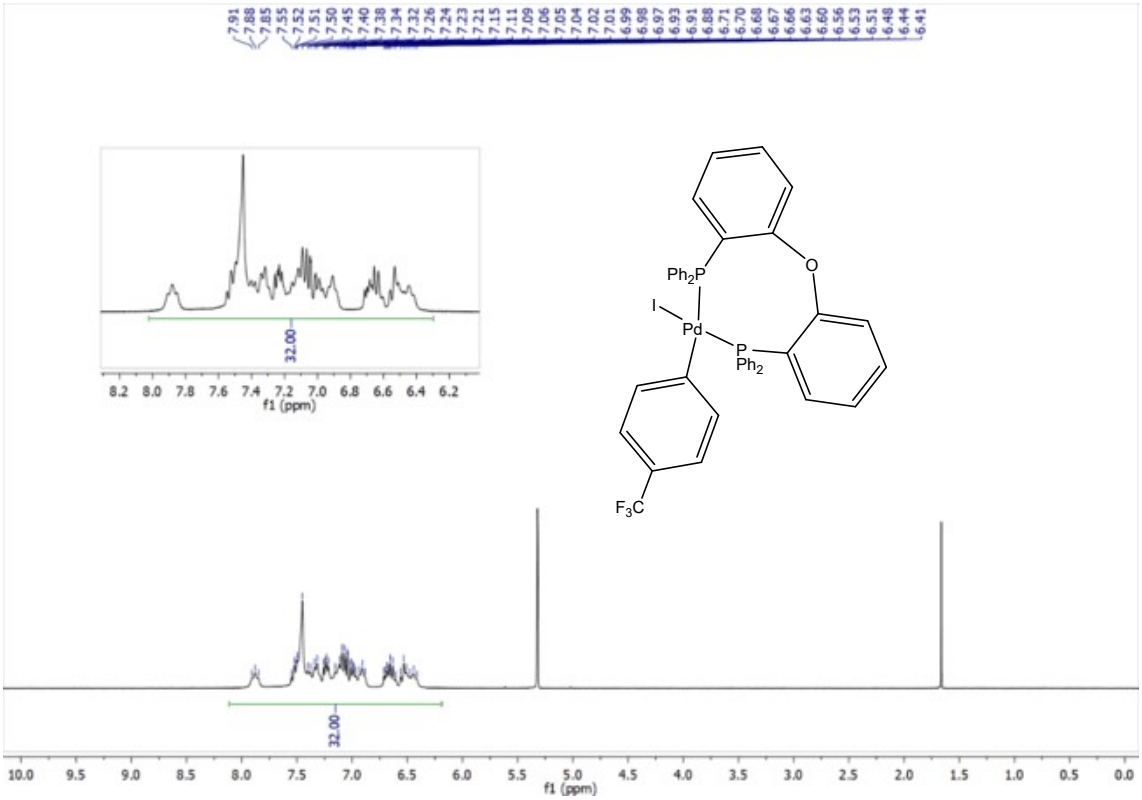

Figure S45. ^{1}H NMR spectrum of **6b** in CD_2Cl_2 at 233 K.

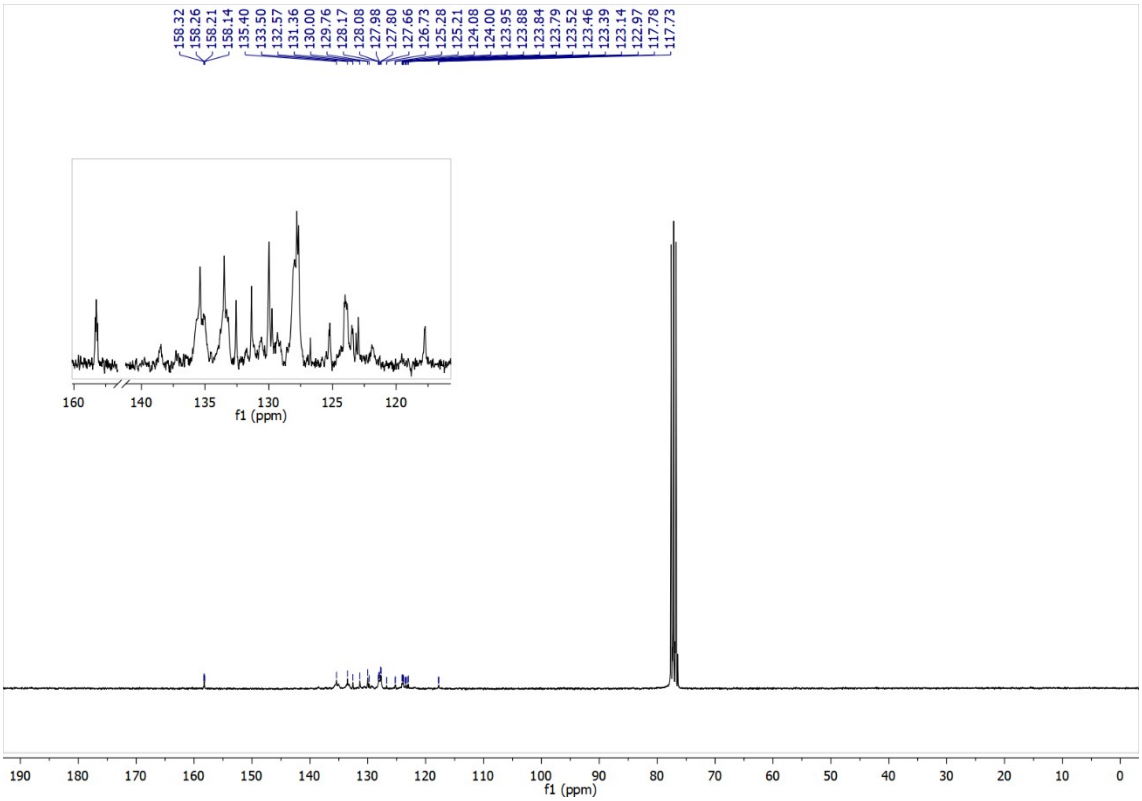

Figure S46. $^{13}C\{^{1}H\}$ NMR spectrum of **6b** in $CDCl_3$ at 233 K.

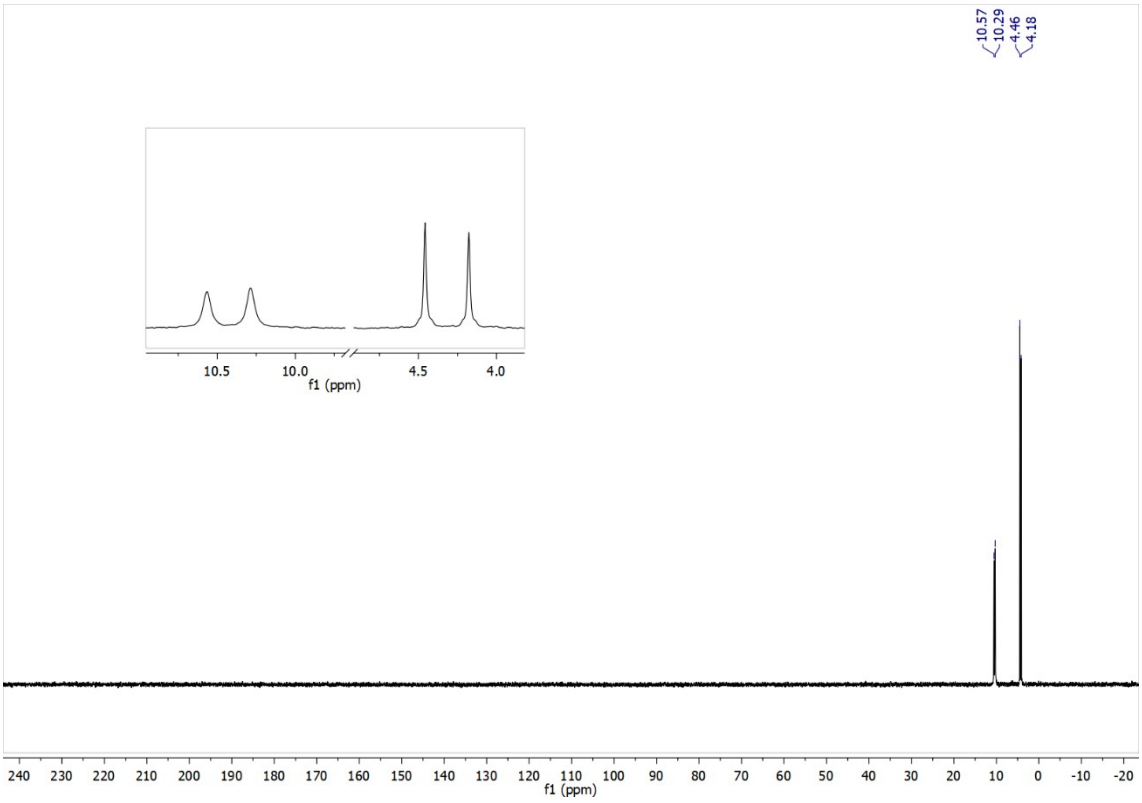

Figure S47. $^{31}P\{^{1}H\}$ NMR spectrum of **6b** in CD_2Cl_2 at 233 K.

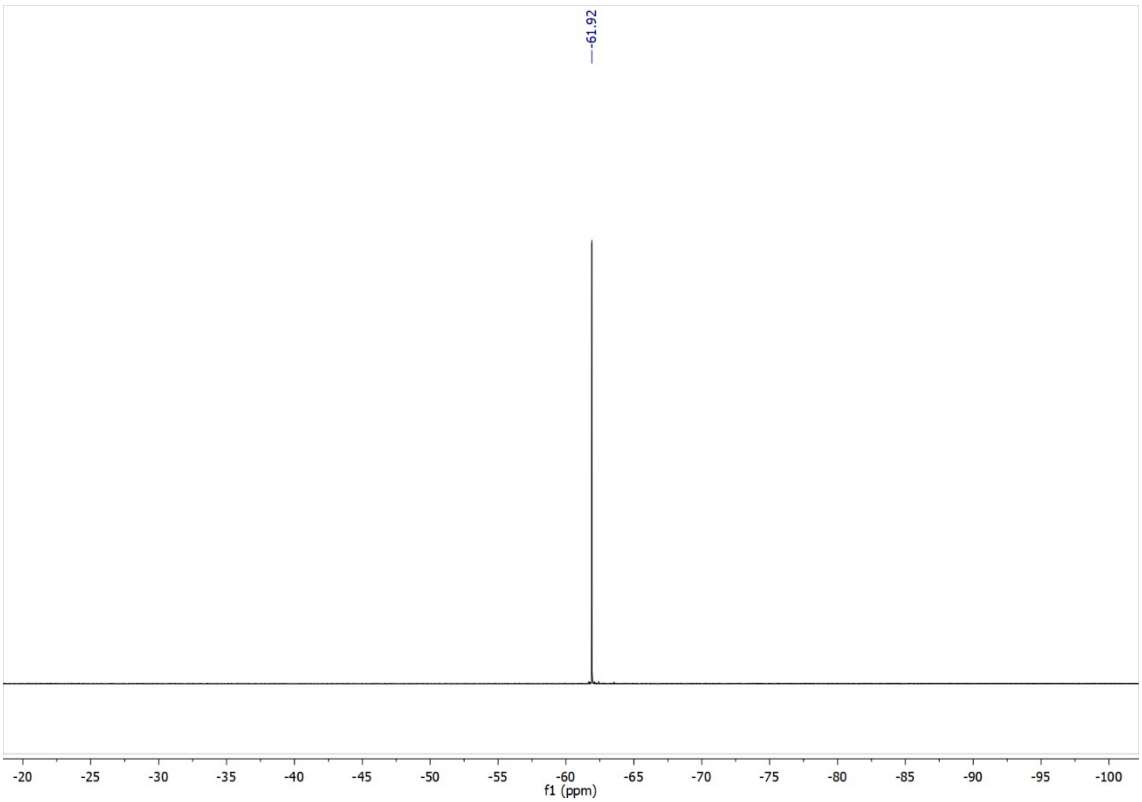

Figure S48. $^{19}F\{^{1}H\}$ NMR spectrum of **6b** in CD_2Cl_2 at 298K.

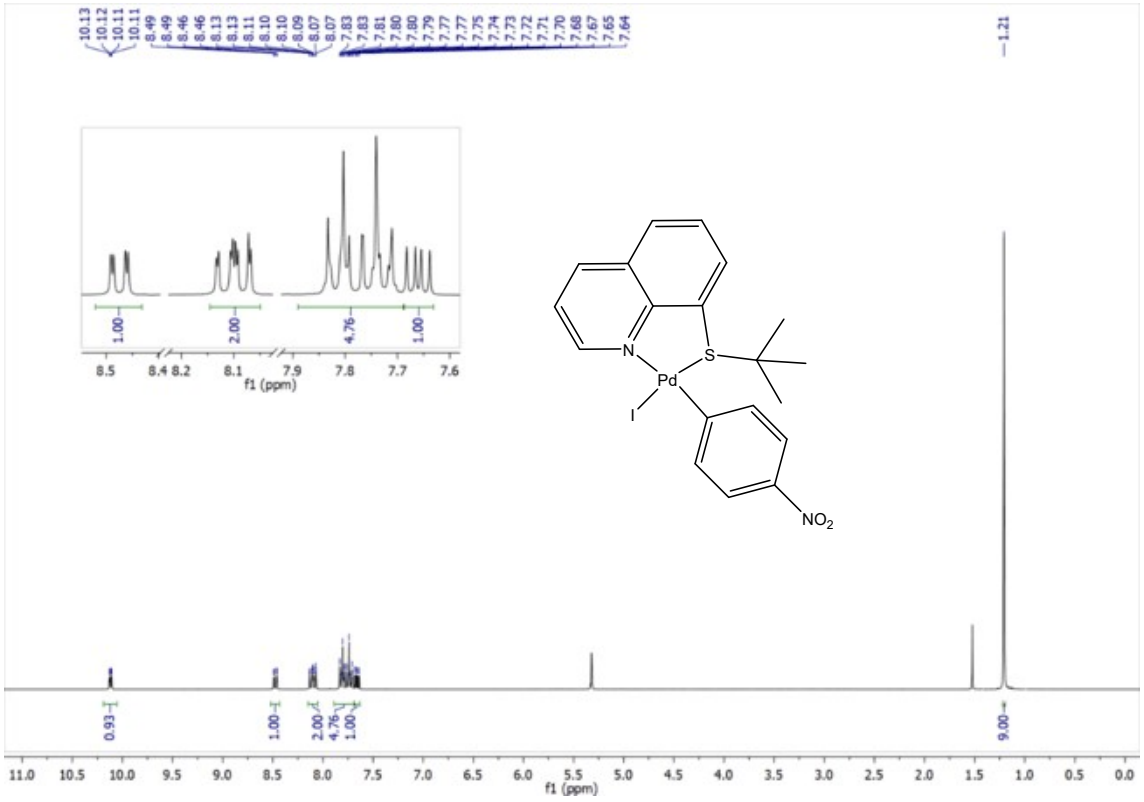

Figure S49. ^{1}H NMR spectrum of **7**-**I** in CD_2Cl_2 at 298 K.

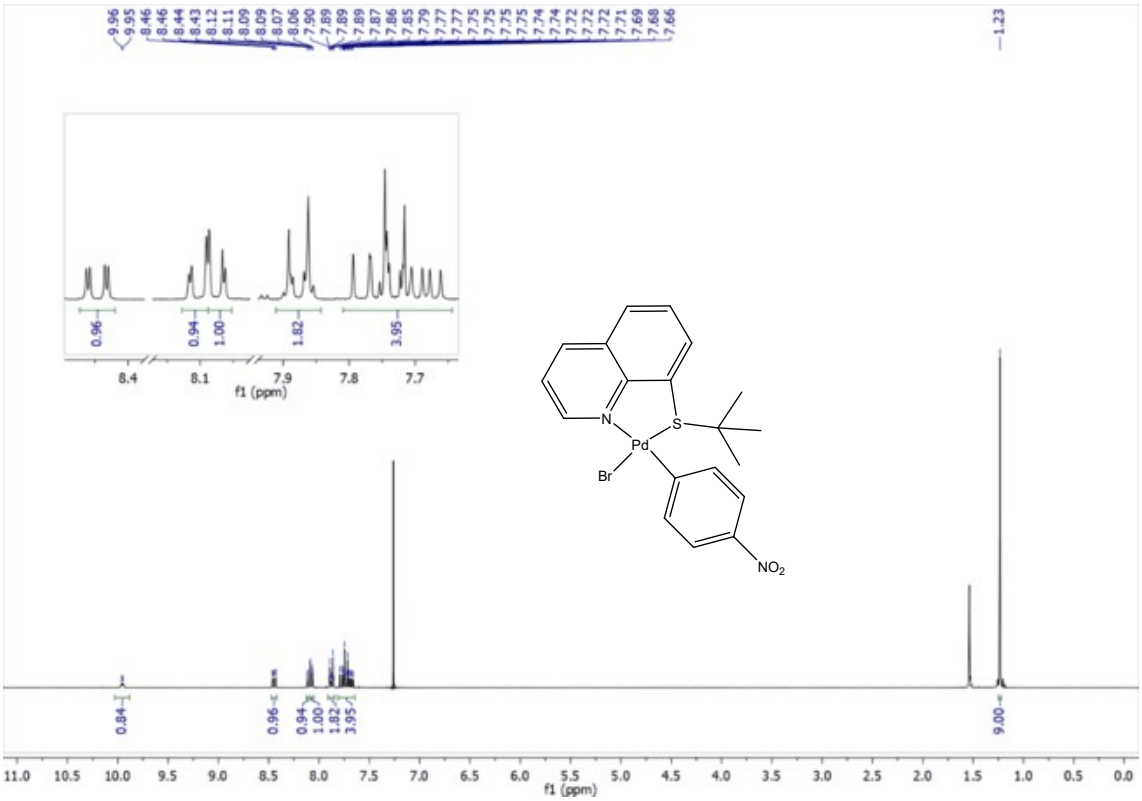

Figure S50. ^{1}H NMR spectrum of **7**-**Br** in $CDCl_3$ at 298 K.

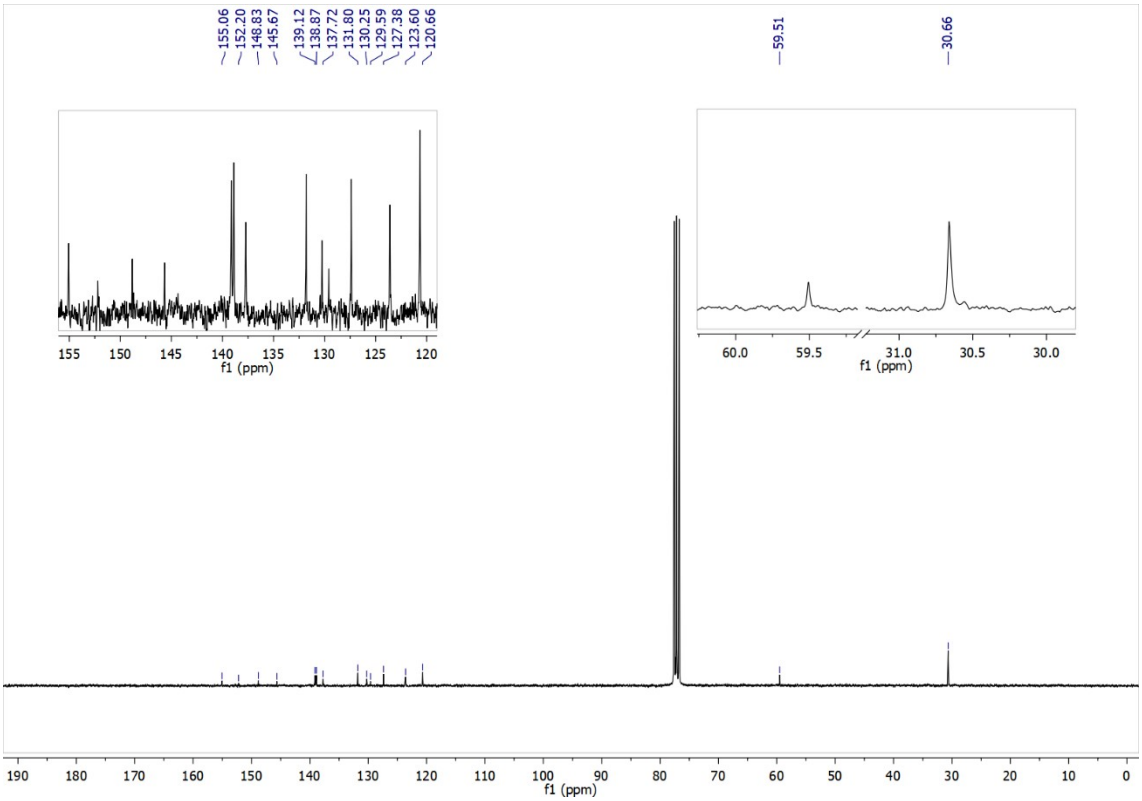

Figure S51. $^{13}C\{^{1}H\}$ NMR spectrum of **7-Br** in $CDCl_3$ at 298 K.

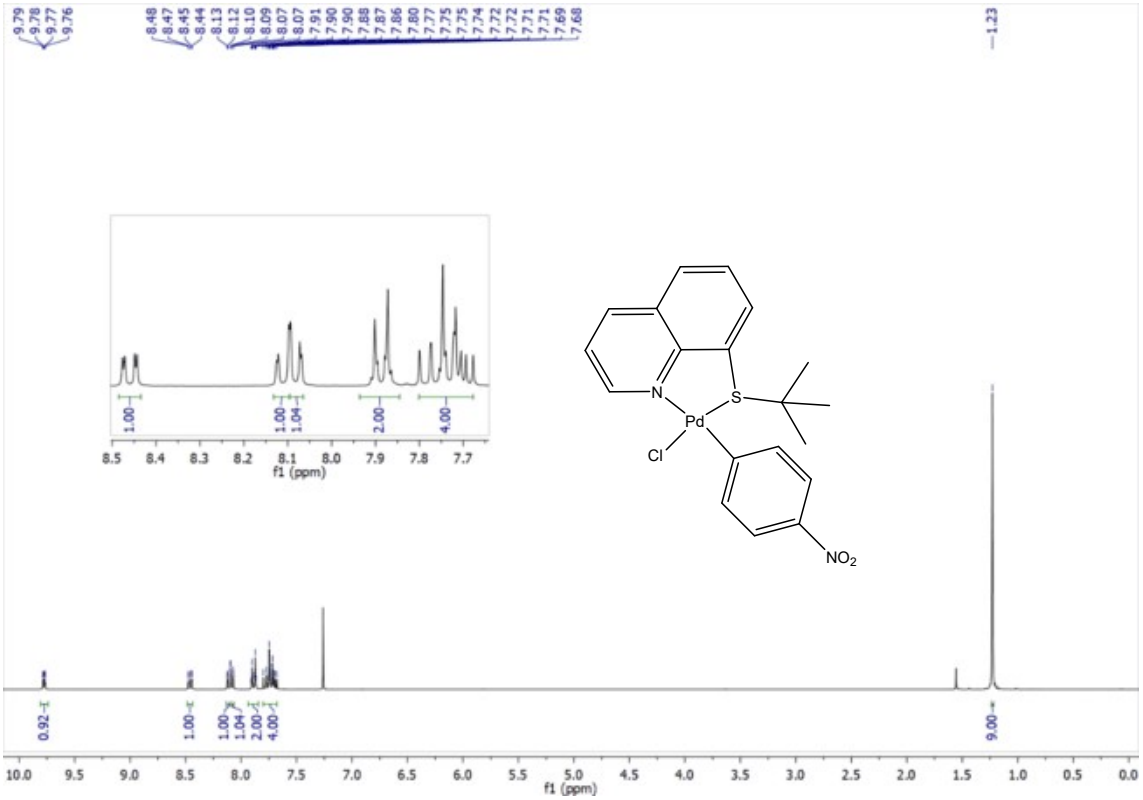

Figure S52. ^{1}H NMR spectrum of **7-Cl** in $CDCl_3$ at 298 K.

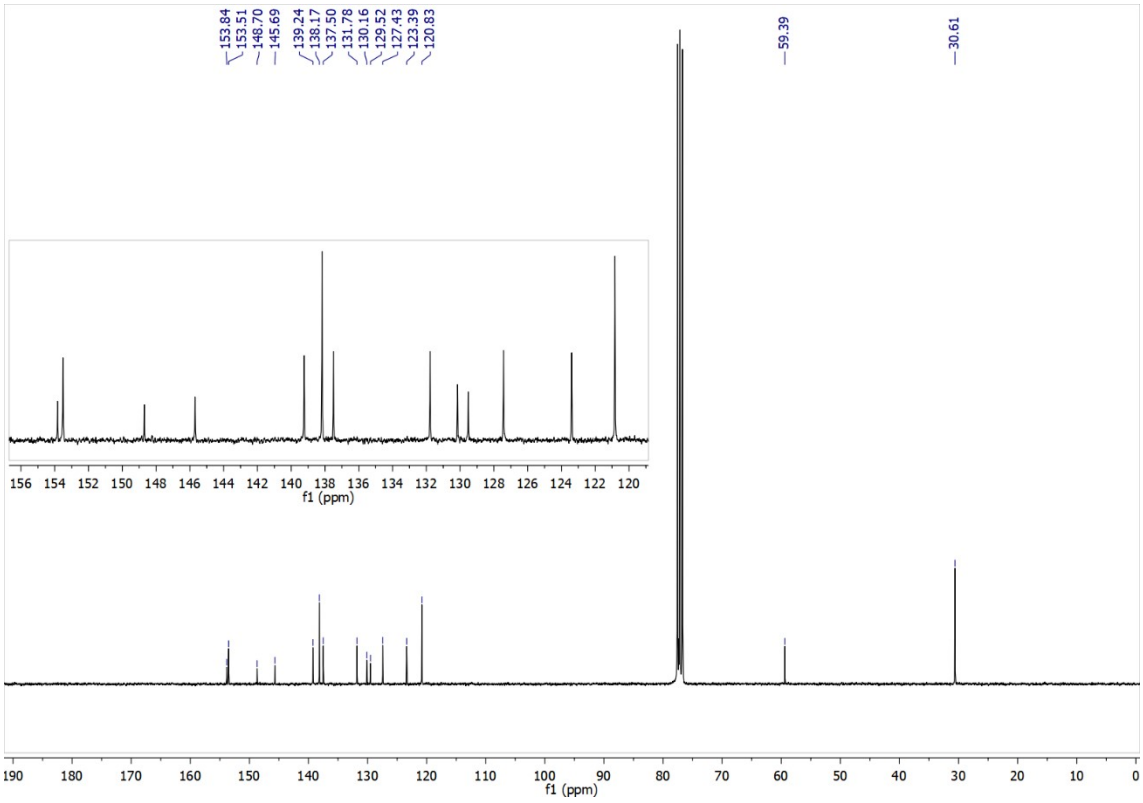

Figure S53. $^{13}C\{^{1}H\}$ NMR spectrum of **7-Cl** in $CDCl_3$ at 298 K.

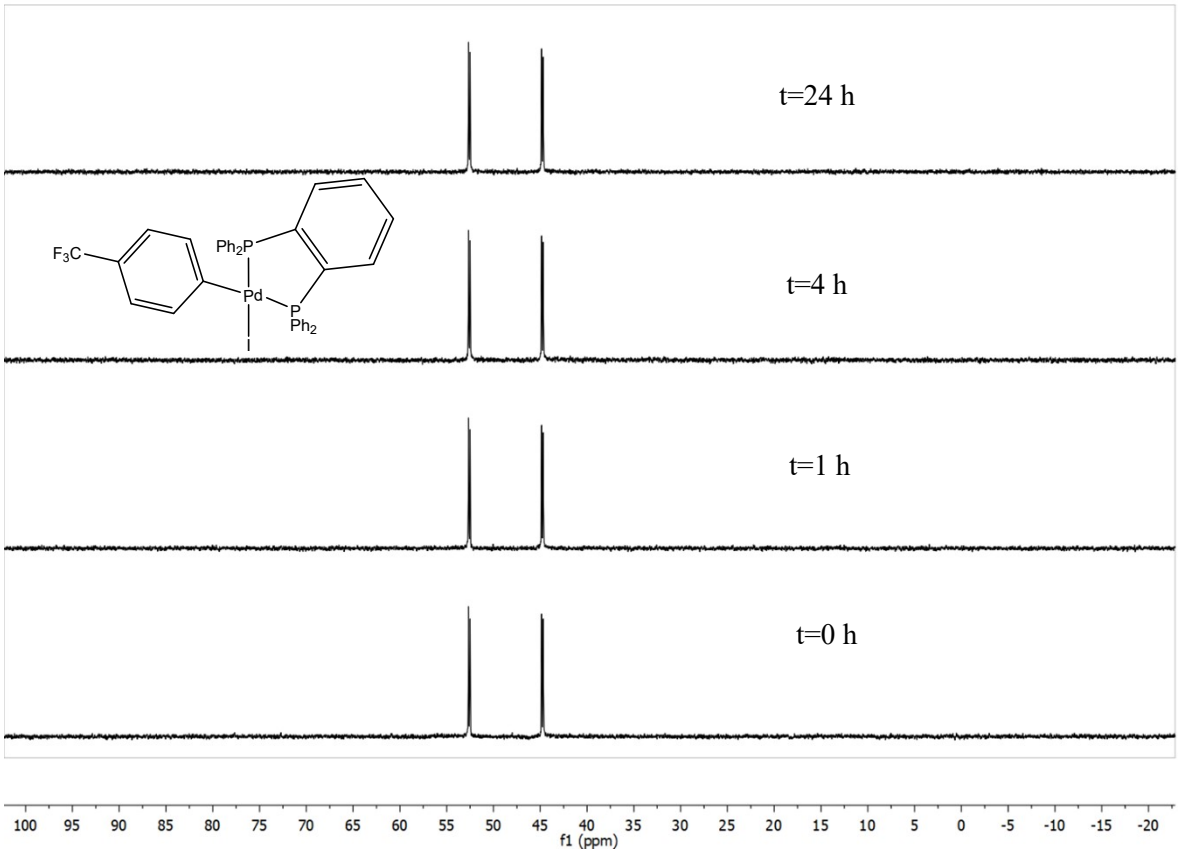

Figure S54. $^{31}P\{^{1}H\}$ NMR spectra of complex **5b** in 1:1 DMSO-d_6/D_2O (t = 0, 1, 4 and 24 h).

IR SPECTRA

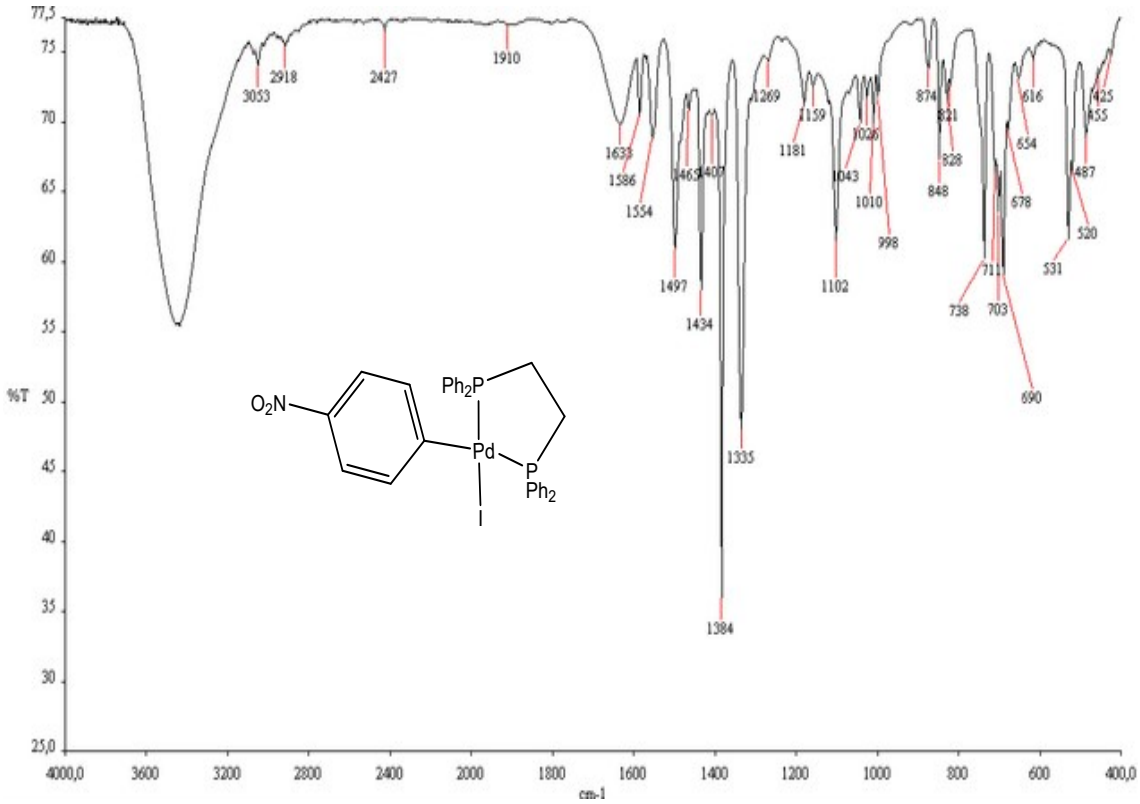

Figure S55. IR spectrum (KBr pellet) of **2a** at 298 K.

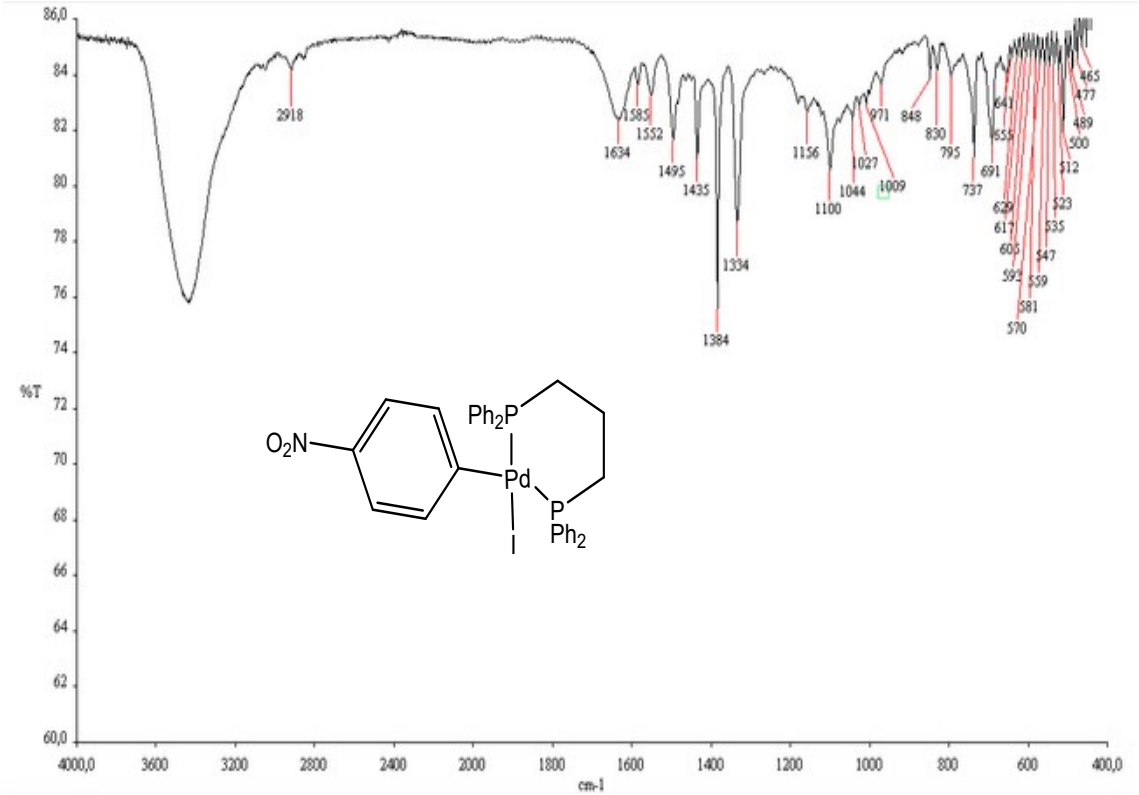

Figure S56. IR spectrum (KBr pellet) of **3a** at 298 K.

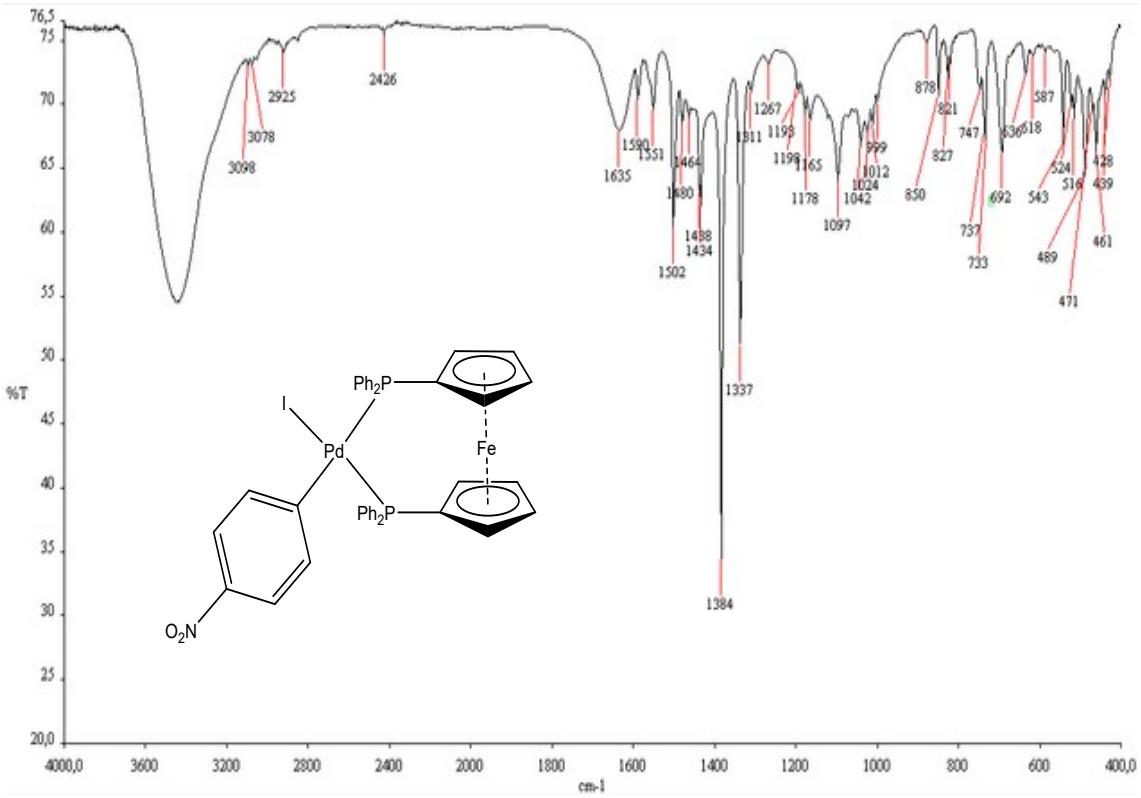

Figure S57. IR spectrum (KBr pellet) of **4a** at 298 K.

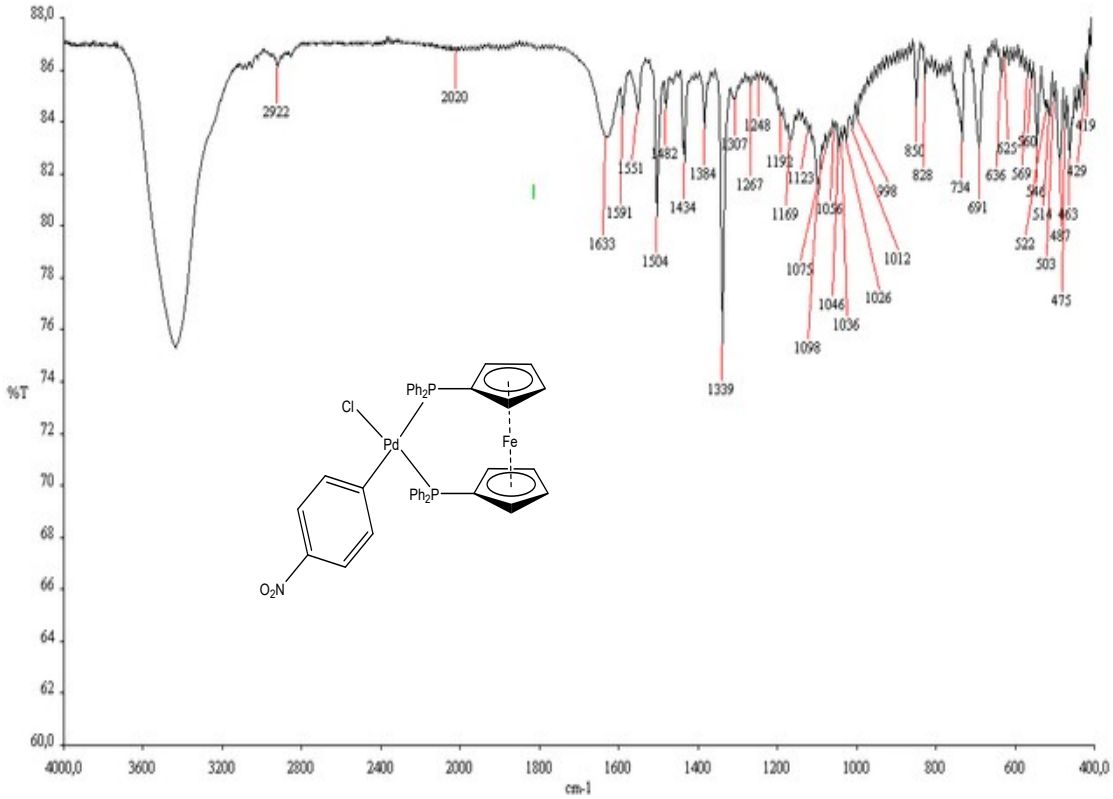

Figure S58. IR spectrum (KBr pellet) of **4a-Cl** at 298 K.

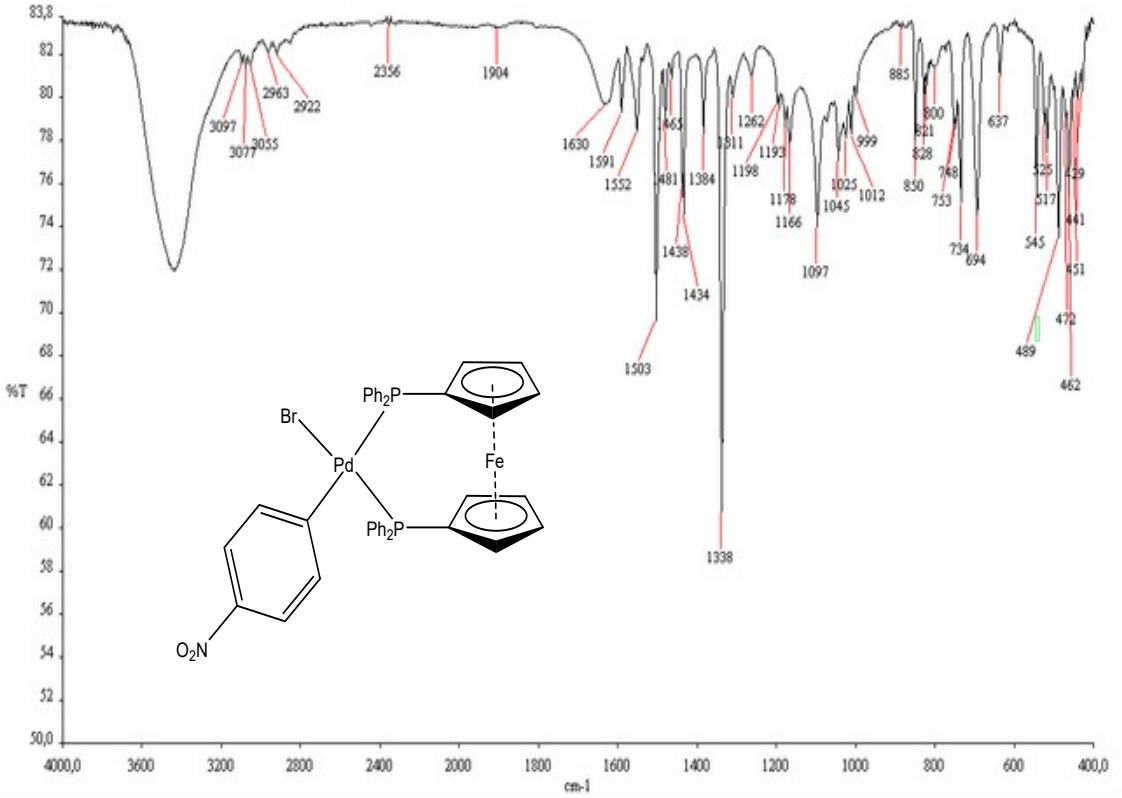

Figure S59. IR spectrum (KBr pellet) of **4a-Br** at 298 K.

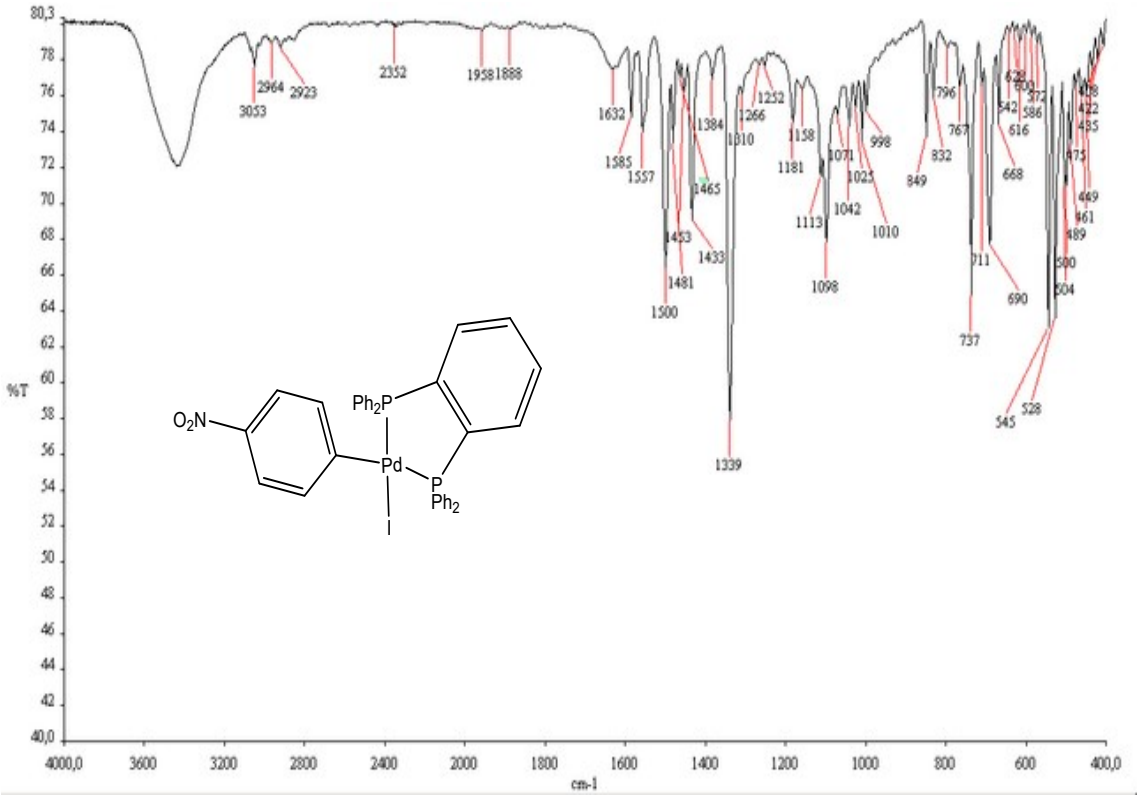

Figure S60. IR spectrum (KBr pellet) of **5a** at 298 K.

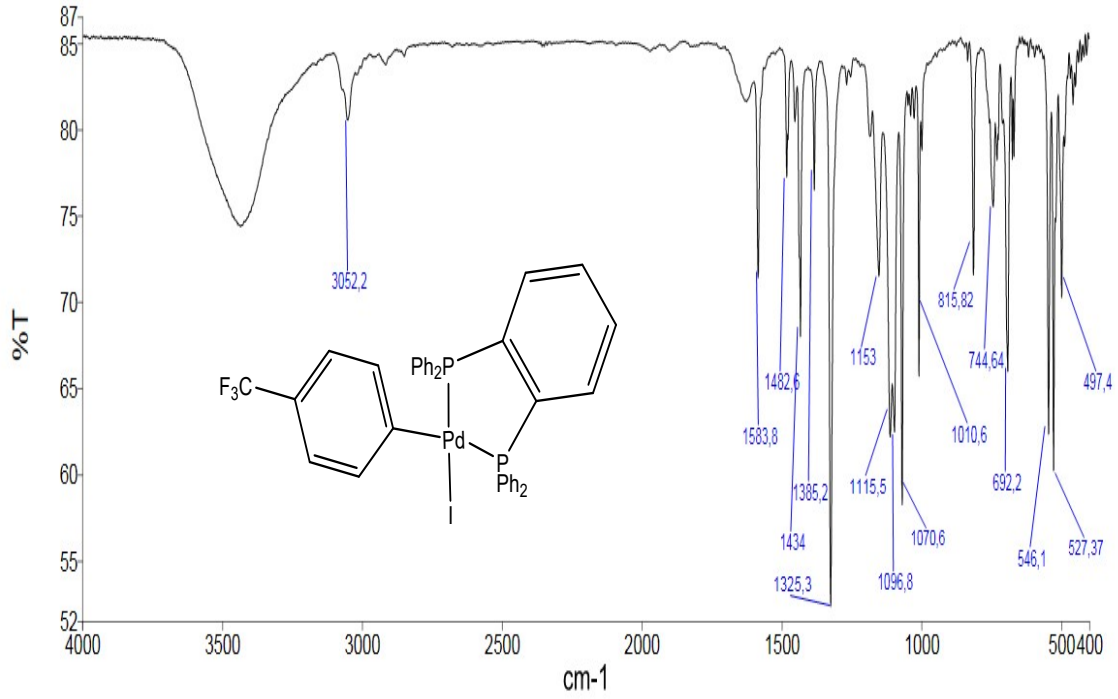

Figure S61. IR spectrum (KBr pellet) of **5b** at 298 K.

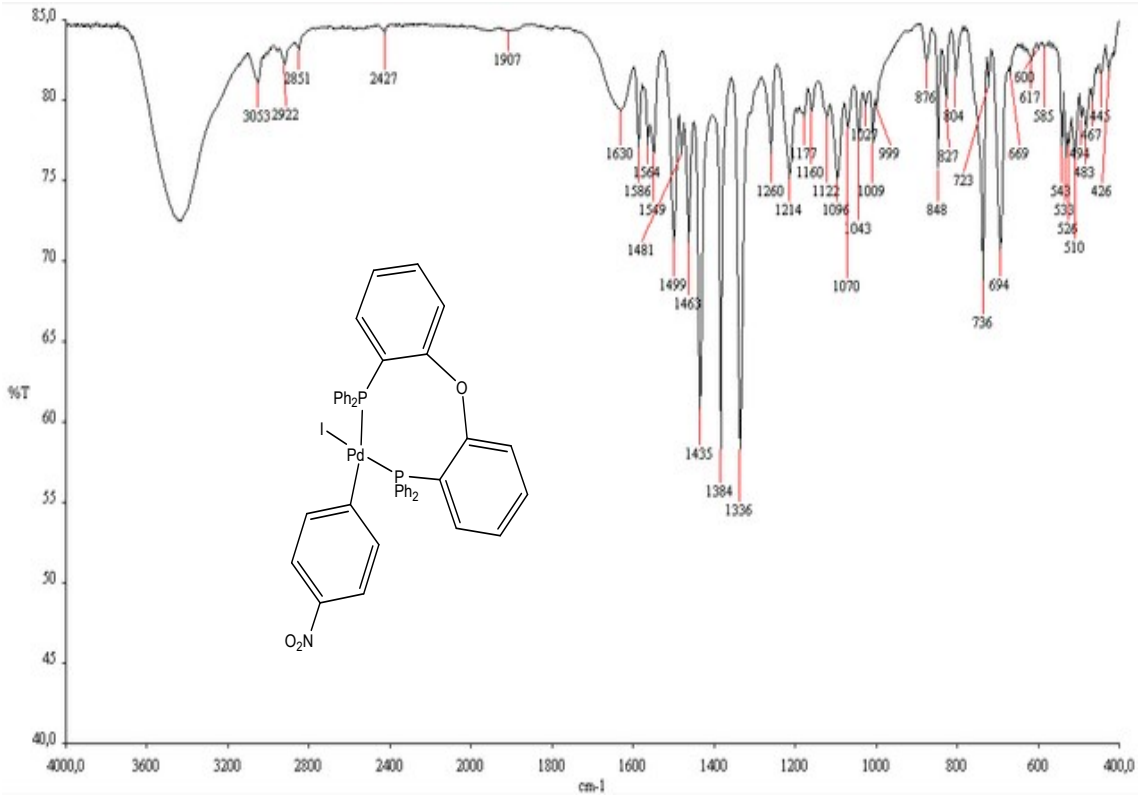

Figure S62. IR spectrum (KBr pellet) of **6a** at 298 K.

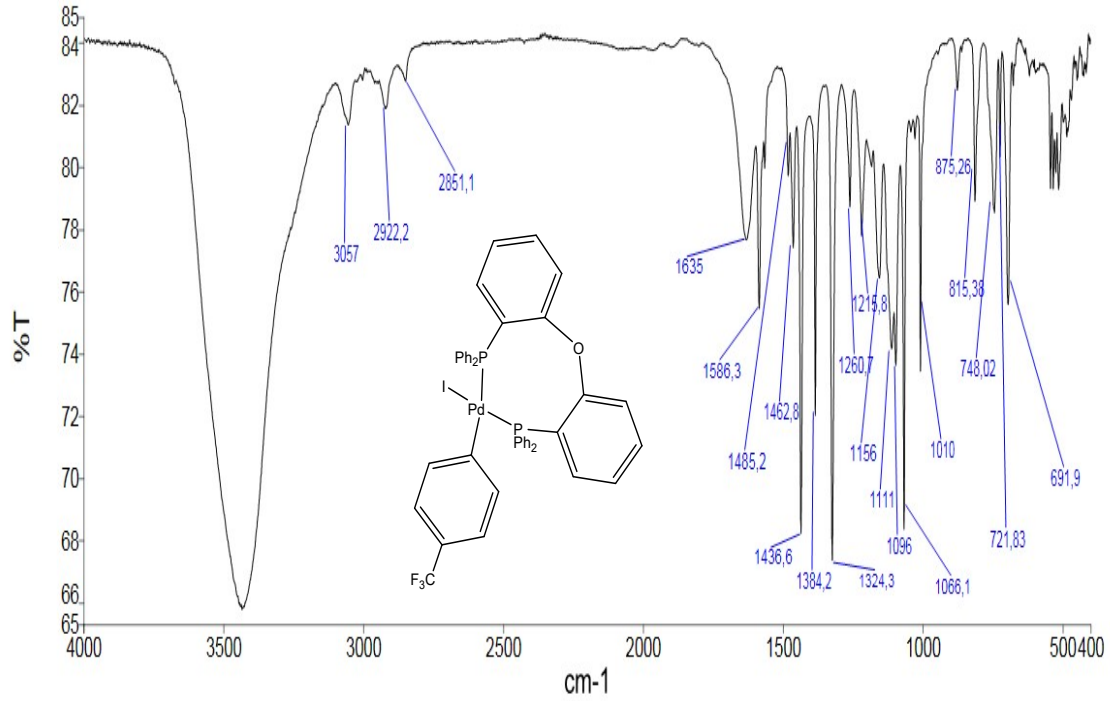

Figure S63. IR spectrum (KBr pellet) of **6b** at 298 K.

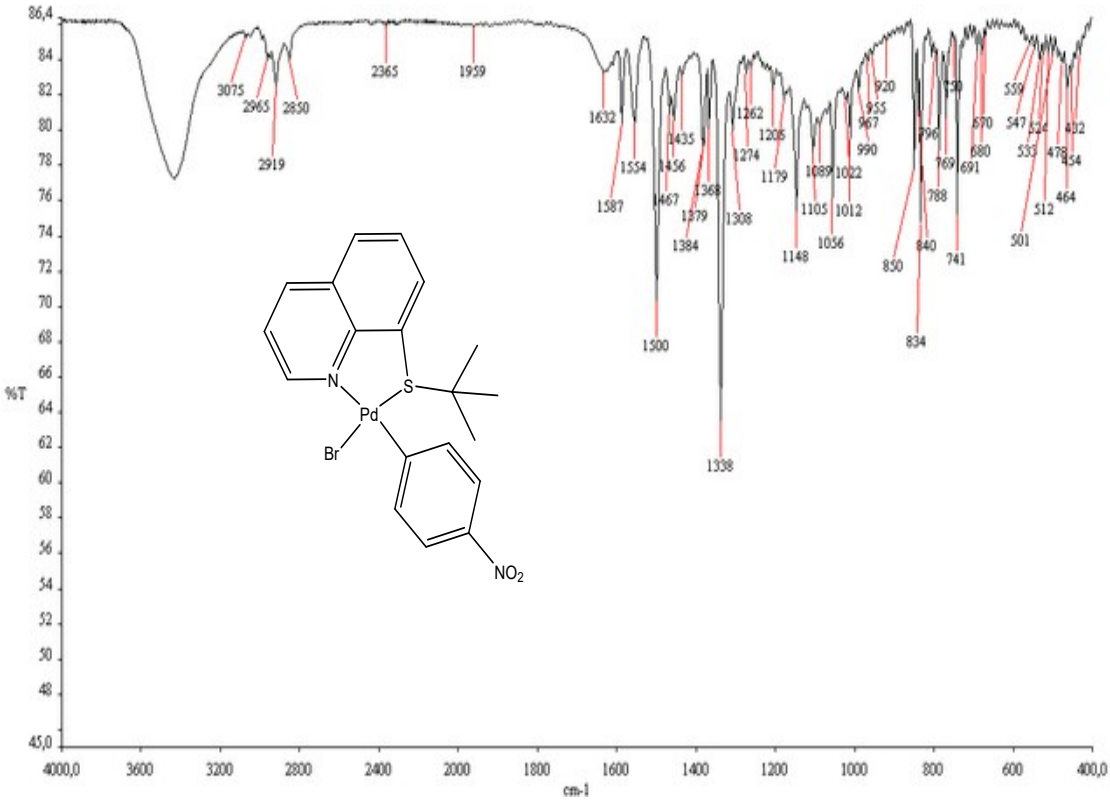

Figure S64. IR spectrum (KBr pellet) of **7-Br** at 298 K.

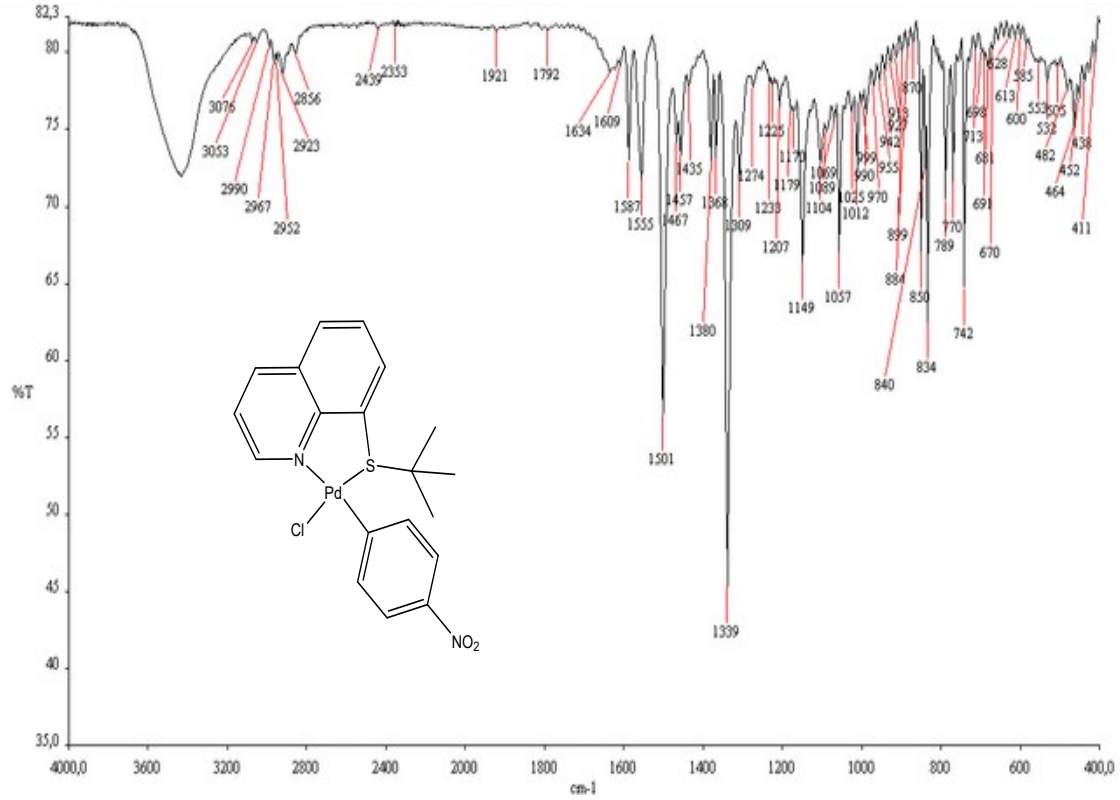

Figure S65. IR spectrum (KBr pellet) of **7-Cl** at 298 K.

HRMS SPECTRA

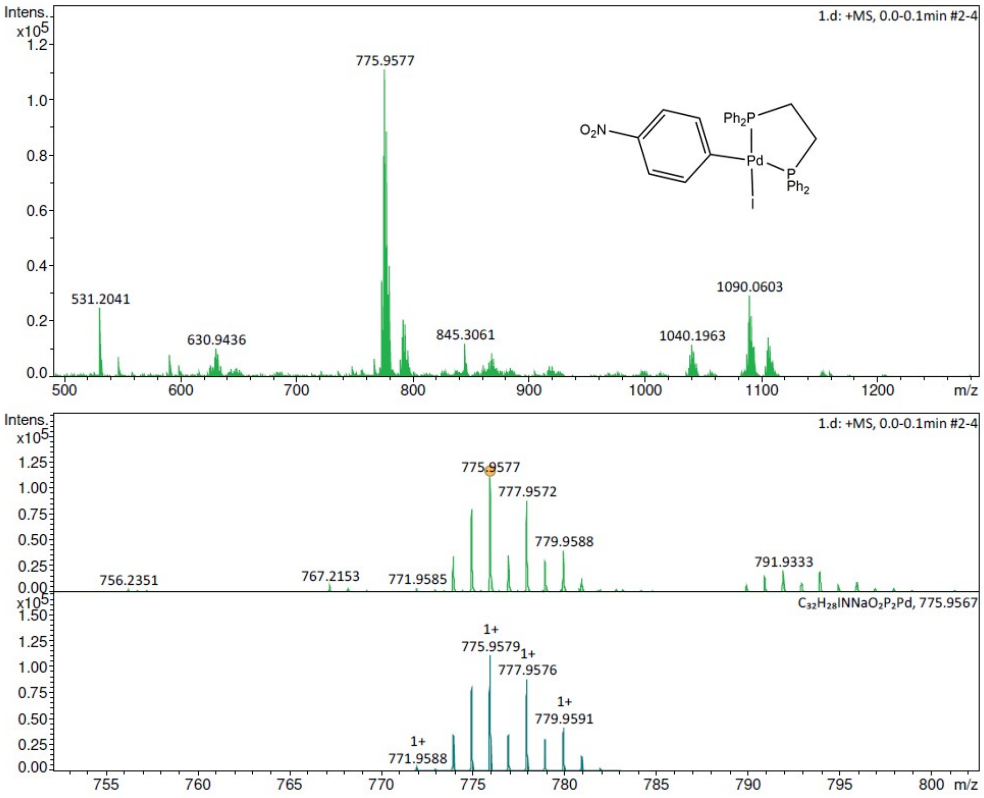

Figure S66. HRMS spectrum of **2a**.

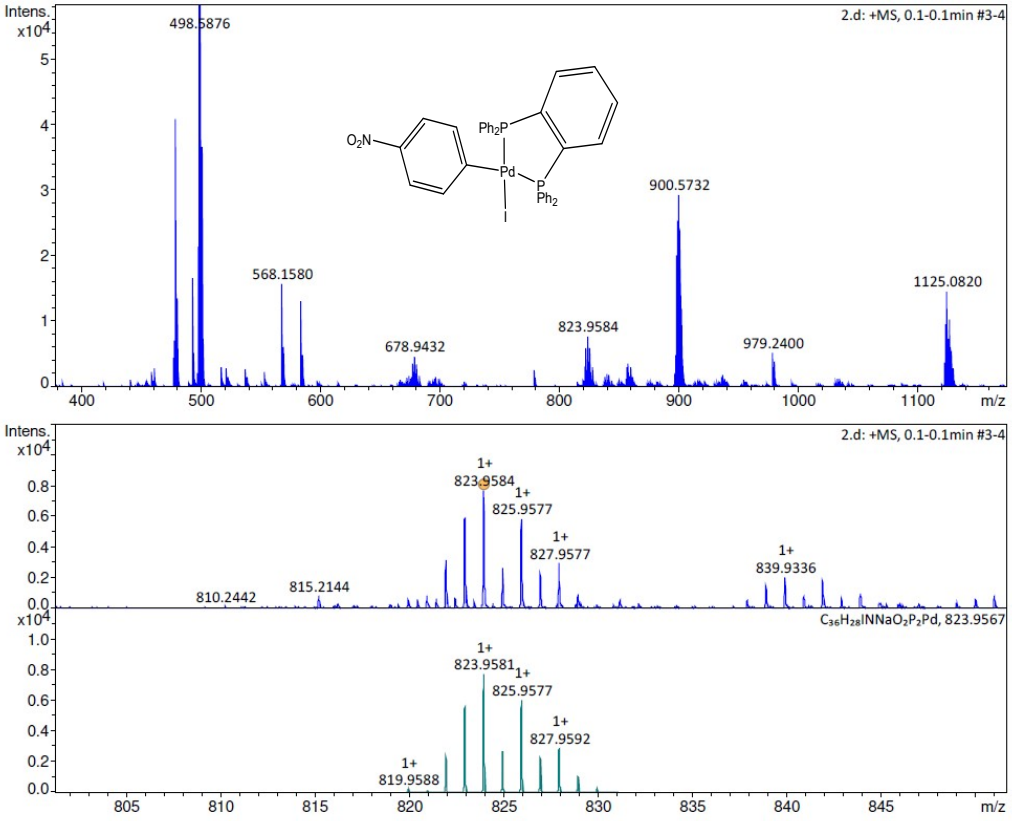

Figure S67 HRMS spectrum of **5a**.

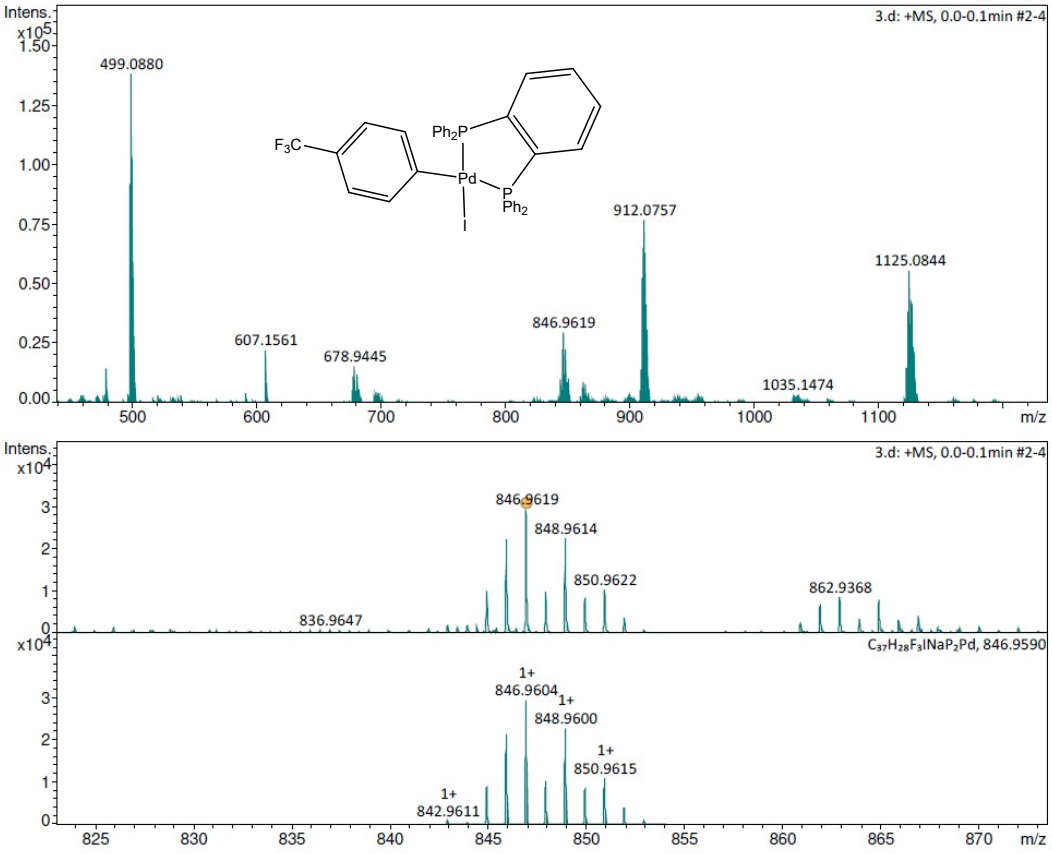

Figure S68. HRMS spectrum of **5b**.

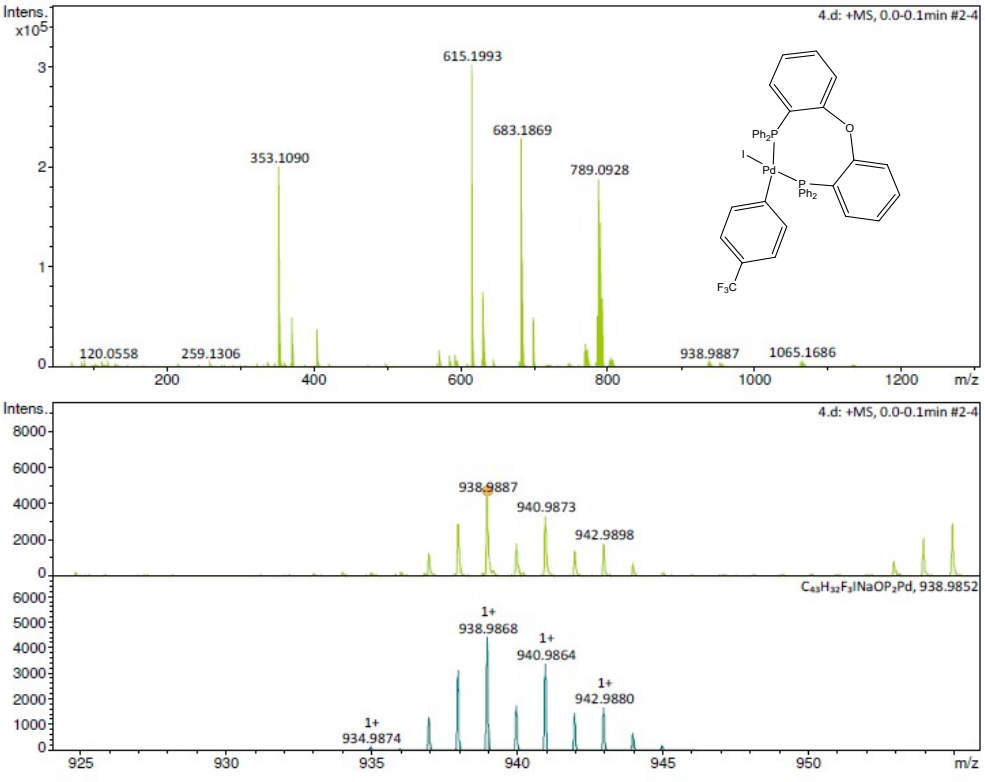

Figure S69. HRMS spectrum of **6b**.

X-RAY DIFRACTION ANALYSIS

Table S1. Crystallographic data.

Compound	**6a@100 K**	**4a@100 K**	**4a-Br@298 K**
Formula	$PdC_{42}H_{32}INO_3P_2 \cdot {}^3/_8C_4H_{10}O \cdot {}^1/_2CH_2Cl_2$	$PdC_{40}H_{32}FeINO_2P_2$	$PdC_{40}H_{32}BrFeNO_2P_2$
M/g·mol^{-1}	964.18	909.75	862.76
Space group	*C* 2/*c*	*P* 2$_1$/*c*	*P* 2$_1$/*c*
Crystal system	Monoclinic	Monoclinic	Monoclinic
a/Å	34.741(7)	21.393(4)	21.451(4)
b/Å	10.714(2)	9.493(2)	9.566(2)
c/Å	25.823(5)	16.865(3)	16.916(3)
α/°	90	90	90
β/°	116.48(3)	95.88(3)	95.90(3)
γ/°	90	90	90
V/Å^3	8603(4)	3407.0(12)	3452.8(12)
Z	8	4	4
T/K	100(2)	100(2)	298(2)
D_c/g·cm^{-3}	1.489	1.774	1.660
F(000)	3846	1800	1728
μ/mm^{-1}	0.906	1.361	1.541
Measured Reflections	97763	76340	79620
Unique Reflections	18733	14752	15216
R_{int}	0.0257	0.0393	0.0594
Obs. Refl.ns [I≥2σ(I)]	17229	12732	9738
θ_{min}- θ_{max}/°	1.14 – 31.08	0.84 – 31.08	0.83 – 31.10
hkl ranges	-57,57; -17,17; -42,42	-33,33; -15,15; -28,27	-34,34; -15,15; -26,26
R(F^2) (Obs.Refl.ns)	0.0452	0.0473	0.0472
wR(F^2) (All Refl.ns)	0.1304	0.1294	0.1365
No. Variables	541	433	433
Goodness of fit	1.042	1.112	1.015
$\Delta\rho_{max}$; $\Delta\rho_{min}$/e·Å^{-3}	2.20; -2.27	1.77; -2.08	0.90; -1.44
CCDC Deposition N.	2324443	2324442	2324438

Compound	**7-Cl@100 K**	**7-Br@298 K**	**4a-Cl@298 K**
Formula	$PdC_{19}H_{19}ClN_2O_2S$	$PdC_{19}H_{19}BrN_2O_2S$	$PdC_{40}H_{32}ClFeNO_2P_2$
M/g·mol^{-1}	481.27	525.73	818.30
Space group	*P* 2$_1$/*c*	*P* 2$_1$/*c*	*P* 2$_1$/*c*
Crystal system	Monoclinic	Monoclinic	Monoclinic
a/Å	10.656(2)	10.774(2)	21.819(4)
b/Å	15.118(3)	15.515(3)	9.590(2)
c/Å	11.730(2)	11.805(2)	17.302(3)
α/°	90	90	90
β/°	95.77(3)	95.72(3)	106.89(3)
γ/°	90	90	90
V/Å^3	1880.1(7)	1963.5(7)	3464.1(13)
Z	4	4	4
T/K	100(2)	298(2)	298(2)
D_c/g·cm^{-3}	1.700	1.778	1.569
F(000)	968	1040	1656
μ/mm^{-1}	0.857	2.153	0.781
Measured Reflections	43969	45706	80221
Unique Reflections	8214	8479	15222
R_{int}	0.0277	0.0316	0.0192
Obs. Refl.ns [I≥2σ(I)]	7978	7537	13869
θ_{min}- θ_{max}/°	1.68 – 31.07	1.90 – 31.10	0.85 – 31.10
hkl ranges	-16,16; -25,25; -18,18	-17,17; -24,24; -19,19	-35,35; -14,14; -28,28
R(F^2) (Obs.Refl.ns)	0.0215	0.0313	0.0322
wR(F^2) (All Refl.ns)	0.0628	0.0894	0.0969

No. Variables	239	239	410
Goodness of fit	1.042	1.038	1.021
$\Delta\rho_{max}$; $\Delta\rho_{min}$/e·Å^{-3}	1.44; -0.85	1.61; -1.46	1.53; -1.21
CCDC Deposition N.	2324439	2324440	2324441

Table S2. Selected palladium distances and angles for **6a** at 100 K.

6a (100 K) - $PdC_{42}H_{32}INO_3P_2$

Distances	(Å)	**Angles**	(°)
Pd_1-C3_4	2.018(3)	C3_4-Pd_1-I_3	85.59(6)
Pd_1-I_3	2.628(1)	P10_2-Pd_1-C3_4	88.91(7)
Pd_1-P10_2	2.301(1)	P10_2-Pd_1-P30_2	101.07(3)
Pd_1-P30_2	2.398(1)	P30_2-Pd_1-I_3	86.91(2)

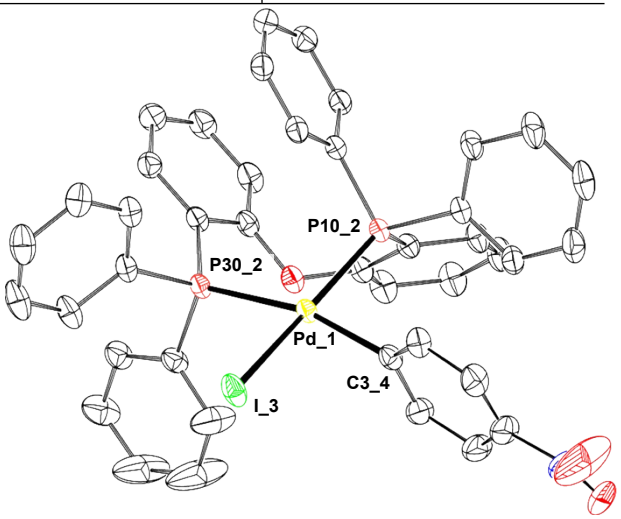

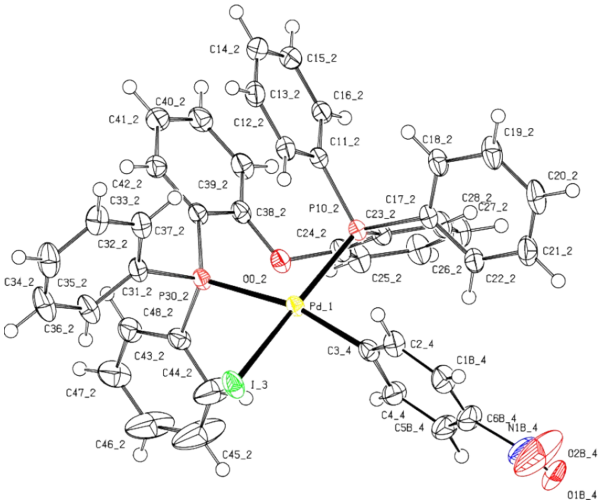

Table S3. Selected palladium distances and angles for **4a** at 100 K.

4a (100 K) - $PdC_{40}H_{32}IFeNO_2P_2$

Distances	(Å)	Angles	(°)
Pd_1-C3_3	2.041(3)	C3_3-Pd_1-I_4	84.49(8)
Pd_1-I_4	2.640(1)	P1_2-Pd_1-C3_3	86.86(8)
Pd_1-P1_2	2.286(1)	P1_2-Pd_1-P2_2	100.02(3)
Pd_1-P2_2	2.405(1)	P2_2-Pd_1-I_4	88.63(2)

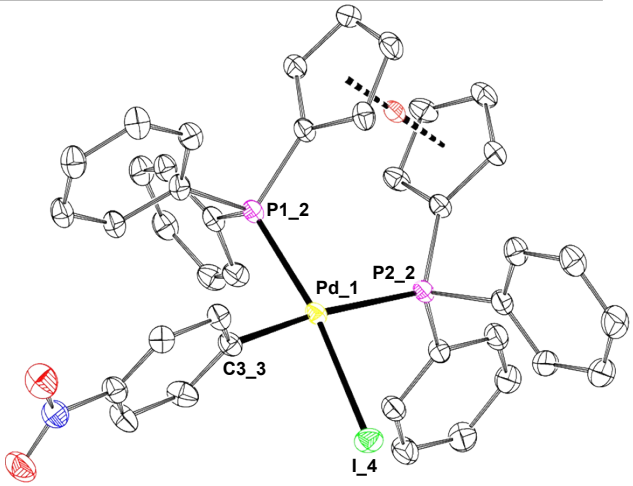

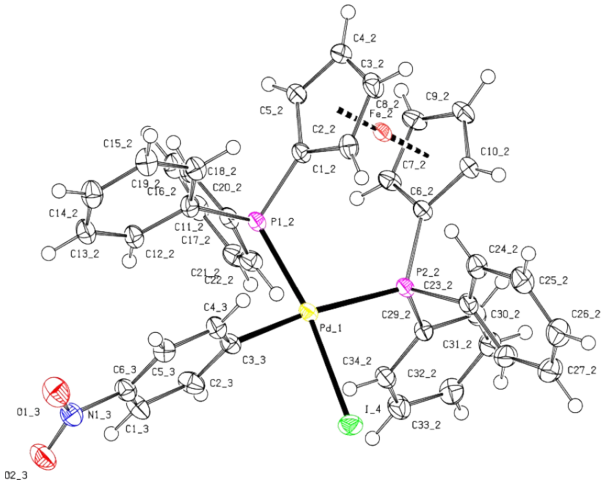

Table S4. Selected palladium distances and angles for **4a-Br** at 298 K.

4a-Br (298 K) - $PdC_{40}H_{32}BrFeNO_2P_2$

Distances	(Å)	Angles	(°)
Pd_1-C3_3	2.046(3)	C3_3-Pd_1-Br_4	85.22(8)
Pd_1-Br_4	2.512(1)	P1_2-Pd_1-C3_3	87.05(8)
Pd_1-P1_2	2.279(1)	P1_2-Pd_1-P2_2	99.91(3)
Pd_1-P2_2	2.409(1)	P2_2-Pd_1-Br_4	87.80(2)

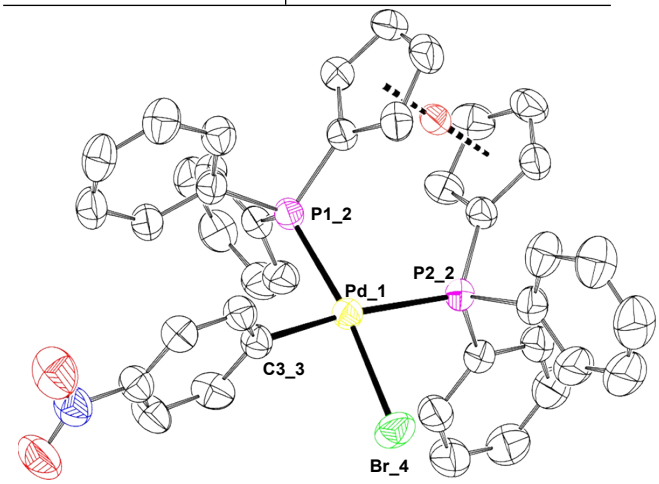

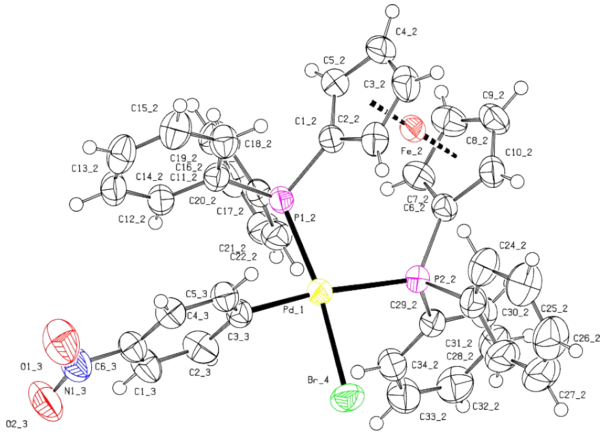

Table S5. Selected palladium distances and angles for **7-Cl** at 100 K.

7-Cl (100 K) – $PdC_{19}H_{19}ClN_2O_2S$

Distances	(Å)	Angles	(°)
Pd_1-C3_4	1.978(1)	C3_4-Pd_1-Cl_3	88.98(3)
Pd_1-Cl_3	2.340(1)	Cl_3-Pd_1-N1_2	95.19(3)
Pd_1-S_2	2.276(1)	N1_2-Pd_1-S_2	85.02(3)
Pd_1-N1_2	2.139(1)	C3_4-Pd_1-S_2	90.83(3)

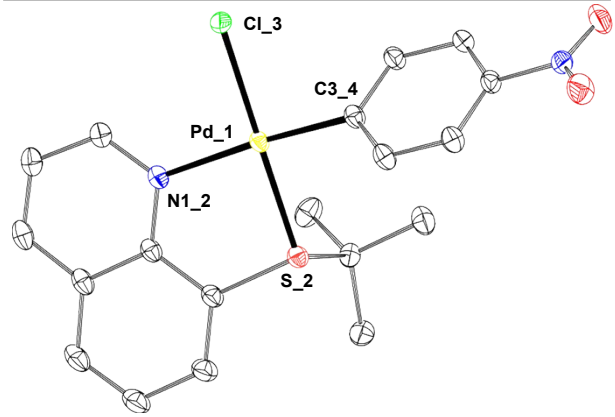

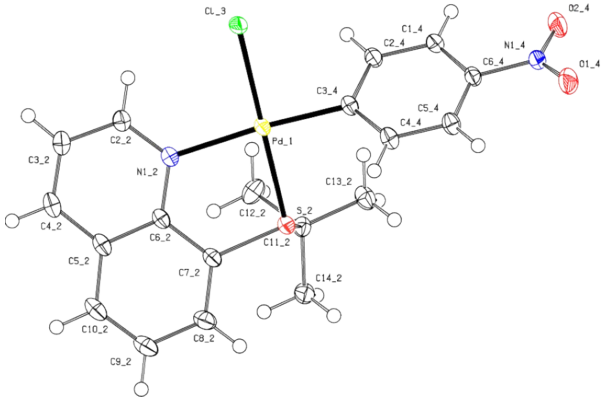

Table S6. Selected palladium distances and angles for **7-Br** at 298 K.

7-Br (298 K) - $PdC_{19}H_{19}BrN_2O_2S$

Distances	(Å)	Angles	(°)
Pd_1-C3_4	1.984(2)	C3_4-Pd_1-Br_3	88.51(5)
Pd_1-Br_3	2.440(1)	Br_3-Pd_1-N1_2	95.59(4)
Pd_1-S_2	2.287(1)	N1_2-Pd_1-S_2	84.82(4)
Pd_1-N1_2	2.145(2)	C3_4-Pd_1-S_2	91.08(5)

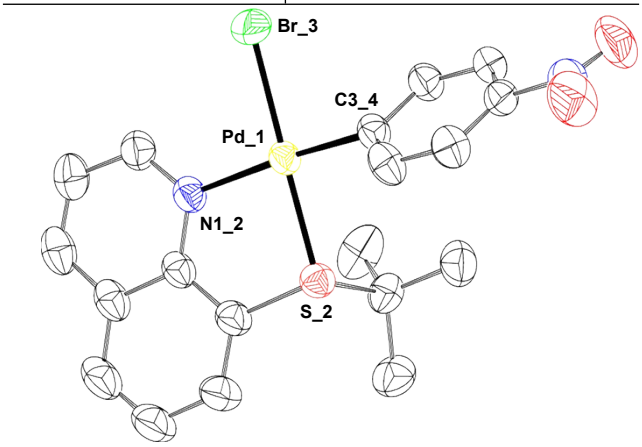

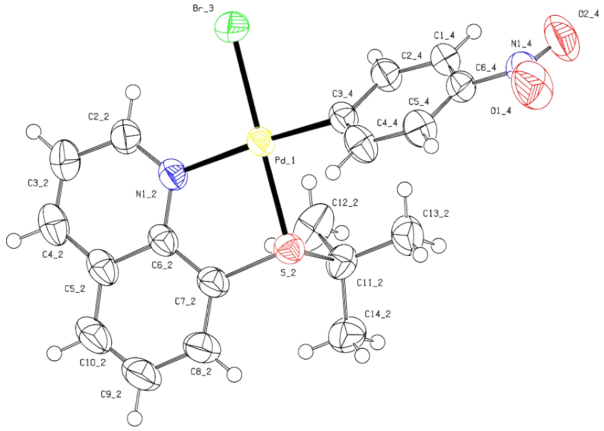

Table S7. Selected palladium distances and angles for **4a-Cl** at 298 K.

4a-Cl (298 K) - $PdC_{40}H_{32}ClFeNO_2P_2$

Distances	(Å)	Angles	(°)
Pd_1-C3_4	2.034(2)	C3_4-Pd_1-Cl_3	85.97(4)
Pd_1-Cl_3	2.391(1)	P1_2-Pd_1-C3_4	87.72(4)
Pd_1-P1_2	2.273(1)	P1_2-Pd_1-P2_2	100.37(2)
Pd_1-P2_2	2.396(1)	P2_2-Pd_1-Cl_3	85.89(2)

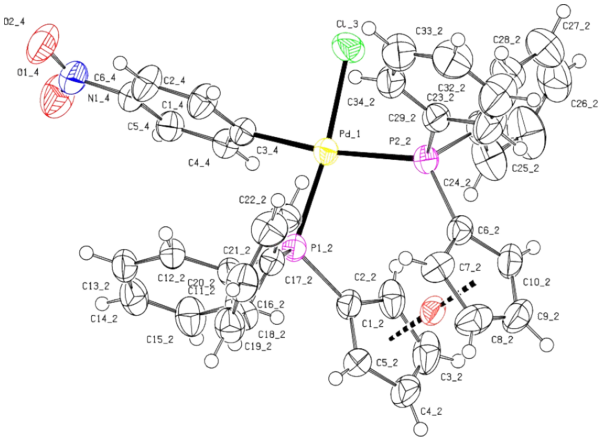

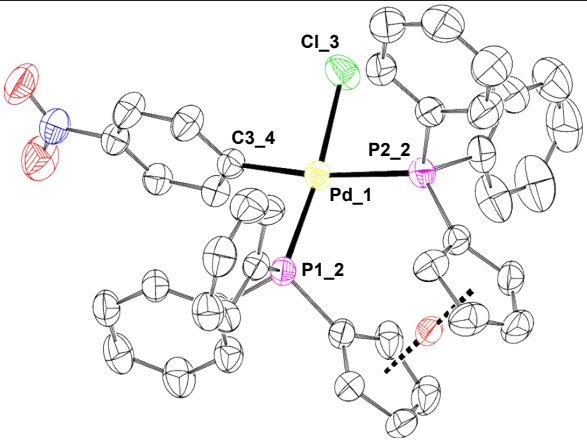

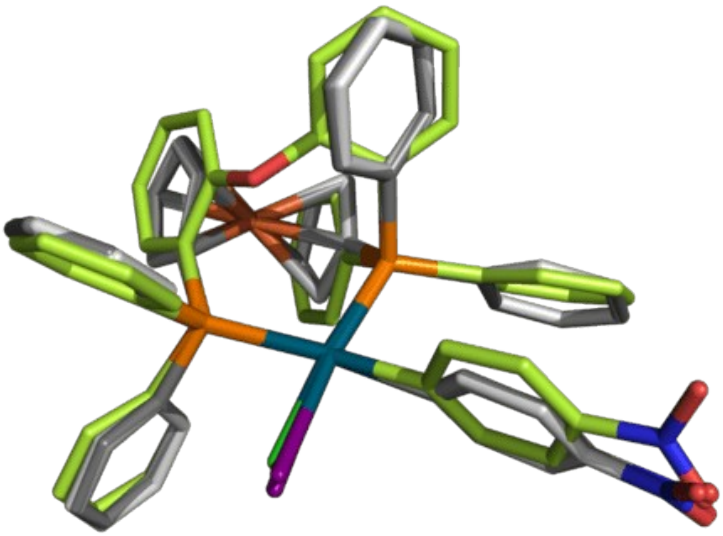

Figure S70. Superimposition of **6a** (green sticks), **4a**, **4a-Br** and **4a-Cl** (sticks with different shades of grey). Hydrogens omitted for clarity.

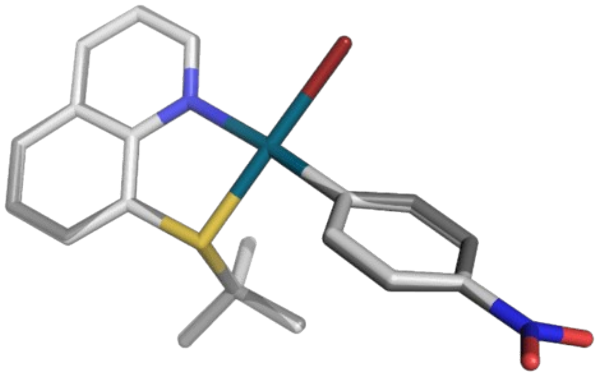

Figure S71. Superimposition of **7-Cl** (dark grey sticks) and **7-Br** (light grey sticks). Hydrogens omitted for clarity.

Table S8. Diagnostic characterization data of Pd(II)-aryl complexes bearing diphosphine ligands.

Compound	^{31}P NMR (δ, ppm)	Multeplicity	J_{P-P} (Hz)	Pd-C (Å)	Pd-X (Å)	Pd-P (Å)	P-Pd-P (°)	τ_4
2a	37.5, 51.0	d d	26.1 26.1					
2b	35.5, 50.2	d d	27.2 27.2					
2c	34.0, 48.9	d d	27.9 27.9					
2d	33.9, 48.7	d d	27.6 27.6					
3a	-9.9, 9.7	d d	52.6 52.6					
3b	-10.3, 10.3	d d	53.3 53.3					
4a	9.3, 26.2	d d	32.0 32.0	2.041(3)	2.640(1)	2.286(1) 2.405(1)	100.02(3)	0.11
4a-Br	10.4, 30.3	d d	31.2 31.2	2.046(3)	2.512(1)	2.279(1) 2.409(1)	99.91(3)	0.11
4a-Cl	11.3, 31.5	d d	31.0 31.0	2.034(2)	2.391(1)	2.273(1) 2.396(1)	100.37(2)	0.11
4b	8.7, 26.5	d d	33.5 33.5					
4c	8.0, 26.4	d d	34.5 34,5					
5a	45.1, 51.2	d d	26.4 26.4					
5b	43.8, 51.1	d d	27.4 27.4					
6a	5.2, 9.7	d d	33.0 33.0	2.018(3)	2.628(1)	2.301(1), 2.398(1)	101.07(3)	0.20
6b	4.3, 10.4	d d	34.0 34.0					

KINETIC STUDY OF THE FORMATION OF DPPBZ COMPLEXES

Preliminary attempts to obtain [PdI(*p*-R-Ph)(dppbz)] (**5a-b**) complexes have highlighted that the substitution reaction of the tmeda ligand with dppbz is a moderately slow reaction. This fact is rather unusual considering the high rate with which ligand exchange processes generally occur in Pd(II) complexes, and it is certainly attributable to a combination of the steric hindrance and rigidity of the dppbz ligand. The slow formation of the target products allowed us to undertake a detailed kinetic study of the reaction which, in addition to being intrinsically interesting, it precisely indicated us the time necessary for the preparation of the complexes of interest.
The technique that has proven to be most suitable for the kinetic analysis of the reaction was the ^{1}H-NMR spectroscopy. Using [PdI(*p*-NO_2-Ph)(tmeda)] (**1a**) as a model substrate, the operating conditions adopted are indicated in Figure S72.

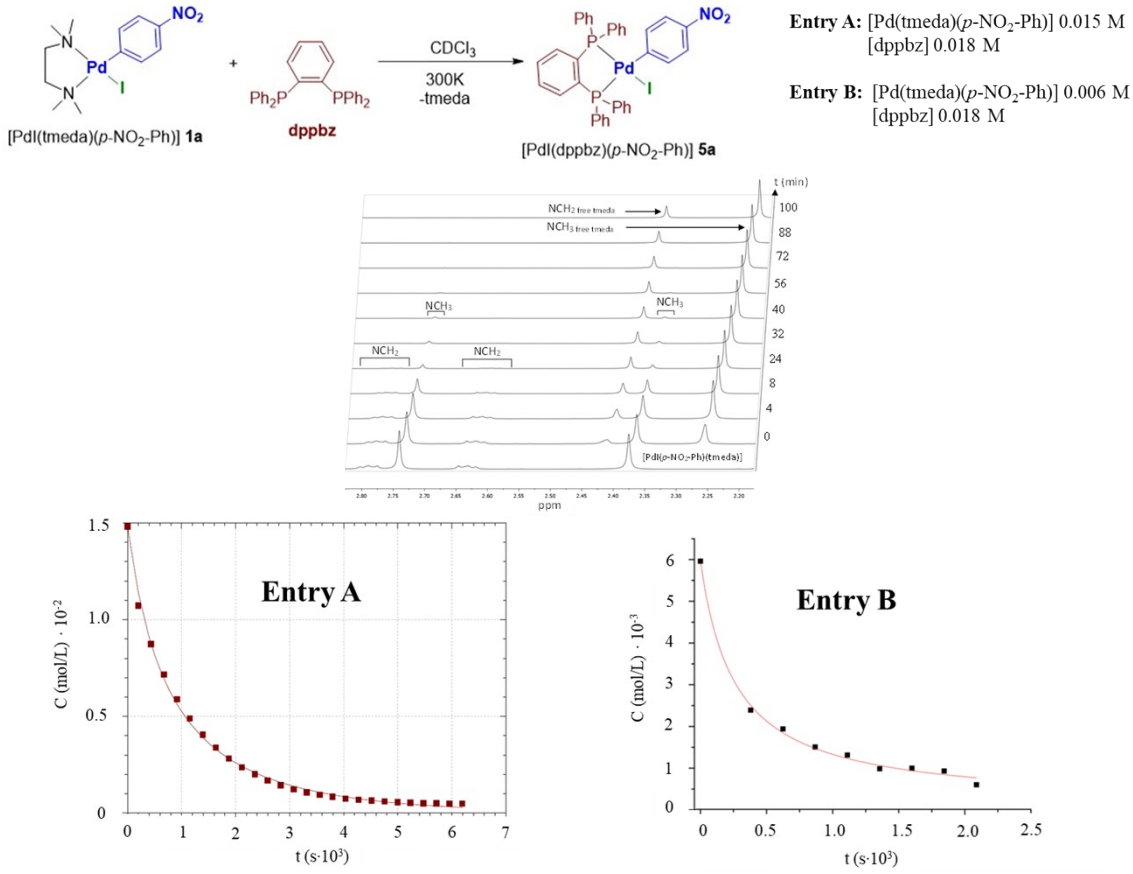

Figure S72. Kinetic study in the case of complex **5a**.

The integration of one of the peaks of the methyl groups of the coordinated tmeda allowed the exact quantification of the variation in concentration of the starting complex over time.
The kinetic law that reasonably governs the process is of the second order with dependence both on the concentration of the starting complex and diphosphine ligand (equation 1):

Equation 1. $-d[\text{complex}]/dt = k[\text{complex}][\text{dppbz}]$

This law effectively agrees with the experimental data as can be seen from the fitting (figure 6) obtained from the non-linear regression based on the system of equations (complex = [PdI(*p*-NO_2-Ph)(tmeda)] (**1a**) and product = [PdI(*p*-NO_2-Ph)(dppbz)] (**5a**)):

Equations 2a-c.
$$\begin{cases} a) -d[complex]/dt = k[complex][dppbz] \\ b)\ [complex]_0 = [complex] + [product] \\ c)\ [product]_0 = [dppbz] + [product] \end{cases}$$

The value of the kinetic constant (*k*) obtained from the regression analysis, using two different set of complex and dppbz concentrations: entry A ([PdI(*p*-NO_2-Ph)(tmeda)]=0.015 M, [dppbz]= 0.018 M); entry B ([PdI(*p*-NO_2-Ph)(tmeda)]= 0.006 M, [dppbz]= 0.018 M), are 0.068 ± 0.005 $L \cdot mol^{-1} \cdot s^{-1}$ and 0.071 ± 0.007 $L \cdot mol^{-1} \cdot s^{-1}$, respectively.

A computational DFT study has shed light on the mechanism that governs the substitution process between the two bidentate ligands. As can be seen from Figure 7, the rate-determining step is the coordination of one of the two phosphorous atoms to the metal center. This fact is in accordance with the experimentally observed second order law.

Curiously, this attack leads to the displacement of the nitrogen atom of tmeda *trans* to the halide (a less *trans*-labilizing ligand with respect to the aryl one). However, this result is justified by the obtainment of a more stable intermediate in which the entering phosphorus is located in *trans* to the iodide.

Finally, the process is completed with a fast intramolecular step that determines the final release of the tmeda ligand. This explains the lack of signals ascribable to the intermediate species in the recorded NMR spectra.

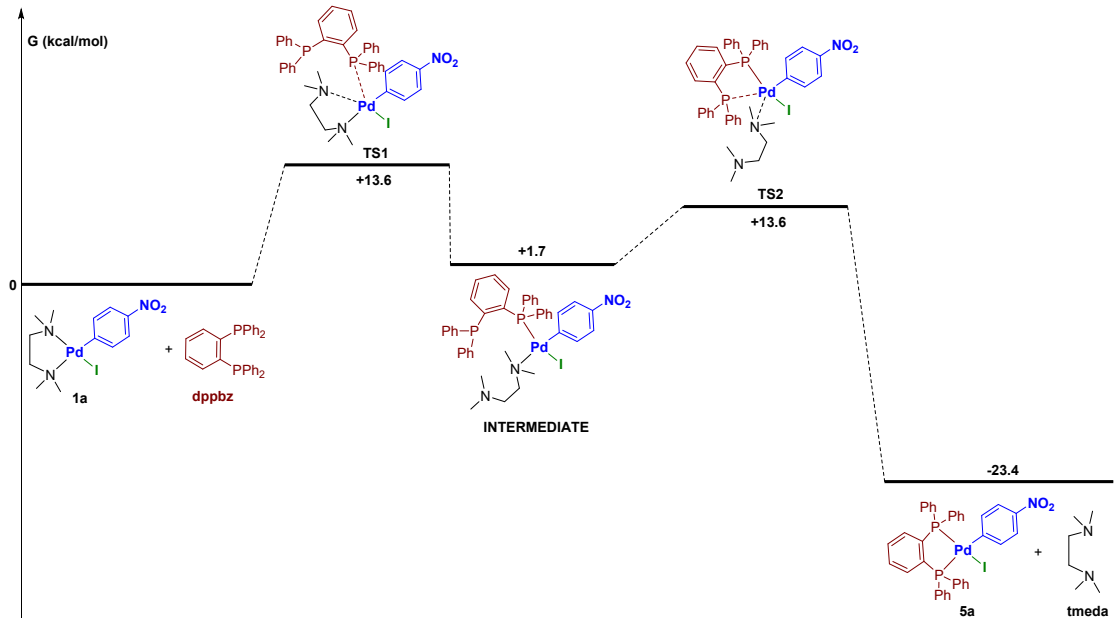

Figure S73. Proposed mechanism for the reaction studied.